ISSN 1000-9620

Marine Science Bulletin

海洋通报

Volume 11 • Number 2 2009

ISSN 1000-9620
02>
9 771000 962001

NATIONAL MARINE DATA AND
INFORMATION SERVICE OF CHINA

MARINE SCIENCE BULLETIN

Vol. 11 No. 2 Oct. 2009

CONTENTS

Comparison between Infrared and Microwave Radiometers
for Retrieving Sea Surface Temperature ····· YIN Xiao-bin et al. (01)

Studies of Variational Assimilation for the Inversion
of the Coupled Air-sea Model ····· DU Hua-dong et al. (13)

Numerical Study on Tides in the Taiwan Strait
And its Adjacent Areas ····· ZHU Jia et al. (23)

Effect of Fouling in Daya Bay Scallop *chlamys nobilis* (reeve)
Cultivation: Food Competition and Nutrient Release ····· SU Zhen-xia et al. (37)

Distribution of Turbidity and Fluorescence of SPM
in Adjacent Waters of Taiwan Bank in Summer ····· HU Yi et al. (45)

Relationship between Phytoplankton Distribution
and Environmental Factors in the Chukchi Sea ····· LIN Geng-ming et al. (55)

Sequence Comparison of Mitochondrial 16S rRNA Gene
between Two Sesarma Species ····· XU Jing-ming (65)

Sedimentary Environment analysis of Ancient Sand Ridges
From Zk23 Hole in the East China Sea ····· DU Wen-bo et al. (72)

Eco-Environment Status of the Bohai Bay
and the Impact of Coastal Explotation ····· NIE Hong-tao et al. (81)

Comparison between Infrared and Microwave Radiometers for Retrieving Sea Surface Temperature

YIN Xiao-bin[1], WANG Zhen-zhan[1], LIU Yu-guang[2], CHENG Yong-cun[2,3], GU Yan-zhen[2], WEN Fan[2]

1. *Center for Space and Applied Research, Chinese Academy of Sciences, Beijing* 100080, *China;*
2. *Physical Oceanography Laboratory, Ocean University of China, Qingdao* 266003, *Shandong Province, China;*
3. *Institute of Meteorology, PLA University of Science and Technology, Nanjing* 211101, *Jiangsu Province, China*

Abstract: The basic principles of sea surface temperature (SST) remote sensing using infrared and microwave radiometers are introduced, and the differences between two sensors for retrieving sea surface temperature are investigated. The ground resolution, atmospheric effect, sea surface wind, skin depth, and so on have important influence on precision of sea surface temperature retrieved by two sensors. The better understanding of the advantage and disadvantage of sea surface temperature detected by infrared and microwave radiometers would help us to imply SST remote sensing data more effectively and correctly.

Keyword: infrared; microwave; radiometer; sea surface temperature

Sea surface, as the interface of sea and atmosphere, is a very important topic in the investigation and development of ocean science. Oceanic and atmospheric exchanges of energy and other processes between ocean and atmosphere are all through this surface. The internal changes of the ocean are also displayed by this surface. Using three-dimensional numerical simulation and assimilation technology of satellite remote sensing data, people can learn oceanography characteristics and physical process of the sea by collecting remote sensing information from the sea surface.

In practice, different bands of electromagnetic wave used by remote sensing are mutually complemented. For remote sensing, the ground resolution on sea surface is proportional to electromagnetic wavelength. Images obtained by infrared and visible sensors which receive shorter wavelength have better ground resolution [1, 2]. When the clouds block visible light and infrared, microwave which can penetrate clouds could make up for the lack [3-5]. As satellite remote sensing can obtain information in long-term, large scale, quasi-real-time and quasi-synchronous, it is playing a vital role in monitoring and studying the ocean.

LIBRARY
Pacific Islands Fisheries Science Center
NOAA Fisheries
Honolulu, Hawai'i

Received on January 23, 2008

1 The principle of sea surface temperature remote sensing

1.1 The principle of infrared radiometers

Various infrared radiometers can be categorized into two types: visible and near infrared radiometers and thermal infrared radiometers. With a wide usage, visible and near infrared radiometers can also be divided into two groups: broad-band radiometers and narrow-band radiometers. For example, the Multi-channel Visible Light and Infrared Scanning Radiometer (MVISR) on Chinese "FY-1" satellite and the Advanced Very High Resolution Radiometer (AVHRR) on the NOAA satellite are all broad-band radiometers. The visible and infrared bands of narrow-band radiometers are generally carried on ocean color satellite. For example, the Chinese Ocean Color and Temperature Sensor (COCTS) on "HY-1" ocean satellite, the Sea-viewing Wide Field-of-view Sensor (SeaWiFS) on NASA satellite SeaStar, and the MOderate Resolution Imaging Spectroradiometer MODIS on EOS-AM and EOS-PM(Aqua).

According to Kirchhoff's law, sea surface brightness can be expressed as:

$$L(f,\theta,\varphi,T) = e(f,\theta,\varphi)L_{BLACK}(f,\theta,\varphi,T) \tag{1}$$

where $e(\lambda, \theta, \varphi)$ is the sea surface emissivity. $L(\lambda, \theta, \varphi, T)$ is a function of sea surface temperature T, electromagnetic wave frequency f, and the solid angle θ and φ. $L_{BLACK}(\lambda, \theta, \varphi, T)$ is the brightness of blackbody which has the same temperature with the sea surface. Sea surface emissivity in the thermal infrared band is a constant closer to 1, generally determined by experience. If $L(\lambda, \theta, \varphi, T)$ and the sea surface emissivity e $(\lambda, \theta, \varphi)$ are known, $L_{BLACK}(\lambda, \theta, \varphi, T)$ can be calculated according to the formula (1). Then the sea surface temperature can be calculated by the brightness $L_{BLACK}(\lambda, \theta, \varphi, T)$ according to Planck's law. In fact, the experienced methods are used to retrieve the sea surface temperature, especially the multi-channel statistical algorithm. In this way, we can not only avoid the unknown issues of seawater infrared emissivity, but also solve the problem of atmospheric correction at the same time.

1.2 The principal of microwave radiometer measuring sea surface temperature

The wavelength of microwave is 0.1 cm - 100 cm, which can be divided to millimeter wave, centimeter wave and decimeter wave, and so on. Microwave is featured by clouds penetrating and all-day-round working. Microwave remote sensing can be divided into active and passive microwave remote sensing.

Ignoring the contribution of various particles in the atmosphere, there is a simple relationship between the sea surface temperature and the brightness temperature $T_b(f)$ measured by microwave radiometer. Take Rayleigh–Kings's law into the formula (1), we have

$$T(f,\theta,\varphi,T_{SST}) = e(f,\theta,\varphi)T_{SST} \tag{2}$$

where $T(f, \theta, \varphi, T_{SST})$ is the brightness temperature measured by microwave radiometer; T_{SST} is the

temperature in a thin layer of sea surface water and it represents the sea surface thermodynamic temperature, which is different to the temperature of bucket water got from a certain depth. If sensors are on a high enough platforms above the sea surface, such as aircraft and satellite, the atmospheric correction should be considered, i.e. adding emission of the atmosphere and transmittivity into formula (2).

According to Kirchhoff's law, the relationship between emissivity e and Fresnel reflectivity ρ of calm sea surface is

$$e_{H,V}(f,\theta,\varphi)=1-\rho_{H,V}(f,\theta,\varphi) \tag{3}$$

where subscript H and V represent horizontal and vertical polarization of electromagnetic wave respectively, and f is frequency. θ is observation zenith, which represents the angle between the observation direction and the normal of sea surface. φ is azimuth angle that represents the angle between observation direction and wind direction. For the calm sea surface, the expression of Fresnel reflectivity ρ is

$$\rho_H(\theta)=\left|R_{hh}(\theta)\right|^2=\left|\frac{\cos\theta-\sqrt{\varepsilon_r-\sin^2\theta}}{\cos\theta+\sqrt{\varepsilon_r-\sin^2\theta}}\right|^2 \tag{4}$$

$$\rho_V(\theta)=\left|R_{vv}(\theta)\right|^2=\left|\frac{\varepsilon_r\cos\theta-\sqrt{\varepsilon_r-\sin^2\theta}}{\varepsilon_r\cos\theta+\sqrt{\varepsilon_r-\sin^2\theta}}\right|^2 \tag{5}$$

where $R_{hh}(\theta)$ *and* $R_{vv}(\theta)$ are horizontal and vertical Fresnel reflectance respectively and their squared absolute value are equal to Fresnel reflectivity ρ. The permittivity ε_r of the sea water can be calculated by Debye Equation, which is

$$\varepsilon_r(\omega,T_S,S_S)=\varepsilon_\infty+\frac{\varepsilon_S-\varepsilon_\infty}{1-i\omega\tau}+i\frac{\sigma}{\omega\varepsilon_0} \tag{6}$$

where $\omega=2\pi f$ is angle frequency of electromagnetic wave, T_S is sea surface temperature, S_S is sea surface salinity, ε_∞ is infinite high frequency permittivity, ε_S is static permittivity, τ is relaxation time, σ is ion conductivity, ε_0 is permittivity in vacuum.

According to certain special characteristics of seawater permittivity in each wave band, we can measure the sea surface salinity, temperature and wind speed by specific wave bands. In microwave frequency less than 10 GHz, Klein and Swift (1977) [6] use various concentrations of NaCl resolution as samples instead of seawater and get the estimated parameters in Debye Equation. In the frequency range of 3 - 20 GHz, Ellison et al.[7] give the similar formulae by studying seawater samples with temperature of -2 °C - 30 °C and salinity of 20% - 40%. According to Debye Equation and the estimated parameters, we can obtain seawater permittivity. In the frequency range of 6 GHz - 7 GHz, Fresnel reflectivity ρ changes little with salinity and temperature. So sea surface emissivity e in the range of 6 GHz - 7 GHz can be approximatively considered not as a function of sea surface temperature and salinity, but a constant. Based on brightness temperature $T_b(\lambda)=e\cdot t\cdot T_S$ received by microwave radiometer, sea surface

temperature T_S can be calculated, once atmospheric transmittivity is known. We should consider the effect of rough sea surface in practical retrieving and correct the above calm sea surface emissivity expression[8].

2 Comparison between infrared and microwave radiometers for retrieving sea surface temperature

Infrared and microwave radiometer data are the main equipments for global sea surface temperature remote measuring. Because infrared and microwave sensors have different working principles, each of them has advantage and disadvantage when they are affected by various external conditions. The measured data will be influenced directly or indirectly by many factors, such as the noise of sensor itself, accuracy of retrieving algorithm, ground resolution of sensor, orbit period of satellite, effect of wind, and conditions of atmosphere.

2.1 Comparison between ground resolution and retrieving accuracy

To achieve different purpose, the choices of sensor types and ground resolution, and other parameters are different absolutely. In general, the level of resolution is the main indicator of remote sensing data application, and improving the resolution is also a direction of sensor development. With the development of world's economy and society, people have a continual and deep understanding on the world's resource and environment, so that the requirements for resolution are improving, which contain time and ground resolution and spectral resolution. According to the fluctuation theory of electromagnetic wave, the angle resolution of radiometer is only determined by λ/D; the ground resolution is determined by parameters λ, D, H (D is the aperture of camera or antenna, λ is the wavelength of electromagnetic wave, H is the distance between satellite and ground). The shorter the wavelength of the electromagnetic wave is, the higher the resolution is. The bigger the aperture is, the higher the resolution is. Since infrared wavelength is much shorter than microwave wavelength, and their ratio is 10^{-5}, the ground resolution of infrared radiometer is far higher than the microwave radiometer in general.

AVHRR on the TIROS-N satellite can accurately map out the sea surface temperature image with 1 km resolution and better than 0.5 °C temperature accuracy. Compared the ship and buoy measured data with the global sea surface temperature observed by thermal infrared band radiometer - MODIS, it is found that accuracy of sea surface temperature measured by MODIS reaches 0.25 °C. The resolution of microwave radiometer is less. For example, the ground resolution of AMSR-E is 25 km and accuracy of temperature retrieving exceeds 1 °C.

2.2 Comparison of effects from the atmosphere

When measuring sea surface by satellite, it is found that the atmosphere can not only weaken but also strengthen infrared signal of sea surface. So, atmospheric correction is an indispensable component in infrared remote sensing. Fig. 1 shows absorptivity of different gases(vapor, CO_2, O_2, O_3, N_2O, CH_4) in

different wavelength [9]. The figure indicates that bands of 3.7μm - 4.1 μm and 10μm - 12 μm are two infrared windows for detecting sea surface [10]. Because atmosphere temperature is lower than sea surface temperature, atmosphere components radiate out in low temperature after absorbing sea surface radiation, so that spectral peak to shift longer wavelength. As a result, the effect of atmospheric absorption reduces sea surface radiation reached infrared radiometer, and atmospheric radiation adds sea surface radiation reached infrared radiometer. For infrared wave band, vapor, CO_2, O_3 are the main absorbing gases, and the scattering effects of these gases could be ignored. Aerosol scattering plays a smaller role in the near infrared band and this effect can be ignored in the mid-infrared, thermal infrared and microwave band.

Atmosphere has different effects on infrared remote sensing in different wavelength. According to these different effects, different band-groups are used to eliminate atmospheric effects, and get sea surface temperature (SST). Therefore, using of multi-channel remote sensing technology to eliminate atmospheric effects is very effective.

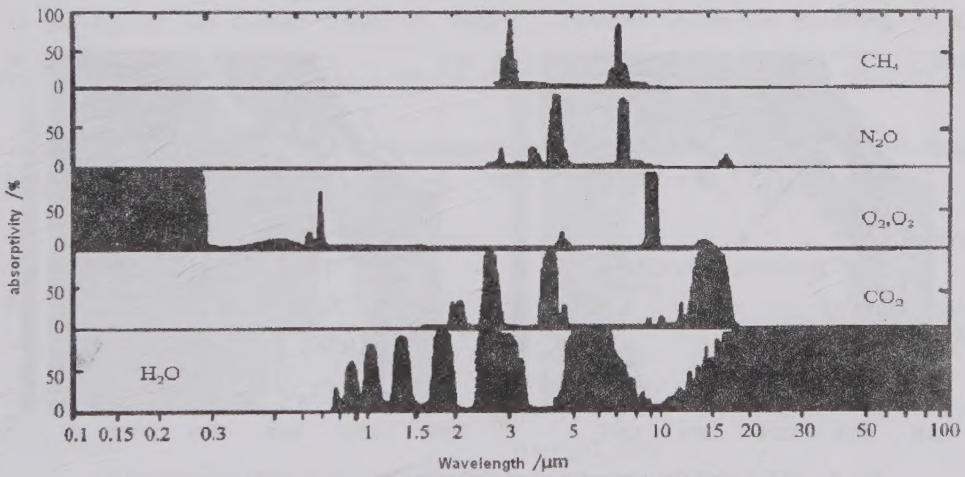

Fig. 1 Absorptivity of main components of atmosphere

Since microwave can penetrate thin clouds, it could be called all-day-round satellite detector. Wavelength of microwave is longer than wavelength of visible light and infrared, and air molecules and aerosol particle size are much smaller than wavelength of microwave. Therefore, scatter of various particles in the atmosphere is not very important to microwave radiometer. But in the range of 21 GHz - 24 GHz, the absorbing effects of O_2, H_2O, vapor and other substances can not be ignored [11]. As shown by Fig. 2, vapor, O_2, and H_2O are the main absorption matters for the microwave band. Atmospheric absorption has little impacts on microwave less than 12 GHz, and atmospheric correction is simple relatively. For example, a cloudy weather with vapor content of 60 mm and H_2O content of 0.2 mm, the total attenuation of microwave signal generated by atmosphere is less than 0.05%. Therefore, the impact of atmosphere and errors caused by path correction are not the main errors of retrieving sea surface temperature and salinity by microwave radiometer.

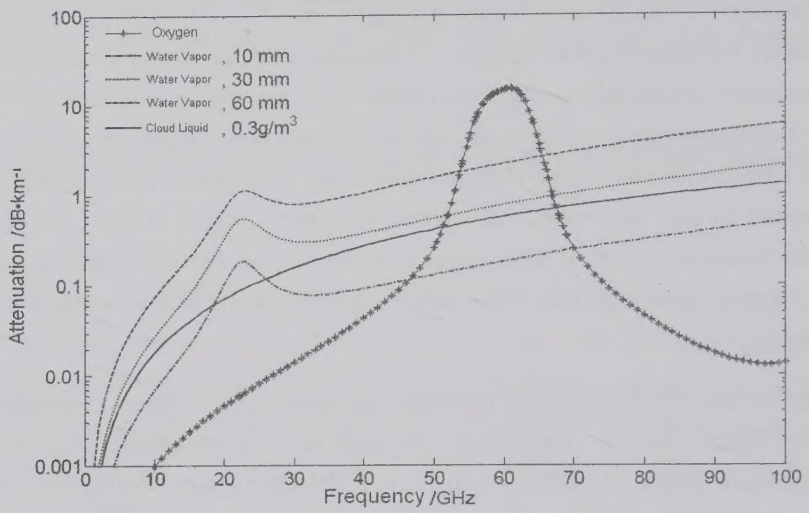

Fig. 2 Atmospheric attenuation at microwave bands.

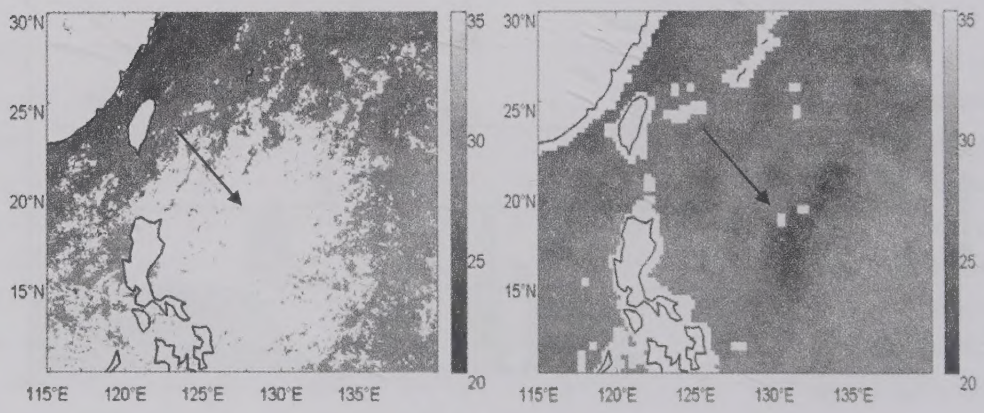

Fig. 3 SST during the appearance of typhoon Ketsana (weekly averaged data)

(a) SST from MODIS (b) SST from AMSR

In Fig. 3(a) and (b) show SST image of West Pacific around October 20, 2003, and these two pictures are weekly average results. Fig. 3(a) shows that clouds caused by typhoon affect the infrared observation obviously. The infrared sensors displayed some blind plots through the path of Typhoon, and the impact of cloud is significant in the region indicated by arrows. However, in Fig. 3(b), microwave radiometer observed the temperature drop when Typhoon passed, and the clouds in atmosphere have less impacts on microwave radiometer observation. For retrieving sea surface temperature in cloudy conditions, microwave radiometer has considerable advantage.

2.3 Comparison of effects from sea surface wind

In the condition of storm, the calculation for sea surface emissivity e and Fresnel reflectivity ρ are very complex, and ρ of sea-atmosphere interface will be changed with wind. Sea surface wind has

impacts on reflectivity through roughness (U_{10} <15 m/s) and foam (U_{10} >15 m/s) caused by the storm.

According to Planck's law of blackbody radiation, emissivity of seawater is determined experientially for visible light and infrared, and sea surface is close to Lombard surface. Therefore, in the range of infrared wave band, sea surface emissivity caused by wind changes little.

The effect of sea surface roughness can be calculated by geometry model of electromagnetic wave reflected/scattered by the sea surface [12]. In short, wind results in sea surface slope changing, and then observation zenith angle and polarization are changed, which leads to the changing of reflectivity and brightness received by radiometer. Foam produced by broken ocean wave under high wind speed will increase sea surface microwave emissivity. Therefore, brightness temperature received by microwave sensor is determined by sea surface temperature, salinity, roughness related to wind speed, foam raised by broken wave.

Fig. 4 shows ($\partial T_{H,V}/\partial U_{10}$) versus U_{10}, ($\partial T_{H,V}/\partial T_S$) versus T_S and $\left(\int_{\varphi-10}^{\varphi+10}(\partial T_{H,V}/\partial\varphi)d\varphi\right)$ versus φ. The curves in the figures are derived based on AMSR (Advanced Microwave Scanning Radiometer) algorithms[8]. We plot $\left(\int_{\varphi-10}^{\varphi+10}(\partial T_{H,V}/\partial\varphi)d\varphi\right)$ here to show the effect of wind direction error on $T_{H,V}$. The integral interval is limited between azimuth angles with φ-10° and φ+10°, because 20° is the accuracy of wind direction retrieved from satellite data [13].

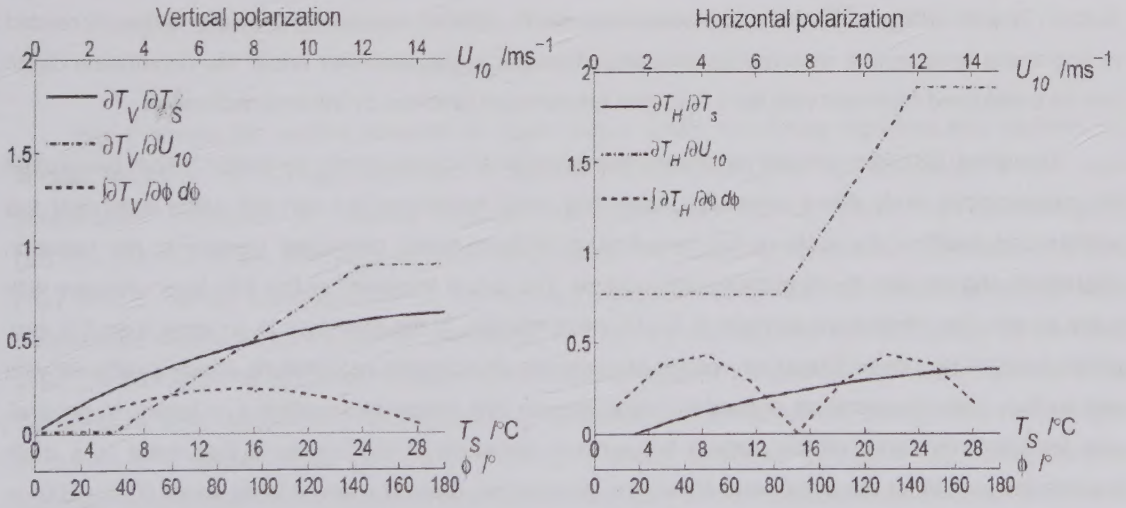

Fig. 4 ($\partial T_{H,V}/\partial U_{10}$) versus U_{10}, ($\partial T_{H,V}/\partial T_S$) versus T_S, and ($\int_{\varphi-10}^{\varphi+10}(\partial T_{H,V}/\partial\varphi)d\varphi$) versus φ with the frequency f being 10.7 GHz and an incidence angle θ being 55°: The sea surface is supposed to be calm for ($\partial T_{H,V}/\partial T_S$). SST is set to be 15 °C for ($\partial T_{H,V}/\partial U_{10}$). SST is 15 °C and U_{10} is 10 m/s for ($\int_{\varphi-10}^{\varphi+10}(\partial T_{H,V}/\partial\varphi)d\varphi$)

As indicated by Fig. 4, for vertical polarization and f =10.7 GHz, the changing of sea surface temperature by 1 °C results in increasing of brightness temperature by 0 to 0.6 K (sea surface temperature between 0 °C - 30 °C). Brightness temperature changes caused by sea wind speed changing 1 m/s are ladder style with speed, ranging between 0 K - 0.9 K for sea wind speed between 1 m/s - 15 m/s. When wind speed is 10 m/s, azimuth angle changing by 20° will result in brightness temperature changing up to 0.2 K. For horizontal polarization and f =10.7 GHz, changing of sea surface temperature by 1 °C results in decreasing and then increasing of brightness temperature with sea surface temperature. The range of change is 0.07 K - 0 K for sea surface temperature between 0 °C - 3 °C and 0 K - 0.3 K for sea surface temperature between 3 °C - 30 °C. Brightness temperature changes caused by sea wind speed changing 1m/s are ladder style with speed, ranging between 0.8 K - 1.9 K for sea wind speed between 1 m/s - 15 m/s. When wind speed is 10 m/s, azimuth angle changing by 20° will result in brightness temperature changing up to 0.4 K.

So, the wind speed error of 1 m/s or wind direction error of 20° may induce a retrieved SST error of 1 °C or more. However, the effects of errors from retrieved wind on SSS retrieval algorithm are even more remarkable.

2.4 Measuring the temperature difference in different water depth

If irradiance reduced to 1/e of its initial value at depth of D from sea surface, the distance D is called the penetration depth. In pure seawater which does not contain organics, penetration depth of 400 nm violet is about 75 m, and penetration depth of 700 nm red is 3 m, and penetration depth of thermal infrared is about 20 μ m - 100 μ m [14]. Within the penetration depth, infrared radiation of seawater is directly related to brightness temperature received by infrared radiometer, while seawater under the penetration depth can be considered irrelevant with the brightness temperature received by infrared radiometer.

Therefore, SST from infrared radiometer needs physical oceanography correction before being used for oceanography study. Since infrared radiation from water molecules in a very thin water layer near sea surface can overflow the surface, the temperature of those water molecules represents the radiation characters and controls the brightness temperature. The actual thickness of this thin layer changes with wave length. For infrared wavelength of 3 - 15 μm, thickness of the thin layer is no more than 0.1 mm, which is called skin layer. Therefore, remote sensing just detects skin temperature, which is different with sea surface water temperature defined in oceanography (the temperature within 1 m layer). In general, one important character of the vertical temperature structure of the ocean is that there is a main thermocline except for the polar area. Above the thermocline, there is a mixed layer about 50 m - 200 m. During daytime, sunshine will make the skin heat, especially in the strong sunshine and the weak wind summer. This will form the surface diurnal thermocline. After shined for several days, seasonal thermocline will be gradually formed. Since diurnal thermocline and seasonal thermocline make it a big difference between skin temperature and surface temperature, they need to be corrected. During night, due to the wind disturbance and output of heat, diurnal thermocline disappears quickly. The diurnal thermocline problems can be ignored for infrared images got during night. Errors for skin temperature are

very complex oceanography problems which involve roughness of sea surface, wind, fog, vapor, tide, ocean current, water quality as well as sea oil film, and so on[15-19].

Within skin depth, microwave radiation of the seawater is directly related to brightness temperature received by microwave radiometer, while seawater under the skin depth can be considered irrelevant with the brightness temperature. Skin depth of microwave in seawater decreases along with wavelength of microwave. The skin depth of X-band microwave with f=10 GHz and wavelength=3 cm is about 2 mm. The skin depth of C-band with f=5 GHz and wavelength=6 cm is about 5 mm. The skin depth of L-band with f=1.4 GHz is about 2 cm. Therefore, correction should be implemented before SST from microwave radiometer being used for oceanographic study.

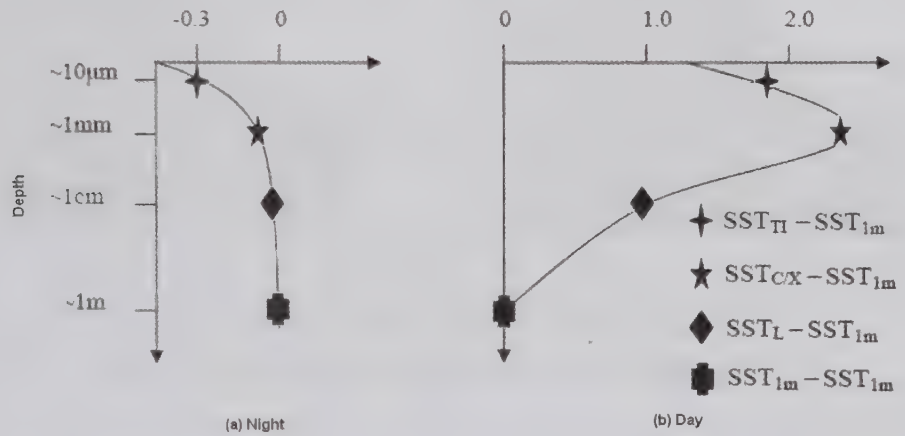

Fig. 5 Idealized temperature profiles of the near surface layer (~1 m depth) of the ocean during (a) nighttime and (b) daytime

Fig. 5 shows the vertical structure of upper ocean within 1m during nighttime and daytime, i.e. vertical structure of (SST_{depth}—SST_{1m}). In Fig. 5, (SST_{TI}—SST_{1m}) is the difference of thin layer temperature measured by thermal infrared radiometer and SST_{1m}, marked as quadrangular; ($SST_{C/X}$—SST_{1m}) is the difference of water temperature measured by microwave radiometer (6.9 GHz /10.7 GHz, C band/X band) and SST_{1m}, marked as pentagram; (SST_{L}—SST_{1m}) is the difference of water temperature measured by microwave radiometer of L band (1.4 GHz) and SST_{1m}, marked as diamond; (SST_{1m}—SST_{1m}) is the difference of water temperature at depth of 1 m and SST_{1m}, marked as crisscross. During night, water temperature increases along with water depth, and will not change when water depth increases to a certain depth, and $SST_{TI} < SST_{C/X} \approx SST_{L}$, as shown by Fig. 5 (a). During daytime, seawater temperature vertical structure is complex with depth, which increases firstly and then decreases, and $SST_{C/X} > SST_{TI} > SST_{L}$, as shown by Fig. 5 (b). The differences of SST_{TI}, $SST_{C/X}$ and SST_{L} can reach up to 1 °C, and even higher. According to figure 5, $SST_{C/X} \approx SST_{L}$ during night, i.e. water temperature measured by microwave radiometer of 6.9 GHz / 10.7 GHz equals approximately to the temperature obtained by that of 1.4 GHz.

Since infrared radiometer just measures the sea skin temperature, sunlight will result in a higher

temperature skin during daytime, especially in the strong sunshine and weak wind summer. Due to the wind disturbance and output of heat, skin temperature decreasing will form an obvious day-night difference. Fig. 6 shows the day-night SST difference of MODIS weekly averaged data around June 28 and November 1, 2003. Skin temperature difference is obvious. Due to strong solar radiation in summer, the skin temperature difference between day and night is more significant, as shown by Fig. 6(a).

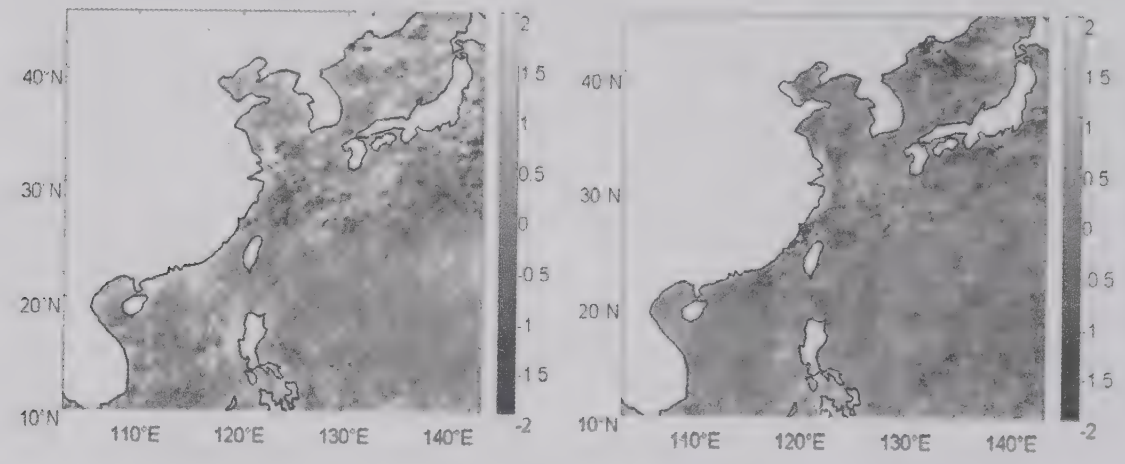

Fig. 6 Day-night SST difference of MODIS weekly averaged data
(a) for around July 28th, 2003, and (b) for around November 1st, 2003

2.5 Other factors

Except for the above factors, noise of radiometer is likely to result in a great error of retrieved temperature. So the stability of radiometer is needed. Frequency resolution of radiometer is determined by the noise and conversional precision of data-mode switch. Noise of sensor is the function of target temperature and time integral of output of switch voltage. As switch converts the target radiation energy to electronic signal, the longer time integral is, the easier elimination of random thermal noise is. Sea surface roughness, effects of atmospheric ionosphere on lower frequency microwave, background of cosmic microwave radiation, and so on can not be ignored.

3 Conclusion

Infrared radiometer and microwave radiometer have their own advantages for practical use. For all-day-round observation, two kinds of sensors make up for each other and play an important role. Ground resolution of infrared radiometer is higher than microwave radiometer. Infrared radiometers will not be impacted by sun high angle and sea surface wind. Accuracy of retrieved temperature by infrared radiometers can reach up to 0.5 °C and even higher after correction of various algorithms. Microwave can penetrate clouds. When the sea is covered by clouds and infrared radiometer affected by atmosphere can not provide data, microwave radiometers can guarantee to make up for the shortcomings and provide a

steady source of information. Since attenuation in different bands is different, infrared and microwave radiometers can be used to measure temperatures at different water depths.

Reference

[1] Yokoyama R, Tanba S. Estimation of sea surface temperature via AVHRR of NOAA-9 --Comparison with fixed buoy data [J]. Int. J. Rem. Sens., 1991, 12: 2 513-2 528.

[2] Barton I J. Interpretation of Satellite-Derived Sea Surface Temperatures [J]. Advances in Space Research, 2001, 28(1): 165-170.

[3] Jiang J S. China Microwave Remote Sensing Technology Facing to 21st Century [J]. Engineering Science, 1999, 1(2): 78-81.

[4] Jin Y Q. Remote sensing of DMSP SSM/I over the south China Sea and retrieval of sea surface wind [J]. Chinese Journal of Geophysics, 1998, 41(1): 30-37.

[5] Milman A S, Wilheit T. Sea surface temperatures from the scanning multichannel microwave radiometer on Nimbus-7 [J]. J. Geophys. Res., 1985, 90: 11 63 -11 641.

[6] Klein L A , Swift C T. An improved model for the dielectric constant of sea water at microwave frequencies [J]. IEEE Trans. Antennas Propagat., 1977, AP-25: 104-111.

[7] Ellison W, Balana A, Delbos G, et al. New permittivity measurements of seawater [J]. Radio Sci., 1998, 33: 639-648.

[8] Wentz F J, Meissner T. Algorithm theoretical basis document (ATBD) version 2 AMSR ocean algorithm [R]. RSS Tech. Proposal 121599A-1, 2000, 1-37.

[9] Chen W M. Satellite Meteorology [M]. Beijing: China Meteorological Press, 2003, 87-112.

[10] Zhou X J. Theory on emission of atmosphere and remote sensing [M]. Beijing: Science Press, 1992, 50-162.

[11] Liebe H J, Hufford G A, Cotton M G. Propagation modeling of moist air and suspended water/ice particles at frequencies below 1000GHz [Z]. AGARD 52nd Special Meeting of the Electromagnetic Wave Propagation Panel, 1993, 3: 1-10.

[12] Yin X B, Liu Y G, Zhang H D. Removing the Impact of Wind Direction on Remote Sensing of Sea Surface Salinity [J]. Chinese Science Bulletin, 2006, 51(11): 1 368-1 373.

[13] Yin X B, Liu Y G, Wang Z Z, et al. A new algorithm for microwave radiometer remote sensing of sea surface salinity and temperature [J]. Science in China, Ser. D Earth Sciences, 2006, 49(11): 1 204-1 211.

[14] Wu Y S. Analysis and Test of the Feasibility of Applying Remote Sensing to the Study of the Water Surface Thin Layer [J] . Remote Sensing Technology and Application, 1994, 9(4):1-8.

[15] Gentemann C L, Donlon C J. Diurnal signals in satellite sea surface temperature measurements [J]. Geophys. Res. Lett., 2003, 30(3): 1140, doi:10.1029/2002GL016291.

[16] Edwards T, Browning R. The along-track scanning radiometer - Measurement of sea surface temperature from ERS-1 [J]. J. Br. Interplanet. Soc., 1990, 43: 160-180.

[17] Wick G A, Bates J J, Scott D J. Satellite and Skin-Layer Effects on the Accuracy of Sea Surface Temperature Measurements from the GOES Satellites [J]. Journal of Atmospheric and Oceanic Technology, 2002, 19(11): 1 834-1 848.

[18] Schlüssel P, Emery W J. On the Skin-Bulk Temperature Difference and its Impact on Satellite Remote Sensing of Sea Surface Temperature [J]. J. Geophys .Res, 1990, 95: 13 34 -13 356.

[19] Donlon C, Minnett P. Toward Improved Validation of Satellite Sea Surface Skin Temperature Measurements for Climate Research [J]. Journal of Climate, 2002, 15(4): 353-369.

红外和微波辐射计反演海表面温度的比较

殷晓斌[1]，王振占[1]，刘玉光[2]，程永存[2,3]，顾艳振[2]，文 凡[2]

(1. 中国科学院 空间科学与应用研究中心，北京 100080；2. 中国海洋大学 物理海洋实验室，山东 青岛 266003；
3. 解放军理工大学 气象学院，江苏 南京 211101)

摘 要：介绍了红外辐射计和微波辐射计测量海表面温度的原理，分析了它们各自在反演海表面温度时的差异。在全球范围的海表面温度的遥感监测中，红外辐射计和微波辐射计的遥感精度受到多种因素影响。传感器本身的噪音、算法反演精度、传感器分辨率、搭载卫星的全球覆盖率等自身因素使辐射计的探测资料产生差别；大气状况、海面风速、测量海洋不同深度海水的表征温度等外界因子也同时影响着红外辐射计和微波辐射计的遥感精度。了解红外波段和微波波段的辐射计在各方面的优劣，有助于发挥各自特长，有效提高卫星监测海表面温度的精度。

关键词：红外；微波；辐射计；海表面温度

Studies of Variational Assimilation for the Inversion of the Coupled Air-sea Model

DU Hua-dong, HUANG Si-xun, CAI Qi-fa, CHENG Liang

1. *The Institute of Meteorology of the PLA University of Science and Technology, Nanjing* 211101, *Jiangsu Province, China;*

2. *Jiangsu Key Laboratory of Meteorology Disaster, NUIST Nanjing* 210044, *Jiangsu Province, China;*

3. *Beijing PO# Box* 2433, *Beijing* 100081, *China*

Abstract: For the prediction of ENSO, the accuracy of the model including the parameters, initial value and others of the model is important, which can be retrieved by the variational data assimilation methods developed in recent years. However, when the nonlinearity of the model is quite strong, the effect of the improvement made by the 4-D variational data assimilation may be poor due to the bad approximation of the tangent linear model to the original model. So in the paper the ideas in the optimal control is introduced to improve the effect of 4-DVAR in the inversion of the parameters of a nonlinear dynamic ENSO model. The results indicate that when the terminal controlling term is added to the cost functional of 4DVAR, which originated from the optimal control, the effect of the inversion may be largely improved comparing to the traditional 4DVAR, as can be especially obvious from the phase orbit of the model variables. The results in the paper also suggest that the method of 4DVAR in combination with optimal control cannot only reduce the error resulting from the inaccuracy of the model parameters but also can correct the parameters itself. This gives a good method in modifying the model and improving the quality of prediction of ENSO.

Keywords: variational data assimilation; coupled air-sea mode; optimal control

Introduction

For the successful prediction of ENSO, at least two aspects are essential: 1) the knowledge of dynamical mechanisms of ENSO[1] such as the unstable air-sea interaction theory[2], the Kelvin waves theory[3], the delayed action oscillator theory[4] and nonlinear self action oscillation theory[5], 2) the observation data, which the dynamical mechanism and observation are the scientific foundation and necessary precondition of the prediction. Studies in recent years have shown that the variational data assimilation methods can provide great improvements on the optimization of forcing fields and initial fields, compensation of outside force such as wind stress and the exploration of error caused by the parameterization of physical process[6].Therefore, it can be predicted that, by optimization of the initial values and model parameters of ENSO forecasting system using variational data assimilation methods, a positive significance will be shown on the forecasting ENSO events.

Received on January 31, 2008

When the variational data assimilation method is used on the retrieval of model parameters, the results of usual adjoint method based on the tangent model are often unsatisfactory for highly non-linearity model. In the literature [7], the authors proposed a method by improving tangent ways to solve this problem, and good results have been achieved. In this paper, another way is introduced to solve this problem by adding the control of the terminal item to the object functional that is used in the variational data assimilation method. With this method, the inversion of model parameters and the outside enforcing fields of a simple ENSO dynamic model is carried out by theoretical analysis and numerical experiments.

1 The coupled air-sea model

In recent years, many forecasting models have been developed for the forecasting ENSO events, of which the most representative one is the simple dynamic coupling model developed by the Lamont-Doherty Earth Observatory, i.e. the famous Cane Zebiak-simple air-sea coupling model (ZC model for short) [8, 9]. In order to explain the high irregularity and the phase character of the equatorial air-sea coupled climate system, a nonlinear ENSO dynamic system (referred to as WF96) is developed by simplifying the ZC model[10]. The system is composed of two non-dimensional equations: one is the sea surface temperature anomalies (SSTA) which describes the thermodynamic changes of ocean mixed layer, and the other is the thermocline depth abnormal (H20A) which describes the change of the upper-ocean dynamics:

$$\begin{cases} \dfrac{dT}{dt} = a_1 T - a_2 h + a_3 T(T - \mu h) + f_1, & T\big|_{t=t_0} = T_0 \\ \dfrac{dh}{dt} = b(2h - T) + f_2, & h\big|_{t=t_0} = h_0 \end{cases}, \tag{1}$$

where T represents dimensionless variables SSTA; h represents dimensionless H20A; coefficient μ represents effect of the movement of thermocline posed on the sea surface temperature (SST); dimensionless parameter b is a monotone function of the air-sea coupling coefficient which can be obtained directly by retrieving the parameter b. The value and descriptions of other parameters can be found in reference [10]. For this nonlinear dynamic system, when the value of the model coefficients and parameters is constrained to a domain, the solution exhibits a nonlinear self-excited oscillation limit ring forms. Fig. 1 shows the solutions of the system when the parameters and coefficients use the value in Tab. 1, where Fig. 1a is the evolution of T and h with the time, and Fig. 1b is the track orbit of the SSTA and H20A.

Tab. 1 Representative values of the coefficients and parameters in the ENSO system错误！未找到引用源。

a_1	a_2	μ	a	b	$f_1(t)$	$f_2(t)$
-0.97	-2.84	1.7	0.14	0.56	0	0

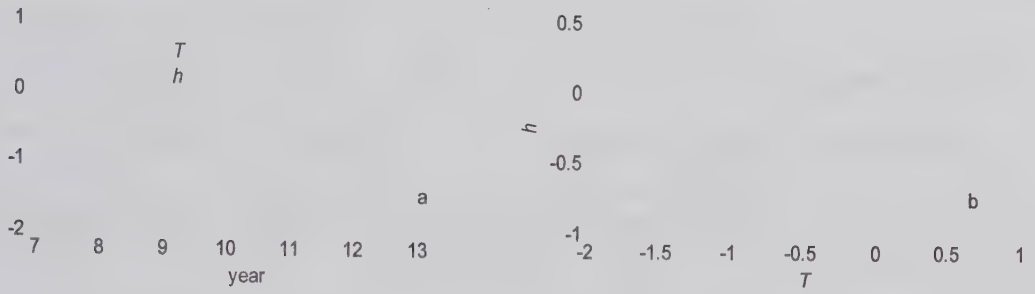

Fig. 1 Limit cycle solution of model WF96 a. Time series of and h; b. The phase orbit of T and h

(Running clockwise as the time goes on)

2 The introduction of adjoint models and derivation of functional gradient

The objective functional used in data assimilation method can be expressed as:

$$J\left[\mu,b,T_0,h_0,f_1,f_2\right]=\frac{1}{2}\int_{t_0}^{t_e}\left[\left(T-T^{obs}\right)^2+W\left(h-h^{obs}\right)^2\right]dt \tag{2}$$

where T^{obs} and h^{obs} represent the observation of SSTA and H20A, and W represents a weight function. The optimal estimation of the parameters and forcing fields is realized by making the forecasting value of the model closest to observed values and the functional achieve the minimum. As the earlier mentioned, the result using usual variational data assimilation method is often not satisfactory for the high non-linearity of WF96, therefore, in accordance with the optimal control idea, a control item of the terminal of state variables is added to the functional, and a new object functional is introduced as follows:

$$\begin{aligned}J\left[\mu,b,T_0,h_0,f_1,f_2\right]=&\frac{1}{2}\int_{t_0}^{t_e}\left[\left(T-T^{obs}\right)^2+W\left(h-h^{obs}\right)^2\right]dt\\&+\frac{\gamma}{2}\left[\left(T-T^{obs}\right)^2+W\left(h-h^{obs}\right)^2\right]\Big|_{t_e},\end{aligned} \tag{3}$$

where $\frac{1}{2}\left[\left(T-T^{obs}\right)^2+W\cdot\left(h-h^{obs}\right)^2\right]\Big|_{t_e}$ is control items of the terminal of the state variable; γ is a control parameter which plays a weighting role between the first items and the second item of the right-hand of formula (3)[12].

In a variety of minimization algorithm (such as the steepest descent, Newton's method and quasi-Newton method, the conjugate gradient method, et al.), the calculation of gradient of the functional with respect to the parameters to be retrieved is necessary, and the gradient can be obtained using variational adjoint method. The gradients of the cost functional (3) with respect to the parameters that will be retrieved are deduced gradually as follows.

2.1 The linear tangent models

Set perturbation to model parameters μ , b , the initial value T_0 , and forcing items i.e. $\mu \to \tilde{\mu} = \mu + \hat{\mu}$, $b \to \tilde{b} = b + \hat{b}$, $T_0 \to \tilde{T}_0 = T_0 + \alpha\hat{T}_0$, $h_0 \to \tilde{h}_0 = h_0 + \alpha\hat{h}_0$, $f_1 \to \tilde{f}_1 = f_1 + \hat{f}_1$, $f_2 \to \tilde{f}_2 = f_2 + \hat{f}_2$, take $\tilde{T}$ and $\tilde{h}$ as the solution of (1) with the above perturbation, and define $\hat{T}$ and $\hat{h}$ as the Gâteaux differential of T and h with respect to $\hat{\mu}, \hat{b}, \hat{T}_0, \hat{h}, \hat{f}_1$ and $\hat{f}$ at point μ, b, T_0, h, f_1, f_2, i.e.

$$\hat{T}(t) = \lim_{\alpha \to 0} \frac{\tilde{T}(t) - T(t)}{\alpha}, \tag{4}$$

$$\hat{h}(t) = \lim_{\alpha \to 0} \frac{\tilde{h}(t) - h(t)}{\alpha}。 \tag{5}$$

and then $\tilde{T}$ and $\tilde{h}$ will satisfy the following initial boundary value problem:

$$\begin{cases} \dfrac{\mathrm{d}\hat{T}}{\mathrm{d}t} = a_1\hat{T} - a_2\hat{h} + 2a_3T\hat{T} - a_3\mu\hat{T}h - a_3\mu T\hat{h} - a_3\hat{\mu}Th + \hat{f}_1 , \\ \dfrac{\mathrm{d}\hat{h}}{\mathrm{d}t} = 2b\hat{h} + \hat{b}(2h - T) - b\hat{T} + \hat{f}_2 , \\ \hat{T}\Big|_{t=t_0} = \hat{T}_0 , \\ \hat{h}\Big|_{t=t_0} = \hat{h}_0 , \end{cases} \tag{6}$$

2.2 Derive the gradients of object functional

The Gâteaux differential of $J\left[\mu, b, T_0, h_0, f_1, f_2\right]$ with respect to $\hat{\mu}, \hat{b}, \hat{T}_0, \hat{h}, \hat{f}_1$ and $\hat{f}$ at point μ, b, T_0, h, f_1, f_2 are:

$$\begin{aligned} J'[\hat{a}_2, \hat{b}, \hat{T}_0, \hat{h}_0, \hat{f}_1, \hat{f}_2] = {} & \nabla_{\mu} J \cdot \hat{\mu} + \nabla_b J \cdot \hat{b} + \nabla_{T_0} J \cdot \hat{T}_0 + \nabla_{h_0} J \cdot \hat{h}_0 \\ & + \int_{t_0}^{t_e} \{\nabla_{f_1} J \cdot \hat{f}_1\} dt + \int_{t_0}^{t_e} \{\nabla_{f_2} J \cdot \hat{f}_2\} dt \quad ; \end{aligned} \tag{7}$$

On the other hand, from the definition of $J\left[\mu, b, T_0, h_0, f_1, f_2\right]$, the following will be getted:

$$\begin{aligned} \nabla J = {} & \int_{t_0}^{t_e} \left[\left(T - T^{obs}\right)\hat{T} + W\left(h - h^{obs}\right)\hat{h} \right] dt \\ & + \gamma \left[\hat{T}\left(T - T^{obs}\right) + \hat{h}W\left(h - h^{obs}\right) \right] \Big|_{t_e} . \end{aligned} \tag{8}$$

2.3 Derive the adjoint equation

Multiple the two equations of (6) with new variable p_1 , p_2 respectively and integrate the equations from t_0 to t_e, and the sum of the two equations will be:

$$\int_{t_0}^{t_e}\left[\frac{d\hat{T}}{dt}p_1+W\frac{d\hat{h}}{dt}p_2\right]dt=\int_{t_0}^{t_e}[\left(a_1\hat{T}-a_2\hat{h}+2a_3T\hat{T}-a_3\mu\hat{T}h-a_3\mu T\hat{h}-a_3\hat{\mu}Th+\hat{f}_1\right)p_1+W\left(2b\hat{h}+\hat{b}(2h-T)-b\hat{T}+\hat{f}_2\right)p_2]dt\ 。 \tag{1}$$

using the initial condition of (6), equation (9) becomes:

$$\begin{aligned}&\int_0^{t_e}\left[\left(\frac{dp_1}{dt}+a_1p_1+2a_3Tp_1-a_3\mu hp_1-bWp_2\right)\hat{T}+\left(\frac{dp_2}{dt}+2bWp_2-a_2p_1-a_3\mu Tp_1\right)\hat{h}\right]dt\\&=p_1(t_e)\hat{T}(t_e)-p_1(t_0)\hat{T}(t_0)+p_2(t_e)\hat{h}(t_e)-p_2(t_0)\hat{h}(t_0)\\&-\int_0^{t_e}\left(\hat{f}_1p_1+\hat{f}_2p_2\right)dt+\hat{\mu}\int_0^{t_e}(a_3\mu hTp_1)dt-\hat{b}W\int_0^{t_e}(2h-T)p_2dt.\end{aligned} \tag{10}$$

Now introduce the following adjoint equation and initial conditions:

$$\begin{cases}\dfrac{dp_1}{dt}=(-a_1-2a_3T+a_3\mu h)p_1+bWp_2-\left(T-T^{obs}\right),\\ \dfrac{dp_2}{dt}=-2bWp_2+\left(a_2+a_3\mu T\right)p_1-W\left(h-h^{obs}\right),\\ p_1\big|_{t=t_e}=-\gamma\left(T-T^{obs}\right),\\ p_2\big|_{t=t_e}=-\gamma W\left(h-h^{obs}\right).\end{cases} \tag{2}$$

using (11) and (10), it is obtained that

$$\begin{aligned}&\int_{t_0}^{t_e}\left[\left(T-T^{obs}\right)\hat{T}+\left(h-h^{obs}\right)\hat{h}\right]dt+\gamma[\hat{T}(T-T^{obs})+W(h-h^{obs})]\big|_{t_e}\\&=-p_1(t_0)T(t_0)-p_2(t_0)\hat{h}(t_0)-\int_{t_0}^{t_e}\left(\hat{f}_1p_1+\hat{f}_2p_2\right)dt\\&+\int_{t_0}^{t_e}(\hat{\mu}a_3\mu hTp_1)dt-\int_{t_0}^{t_e}\left(W\hat{b}2hp_2\right)dt.\end{aligned} \tag{12}$$

Comparing formula (12) with (7) and (8), the gradients of J with respect to μ, b, T_0, h_0, f_1, f_2 can be obtained:

$$\begin{aligned}&\nabla_\mu J=a_3\mu hTp_1,\\&\nabla_b J=-(2h-T)p_2,\\&\nabla_{T_0}J=p_1(t_0),\\&\nabla_{h_0}J=p_2(t_0),\\&\nabla_{f_1}J=-p_1,\\&\nabla_{f_2}J=-p_2.\end{aligned} \tag{13}$$

Letting $R=(R_1,R_2,\cdots,R_6)=(\mu,b,T_0,h_0,f_1,f_2)$, with these gradients and using appropriate descending algorithms:

$$R_j^i=R_j^{i-1}-\nabla_{R_j}J\big|_{R^{i-1}}\rho_j^i, \tag{3}$$

where ρ_j^i $(j=1,2,\cdots,6)$ is the step length of iteration i and R_j^0 $(j=1,2,\cdots,6)$ is the initial value, the results of the retrieval will be obtained at last.

Now a brief description of the retrieval of the initial values, model parameters and the forcing items is given as the following:

Step 1: Give the initial guess value of model parameters $\mu(t)$ and $b(t)$, the initial value T_0 and h_0, the forcing items $f_1(t)$ and $f_2(t)$.

Step 2: Integrating model 错误！未找到引用源。 using the new guess value, and save the results of $T(t)$ and $h(x)$ predicted by the integration.

Step 3: Integrating the adjoint model 错误！未找到引用源。 from $t = t_c$ to $t = t_0$ reversely using $T(x)$, $h(x)$ and $T^{obs}(x)$, $h^{obs}(x)$, and then the adjoint variables $p_1(t)$ and $p_2(t)$ will obtained.

Step 4: Calculate the step length using appropriate descending algorithms, and get the new values of the variables to be retrieved by making the iteration in accordance with (14).

Step 5: Calculate the gradients of J with respect to the variables to be retrieved in accordance with (13) If termination conditions (such as the requisite accuracy has reached or the number of iterations has reached the predefined maximum number) is satisfied, terminate procedures; Other wise begin a new round of the iteration cycle from Step 2 using the new value of $\mu(t)$, $b(t)$, T_0, h_0, $f_1(t)$, $f_2(t)$.

3 Numerical experiment

3.1 Experiment design

To illustrate the effect of the terminal control item on the results, two experiments are carried out where in experiment 1 $\gamma = 0$ and in experiment 2 $\gamma = 0.4$ (the value of γ is just taken to be equal to the ratio of the first term and the second term in the right hand of the object functional错误！未找到引用源。. For more accurate or sophisticated methods of the selection of γ, please see reference[12]. The values of other parameters in the two experiments are identical and given in the following remark:

(a) For $T^{obs}(x)$ and $h^{obs}(x)$, their values are distilled from the TAO (Tropical Atmosphere and Oceans) data with the resolution of 1°×1°×5d and period from 1991 to 1999. The time series of SSTA and H20A are obtained by averaging the sea surface temperature anomaly and the thermocline depth anomaly in the region 160°E - 100°W, 5°S - 5°N. Fig. 2 shows the results of the average where SSTA and H20A are normalized by 2.5 and 35 respectively. From Fig. 2b it can be seen that the ENSO events at 1997 - 1998 has the similar behavior with the prediction of WF96 in the phase plane (the observations in 1997 - 1998 is shown separately in Fig. 4). So in the paper, the observations in this period are used as $T^{obs}(x)$ and $h^{obs}(x)$ (To facilitate comparison with the predicted value of WF96, the value of SSTA and H20A is set to the normalized observation minus 1.0 and 0.57 respectively).

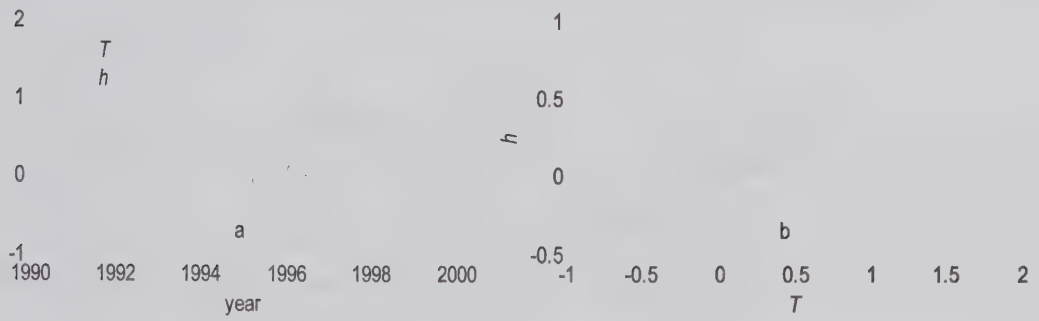

Fig. 2 Data of T and h distilled from TAO

a. The time series of T and h ; b. The phase orbit of T and h (Running clockwise as the time goes on)

b) The values of model parameters are give in accordance with Tab. 1; the guess values of forcing items $f_1(t)$ and $f_2(t)$ is set to 0; initial model variables is set to $T_0 = -1.27$ and $h_0 = -0.6$ according to the observations .

c) The value of W is given to 1.2 which is approximate to the ratio of the norm of SSTA to H20A. The reason for using this value is to ensure that $T(x)$ and $h(x)$ can play an equally important role in the objective function.

d) In this paper, only the retrieval of b, $f_1(t)$ and $f_2(t)$ is carried out.

e) For the descending algorithm, the Quasi-Newton algorithm is used [13].

3.2 Experimental results

The results of the inversion for parameters b and forcing items $f_1(t)$ and $f_2(t)$ are shown in Fig. 3, and the predicted values for SSTA and H20A with the optimized parameters are shown in Fig. 4. To facilitate comparison, the observed values, the predicted value before parameter inversion, the predicted value after parameter inversion with $\gamma = 0.4$ and the predicted value after parameter inversion with $\gamma = 0.4$ are shown in one figure.

It can be seen from Fig. 3 that there are obvious difference for inversion results of parameters b and forcing items $f_1(t)$ and $f_2(t)$ particularly in the second half of the time with $\gamma = 0$, $\gamma = 0.4$, the parameters b have the value departure from the initial value to different directions.

From Fig. 4, it can be seen that both the predicted SSTA and H20A have values closer to the observations after the model parameters have been retrieved. In the time series plotting Fig. 4b, the predicted value of H20A in latter half of the plotting (after the inversion prediction value) has poor improvements when $\gamma = 0$, while when $\gamma = 0.4$ the condition improved markedly especially. From the phase plane Fig. 4c, the effect is particularly evident, where due to the predicted H20A when $\gamma = 0$ has large difference at the end of time relative to the observation which leads to the predicted orbit departing from observed orbit, the predicted orbit has a good agreement with observed orbit when $\gamma = 0.4$. For the object functional, $J = 29.38$ before the retrieval, while $J = 5.32$ when $\gamma = 0$ and $J = 5.32$

when $\gamma = 0.4$ after the retrieval.

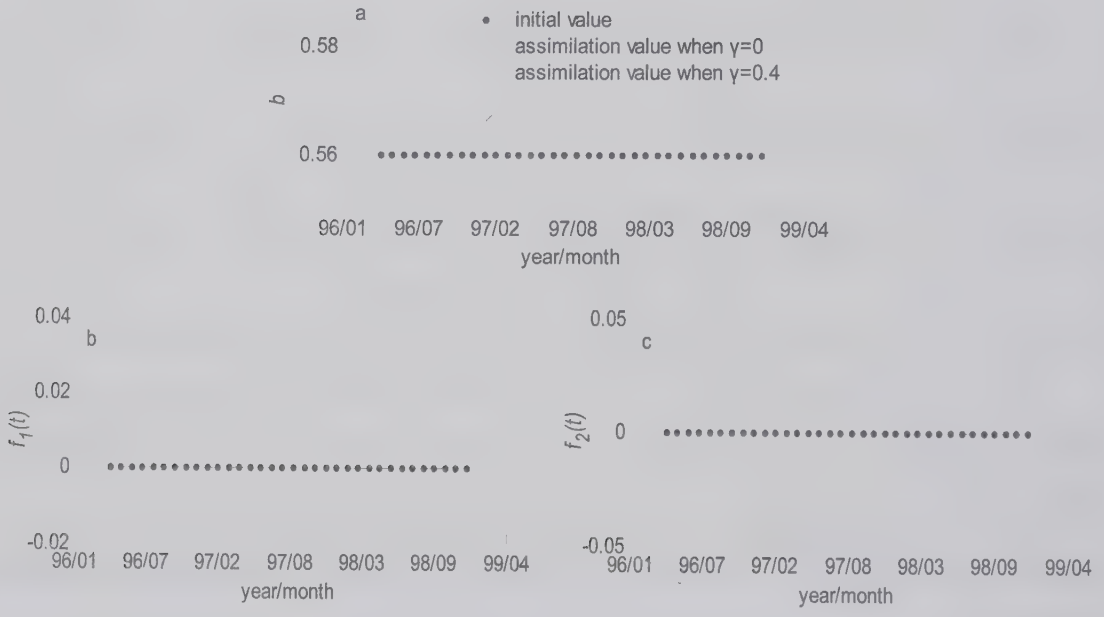

Fig. 3 Results of the inversion of model parameters

a. parameter b ; b. parameter $f_1(t)$ c. parameter $f_2(t)$

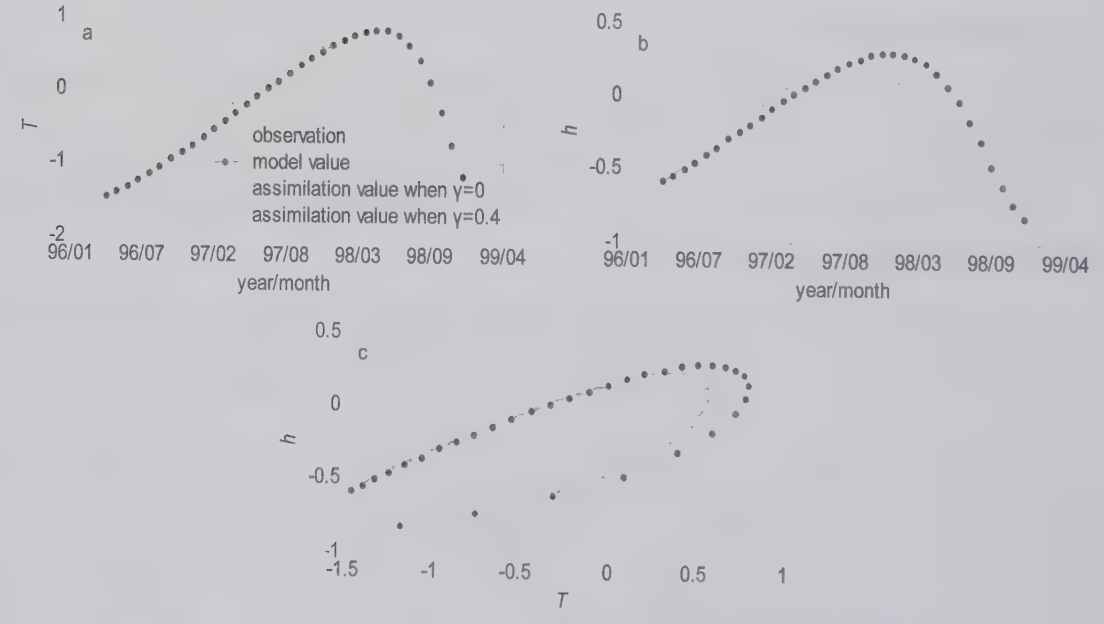

Fig. 4 Comparison of the values of observation and the values predicted by the model

a. SSTA; b. H20A c. The phase orbit of T and h (Running clockwise as the time goes on)

4 Conclusion

Although differences still exists between the predicted value of model variables and the observations due to the model itself or the accuracy of the retrieval, but the results still have great improvements using the data assimilation method combined with the optimal control idea. The improvements are embodied in both compensating the predicted errors caused by the inaccuracy of model parameter and in the retrieval of model parameters and forcing items. The method provides a considerable reference for improving more complicated model in practical conditions

Acknowledgements

The study was supported by the National Science Foundation of China (40775023) and the Science Foundation for Doctor of the Institute of Meteorology of PLA University of Sci. and Tech.

Reference

[1] Min J Z, Sun Z B, Gao Q J, et al. A Global Air-Sea Coupled Model System (NIM/COAMS) II. Simulation of Inter-annual Variations [J]. Journal of Nanjing Institute of Meteorology, 2005, 28(6): 721-729.

[2] Philander S G H. Unstable air-sea interaction in the tropicals [J]. J Atmos Sci, 1984, 41(2): 604-113.

[3] Wyrtki. El Nino-the dynamic response of the equatorial pacific ocean to atmospheric forcing [J]. J Phys Oceanogr, 1975, 5(2): 572-84.

[4] Suarez M J, Schopf P S. A delayed action oscillator for ENSO [J]. J. Atmos. Sci., 1988, 45(21): 3 283-3 287.

[5] McCreay J P, Anderson D J L. A simple model of El Nino and the southern oscillation [J]. Mon Wea Rev, 1984, 112(2): 934 -946.

[6] Huang S X, Han Wei, Wu R S. Theoretical Analyses and Numerical Experiments of Variational Assimilation for One-Dimensional Ocean Temperature Model [J]. Science in China D, 2003, 33(9): 903-911.

[7] Zhu J. The Improvement Made by a Modified TLM in 4DVAR with a Geophysical Boundary Layer Model [J]. Adv Atmos Sci, 2001, 19(4): 563-582.

[8] Zebiak S E, Cane M A. A model El Nino-Southern Oscillation [J]. Mon Wea Rev, 1987, 115(10): 2262-2278.

[9] Yue C J, Lu W S, Tao L. Evaluation of the Prediction Performance of a Simple Coupled Ocean-Atmosphere Model. Journal of Nanjing Institute of Meteorology, 2005, 28(5): 704-709.

[10] Wang B, Zheng F. Chaotic oscillations of the tropical climate: A dynamic system theory for ENSO [J]. J. Atmos. Sci., 1996, 53(19): 2786-2802.

[11] Huang S X, Han W. Theoretical analysis and calculation of an nonlinear self-excited oscillation model for equatorial Eastern Pacific air-sea coupling, Proceedings of the 3rd International Conference on Nonlinear Mechanics [C]. Shanghai: Shanghai University Press, 1998,474-478.

[12] Marquardt D W. An algorithm for least-squares estimation of nonlinear parameters [J]. J Appl Math, 1963, 11(2): 431-441.

[13] Gilbert J C, Lemarechal C. Some numerical experiments with variable storage quasi-Newton algorithms [J]. Math Programming, 1989, 45(3): 407-435.

变分同化方法反演海气耦合模型参数的研究

杜华栋，黄思训，蔡其发，程 亮

（1. 中国人民解放军理工大学气象学院，江苏 南京 211101；2. 南京信息工程大学 江苏省气象灾害重点实验室，江苏 南京 210044；3. 北京 2433 信箱，北京 100081）

摘 要：采用变分资料同化技术，结合最优控制思想，对一个海气耦合模型的模式参数和强迫项进行了反演，结果表明，采用该方法对模式进行优化，既可以补偿模式参数不准确性给预报带来的误差，又可以对模式参数本身进行修正和估计，为将来在实际应用中改善更复杂的预报模式、提高预报准确率提供了一个可借鉴的思路。

关键词：变分资料同化；海气耦合模型；最优控制

Declaration of Correction

The paper named “preliminary Study of Microzooplankton Grazing and Community Composition in the North of South China Sea in Autumn” was written by SU Qiang which was published on Marine Science Bulletin in Vol. 9, No. 1 on Oct. 2007, there are some units need to be correct. In the section 3.3, the unit of Ciliates abundance should be “ind / L”. And also in Tab.2, the unit of abundance should be “ind / L”. In addition, the unit of Ciliates abundance should be “ind / L” in the English and Chinese abstracts.

更 正 声 明

兹有作者苏强于我刊 2007 年 10 月第 9 卷第 2 期上发表的文章 “Preliminary Study of Microzooplankton Grazing and Community Composition in the North of South China Sea in Autumn”一文中，在文章的 3.3 一节，“Ciliates abundance”的单位应为“ind/L”。同样在 Tab. 2 中 abundance 后面的单位也应为“ind/L”。另外，中英文摘要中，纤毛虫丰度（Ciliates abundance）的单位也应为“ind/L”。特此更正！

Numerical Study on Tides in the Taiwan Strait and its Adjacent Areas

ZHU Jia[1, 2], HU Jian-yu[1, 2*], ZHANG Wen-zhou[2], ZENG Gan-ning[2,3], CHEN De-wen[1], CHEN Jin-quan[1], SHANG Shao-ping[1]

1. *Department of Oceanography, Xiamen University, Xiamen* 361005, *Fujian Province, China;*

2. *State Key Laboratory of Marine Environmental Science (Xiamen University), Xiamen* 361005, *Fujian Province, China;*

3. *Marine Technology, Zhejiang University of Technology, Hangzhou 310014, Zhejiang Province, China*

Abstract: Diurnal and semi-diurnal tides in the Taiwan Strait and its adjacent areas are calculated by using a two-dimensional finite-difference model. Compared with data of more than 20 observation stations around the Taiwan Strait, the model-produced results agree quite well with those of previous researches using observational data from coastal tidal gauge stations. According to the results, the co-tidal and co-range charts are given. Furthermore, the characteristics of 8 major tidal constituents have been illuminated respectively. The result shows that: (1) The tide motion can be attributed to the interaction between the degenerative rotary tidal system in the north and the progressive tidal system in the south. (2) The southward and northward tidal waves of semi-diurnal tide converge in the middle of the Taiwan Strait while the diurnal tidal waves propagate southwestward through the Taiwan Strait and the Luzon Strait. (3) The maximum amplitude of semi-diurnal tides exists at the area between the Meizhou Bay and Xinghua Bay, and that of diurnal tides appears in the region to the east of the Leizhou Peninsula. (4) The patterns of co-tidal and co-range charts of N_2, K_2 and P_1, Q_1 tidal constituents are similar to those of M_2, S_2 and K_1, O_1 tidal constituents, respectively.

Keywords: Taiwan Strait and its adjacent areas, tidal characteristics, model

The type of the tides from the Pacific Ocean becomes more complex when the tidal wave enters the research region, Taiwan Strait and its adjacent areas, affected by the complex bottom topography, devious coastal boundary, continental shelf and Taiwan Island.

Several kinds of studies on tides in the Taiwan Strait and its adjacent areas have been conducted these years, including four study methods: the analysis of historic data, numerical modeling, the analysis of satellite data, and the assimilation of numerical modeling result with satellite data. On the basis of the tidal data cited from *the tide table of British Navy* and the historic data from the domestic and overseas tidal observation station, several scholars analyzed the basic features of tides and tidal currents in the South China Sea and the Taiwan Strait (e.g. Zheng et al., 1982; Ding, 1983; Yu et al., 1984; Liu et al., 2002). Ye et al (1985), Ye and Ye (1986), Ye (1990) and Yan and Wu (1995) studied the semi-diurnal and

Received on March 13, 2008

*Corresponding author: hujy@xmu.edu.cn

diurnal tides in the Taiwan Strait. Fang et al. (1985, 1986, 1994) established two models with the resolution of 10 nm×10 nm and 0.25° × 0.25° for the M_2, K_1, O_1 tidal constituents of the Taiwan Strait and for the m_1, M_2 tidal constituents of the South China Sea, respectively, and then presented the tidal charts of M_2, K_1 tidal constituents in the studied area. Cao et al. (1990) simulated the semi-diurnal and diurnal tidal constituents in the northern part of the South China Sea. Zhao et al. (1995) calculated four major tidal constituents in the South China Sea with the resolution of 1° × 1° and 30′ × 30′, respectively. Qian et al. (2000) draw the tidal charts of nine tidal constituents in the East China Sea. Jan et al. (2004) developed a three-dimensional model for current and tide in the Taiwan Strait with the resolution 3 km × 3 km. Sha et al. (2000, 2001, 2002) studied the diurnal and semi-diurnal tides around Taiwan by using the Princeton Ocean Model (POM), and then Yu et al. (2003) studied the effect of the tide character by the sea level changes, using the same model, POM. On the other hand, scientists also applied the satellite data for the tide study. Li et al. (2002) analyzed the TOPEX/POSEIDON (T/P) data to get the characters of the four main tidal constituents around Fujian and Taiwan. Hu et al. (2001) and Fang et al. (2004) obtained a large-scale tidal chart in the China Seas and its adjacent sea area by using the 6-years and 10-years T/P data, respectively. Wu et al. (2003, 2004) optimized the boundary condition and the bottom friction coefficient synchronously and simulated the m_1, M_2, S_2, K_1, O_1 tidal constituents in the SCS, assimilated with T/P data and considered the tidal force. Besides, Lin et al. (2001) studied the abnormal amplitude increasing phenomenon of the semi-diurnal tide along the west coast of Taiwan from theoretic and model aspects. Jan et al. (2004) discussed the mechanism of the abnormal amplitude increasing of the M_2 tidal constituent in the Taiwan Strait, and pointed out that the main reason was the coexistence of the progressive wave in the west and the standing wave in the east of strait. Zeng et al. (2004) summarized the research results of M_2 tidal constituent in the Taiwan Strait in recent years.

Taiwan Strait is the channel between the northern SCS and the southern East China Sea, and the tide motion can be attributed to the interaction of the tidal systems both from the north and the south. We consider the Taiwan Strait and its adjacent areas as an entire region and simulate 8 major tidal constituents using a two-dimensional finite-difference model. Then the tidal features for 8 major tidal constituents can be drawn with the 6′×6′ resolution according to the simulation results.

1 Brief introduction of the model

1.1 Model domain

The computational region of this model covers 110 °E - 130°E, 18 °N - 30°N, including the Taiwan Strait, the southern East China Sea, the deep water area east of Taiwan Island, and the Luzon Strait. The model domain is shown in Fig. 1, demonstrating that the water depth is up to one thousand meters offshore the eastern Taiwan Island, decreases westward to tens of meters in the Taiwan Strait, and increases as deep as thousands meters in the southern deep sea of the Taiwan Bank. The tide motion becomes complex because of the rough bottom topography.

1.2 Model equation

$$\frac{\partial \zeta}{\partial t}+\frac{\partial Hu}{\partial x}+\frac{\partial Hv}{\partial y}=0 \tag{1}$$

$$\frac{\partial u}{\partial t}+u\frac{\partial u}{\partial x}+v\frac{\partial u}{\partial y}-fv=-g\frac{\partial \zeta}{\partial x}-\frac{\tau_{bx}}{\rho H} \tag{2}$$

$$\frac{\partial v}{\partial t}+u\frac{\partial v}{\partial x}+v\frac{\partial v}{\partial y}+fu=-g\frac{\partial \zeta}{\partial y}-\frac{\tau_{by}}{\rho H} \tag{3}$$

where x, y are the horizontal axises of Descartes, which is positive eastward, northward, and upward respectively for x, y and z axis; t stands for time; u, v for average mean velocity in x, y direction respectively:

$$u=\frac{1}{H}\int_h^{\zeta} u' dz\,; \quad v=\frac{1}{H}\int_h^{\zeta} v' dz \tag{4}$$

here, ζ stands for the water level calculated from the undisturbed sea surface; $H=\zeta+h$, is the height of the water column, h is water depth; g is the acceleration of gravity; f is the Coriolis parameter, $f=2\Omega\sin\varphi$, φ stands for the latitude, $\Omega=7.29\times10^{-5}/s$. In this model, the bottom friction is:

$$\tau_b=\rho g C^{-2}\left|\vec{U}\right|\vec{U}, \qquad C=\frac{1}{n}h^{\frac{1}{6}} \tag{5}$$

here *n* is the Manning coefficient, *n*=0.03; ρ is the density of seawater; $\vec{U}$ is the velocity of the vertical flow; C is the bottom drag coefficient.

1.3 Initial and boundary condition

The model begins running with the initial condition, that is, $\zeta=u=v=0$. We suppose the boundary is a zigzag line, and goes through u and v points, $u=0$ or $v=0$. In another word, we make the value of the average vertical velocity in normal direction to be zero. sFinally, we consider the entire water boundary as being forced by the water level:

$$\zeta_i=H_i\cos(\sigma_i t+v_{0i}-g_i) \qquad (i=1,2,3.....8) \tag{6}$$

In this formula, H_i is the amplitude of the tidal constituent i, g_i is its phase, σ_i is the angular velocity; and v_{0i} is the astronomical initial phase, which can be calculated through the formulae (Fang et al., 1986) of astronomical basic factor.

In this model, we adopt an implicit difference method, second-order accurate and unconditionally stable, staggered grid (C grid), with the resolution 6′×6′ in this research region. It can be divided into

201×121 grid points, and the distance between each grid point is about 11 km. The water depth of each grid point is the average depth of that gird. The time step is set to be 200 s.

This research region includes a long opening boundary. How to get the appropriate value of the forcing boundary is a key step in the numerical calculation of astronomical tide. In our model, we adopt a global model's result, NAOTIDE, whose resolution is 0.5° × 0.5°. We input the interpolated result as the boundary condition, and then slightly adjust the boundary value through a series of numerical experiments. After the model calculation being stable, we output one month of water level value, with one hour interval, then analyze the harmonic constants with the Least Square Method (Fang et al., 1986), and finally draw the co-tidal charts of the eight major tidal constituents for analyzing the character of each tide.

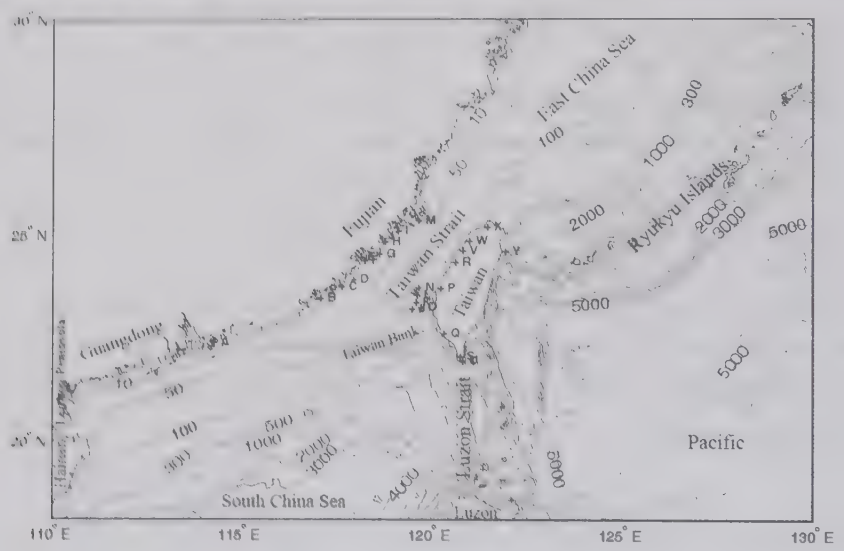

Fig. 1 Topography of the model domain

(A-ShenZhen, B-NanAo, C-DongShan, D-FuTou Bay, E-XiaMen, F-JinMen, G-WeiTou, H-QuanZhou, I-Meizhou, J-Xiji Island, K-Jiangjun'ao, L-Magong, M-Xinghua Bay, N-Baisha Island, O-Dongji, P-Kouhu, Q-Gaoxiong, R-Taizhong, S-Checheng, T-Houbi Lake, U-Dabanlie, V-Houlong, W-Xinzhu, X-Danshui, Y-Su'ao)

2 Comparison between calculated result and observed data

In the validation process, we compare the calculated result with the observation derived harmonic constants which extracted from the book named *Tide application along China coast* written by Wang (1986) (the data were from Royal Navy tide table, reports of Japanese waterway department and publication of the USSR etc.). The comparison of four major tidal constituents (M_2, S_2, K_1, O_1) is shown in Tab. 1.

The comparison result shows: the average absolute deviations of amplitude and phase for M_2 tidal constituent are 4.1 cm and 5.6°, respectively. The absolute amplitude deviation ranges from 0.5 cm to 3 cm; the minimum absolute deviation of amplitude is 0.1 cm at Station Dabanlie, and the maximum is

16.4 cm at Station Xiamen because the station's grid point does not match the geographical position. The absolute phase deviation ranges from 0.6 to 5.5°, with the maximum deviation 16.5° at Station Kouhu. The average absolute deviations of amplitude and phase for S_2 tidal constituent are 7.4 cm and 10.5°, respectively. The absolute amplitude deviations of most stations are less than 10 cm, the maximum and minimum deviations are 19.4 cm and 0.6 cm at Station Nan'ao and Danshui respectively; the maximum deviation of phase is 23.5° at Station Jiangjun'ao. The average absolute deviations of amplitude and phase for K_1 and O_1 tidal constituents are 2.3 cm and 6.3°, 3.2 cm and 7.5°, respectively.

For the rest four tidal constituents (P_1, Q_1, N_2, K_2), due to the lack of the harmonic constants from observation data, we compare the model result indirectly. Wang (1986) and Fang et al. (1986) proposed similar empirical formulae to induce the harmonic constants of P_1, Q_1, N_2, K_2 tidal constituents from M_2, S_2, K_1, O_1 tidal constituents. Their empirical formulae are the same for amplitude, but quite different with each other for phase. Here we use the amplitude empirical formulae as equations. (7) - (10) to calculate the harmonic constants of P_1, Q_1, N_2, K_2 tidal constituents through M_2, S_2, K_1, O_1 tidal constituents , then compare with our model results, and finally get the average absolute deviations of each tidal constituent as shown in Tab. 1. The average absolute deviation of amplitude of P_1, Q_1, N_2, K_2 tidal constituents are 1.2 cm, 1.0 cm, 4.5 cm and 5.3 cm, respectively.

$$H_{p_1} = 0.3333 H_{k_1} \qquad g_{p_1} = g_{k_1} - 0.075(g_{k_1} - g_{o_1}) \tag{7}$$

$$H_{Q_1} = 0.2000 H_{o_1} \qquad G_{Q_1} = G_{k_1} - 1.499(g_{k_1} - g_{o_1}) \tag{8}$$

$$H_{N_2} = 0.2000 H_{M_2} \quad g_{N_2} = g_{M_2} \tag{9}$$

$$H_{k_2} = 0.2725 H_{s_2} \qquad g_{k_2} = g_{s_2} - 0.081(g_{s_2} - g_{M_2}) \tag{10}$$

According to the statistics, the model result of M_2 matches the observation data quite well, as well as the results of K_1 and O_1 tidal constituents. The model results of P_1 and Q_1 tides are close to the value induced from the empirical formulae, the distribution patterns also accord with the co-tidal features obtained from the satellite altimeter data; but the model amplitudes of N_2 and K_2 are a little larger than the theoretic value.

3 Co-tidal and co-range charts for each tidal constituent

3.1 M_2 tidal constituent

As shown in Fig. 2a, the amplitude of M_2 tidal constituent is greater nearshore but smaller offshore. The water depth is thousand meters off the east coast of the Taiwan Island so the amplitude there is less than 60 cm. There's a small amplitude area near the northeast cape of Taiwan Island, the amplitude is no more than 40 cm. In the Taiwan Strait, the tidal amplitude zooms as the water depth decreases, especially

at the Taiwan Bank area. This figure also shows that the amplitude in the west coast is larger than that in the east coast, caused by the Coriolis force. Near the Meizhou Bay and the Xinghua Bay, the amplitude is more than 200 cm, and the maximum amplitude (223 cm) appears around the (119.5ºE, 25.2ºN) sea area. At the shelf area of northern South China Sea, the amplitude increases from 20 cm to 80 cm as a result of "shelf effect", and the large amplitude appears close to the west Guangdong Province.

Tab. 1 Comparisons of calculated and observed harmonic constants for each tidal constituent

station	Lon&lat		gridding		Absolute Error / M_2		Absolute Error / S_2		Absolute Error / K_1		Absolute Error / O_1		Amplitude Absolute Error / cm			
	E	N	I	J	H / cm	G / °	H / cm	G / °	H / cm	G / °	H / cm	G / °	P_1	Q_1	N_2	K_2
Shenzhen	114°12′	22°24′	42	44	3.82	5.37	1.18	6.49	0.99	0.77	3.95	7.10	0.57	-1.11	0.19	3.71
Nan'ao	117°01′	23°28′	70	55	12.40	14.98	19.43	19.28	0.93	7.33	1.17	5.13	1.00	-0.10	-7.89	8.71
Dongshan	117°34′	23°45′	76	58	4.43	0.65	18.46	4.99	0.50	6.85	1.50	8.57	1.00	-0.11	-7.22	8.76
Futou Bay	117°52′	23°55′	79	59	7.22	2.04	11.73	1.73	0.19	3.47	4.83	9.77	0.60	-1.30	-3.20	8.54
Xiamen*	118°04′	24°27′	81	64(63)	16.41	0.82	10.18	0.82	4.17	2.80	7.95	11.50	2.20	-2.10	-2.86	8.07
Jinmen	118°10′	24°23′	82	64	2.88	0.81										
Weitou	118°34′	24°32′	86	65	2.17	0.72	14.17	1.08	3.75	2.63	7.59	11.22	2.10	-2.10	-8.10	10.07
Quanzhou*	118°43′	24°49′	87	68(66)	2.94	14.22	7.28	6.19	3.69	0.84	7.53	14.74	2.10	-2.03	-8.69	10.11
Meizhou*	119°03′	25°05′	91	71(70)	0.46	5.30	5.61	17.49	3.72	15.51	4.41	5.24	2.00	-1.40	-12.70	9.98
Xiji Island	119°25′	23°13′	94	52	9.38	7.38										
Jiangjun'ao	119°31′	23°22′	95	54	8.61	4.72	9.85	23.52	2.57	4.52	0.13	6.33	1.60	-0.38	-3.00	5.13
Magong	119°33′	23°33′	95	55	0.07	2.91	2.50	17.16	0.03	6.56	0.09	5.03	0.70	-0.40	-5.28	2.96
Xinghua Bay	119°35′	25°20′	96	73	1.25	7.13	4.08	17.75	3.68	16.33	4.15	4.63	2.00	-1.41	-16.60	7.04
Baisha Island*	119°36′	23°44′	96	56(57)	5.69	1.04	0.66	0.28	2.71	8.87	0.11	7.10	1.60	-0.38	0.60	3.33
Dongji	119°40′	23°15′	97	53	0.74	2.52										
Mazu	119°55′	26°10′	99	82			11.85	11.28	1.02	3.76	2.05	2.76	0.40	-0.95	-6.97	2.47
Kouhu	120°10′	23°42′	102	57	0.83	16.48	8.91	1.58	4.69	7.55	5.19	8.51	2.20	-1.50	-7.08	6.76
Gaoxiong	120°16′	22°37′	103	46	7.15	7.50	2.45	22.44	4.54	17.94	3.95	14.71	2.17	-1.20	0.60	-0.24
Taizhong	120°33′	24°20′	105	63	0.20	1.91										
Checheng	120°41′	22°04′	107	41	2.03	5.48	4.75	14.28	1.43	10.30	1.94	6.17	0.27	-0.90	1.69	-0.63
Houbi Lake	120°45′	21°57′	108	39	2.18	10.96										
Dabanlie	120°45′	21°58′	108	40	0.06	9.25	4.55	9.08	2.42	1.96	0.82	10.01	0.03	-0.80	1.84	-0.10
Houlong*	120°45′	24°37′	108	67(66)	8.89	5.11	1.16	13.38	2.86	0.46	2.12	3.92	1.60	-0.97	-13.60	7.95
Xinzhu	120°55′	24°51′	109	69	0.78	1.44										
Danshui*	121°24′	25°11′	114	73(72)	1.06	4.54	0.57	12.14	0.21	4.63	0.74	1.68	0.50	-0.48	4.62	2.63
Su'ao*	121°52′	24°35′	119	65(66)	1.41	5.53	7.67	8.28	1.16	2.27	3.80	6.06	0.20	0.11	3.73	-0.31
Average					4.1	5.6	7.4	10.5	2.3	6.3	3.2	7.5	1.2	1.0	4.5	5.3

remark: '*' stands for the station whose location does not match the real observation station, using the closest gridding point instead.

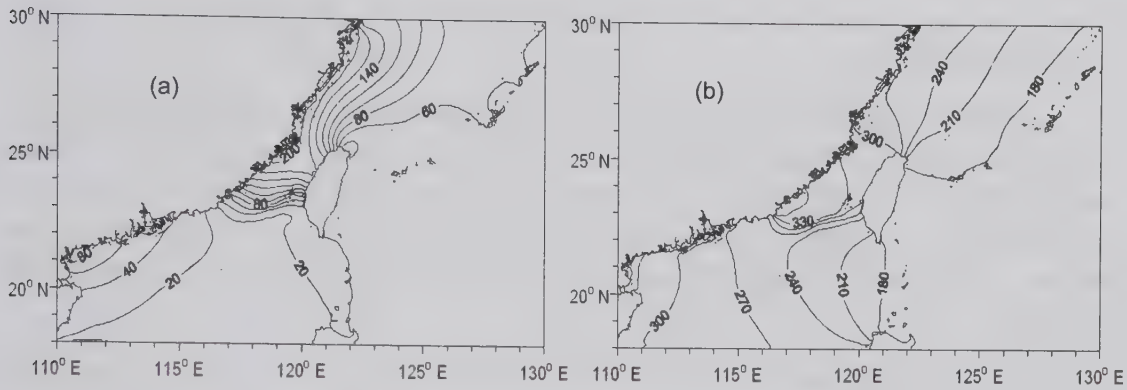

Fig. 2 Co-tidal and co-range charts of M_2 tidal constituent

(a) amplitude (cm); (b) phase (°) referred to 120°E.

Fig. 2b indicates that the co-range lines distribute sparsely to the east of the Taiwan Island, suggesting the tidal waves propagate quickly in deep water. In the southern sea area of the Taiwan Island, the co-range lines distribute evenly, and the tidal waves propagate westward from the Luzon Strait to the east coast of the Hainan Island. In the northern area of Taiwan Island, the co-range lines rotate anticlockwise around the north cape of the Taiwan Island, with the phase increasing from 180° to 300°, so as to become a degenerative rotary tidal system (Shen, 1980). As the north and south tidal waves meet around the Taiwan Bank, the distribution of the co-range lines becomes denser as the water depth being shallower.

Obviously, the amplitude of M_2 tidal constituent is large in the west but small in the east, while large in the north but small in the south of Taiwan Strait. The amplitude increases as the south and north tidal waves meet in the middle of the Taiwan Strait, and reach the maximum near the Meizhou Bay-Xinghua Bay of Fujian Province. The time of high tide defers gradually from south or north to the middle part of the Taiwan Strait, and the latest high tide place is near Dongshan, Fujian Province.

Compared with the other research results, the distribution pattern of the co-tidal and co-range lines are accordant with the results of Fang et al. (1985) and Sha et al. (2000). The maximal amplitude appears near the Meizhou Bay-Xinghua Bay, which is also the same as that from previous results. In this model, the maximal amplitude is 223 cm, close to the result of Fang et al. (1985) and Sha et al. (2000), whose maximal amplitude is 200 cm and 240 cm, respectively. However, there still exist some divarications about the influence range and strength of north and south tidal waves in the Taiwan Strait. Some scholars considered that the north tidal wave is dominant and can spread to the Taiwan Bank, but some others insisted that the south tidal wave is stronger than ever understood, and the influence range is farther into the northern part of the Taiwan Strait. But the influence range of the two tidal waves cannot be distinguished directly; it will be discussed with further consideration of the tidal current distributions.

3.2 S_2 tidal constituent

S_2 tidal constituent is also a semi-diurnal tide, so its patterns of the amplitude and phase (Fig. 3) are similar to those of the M_2 tidal constituent. The amplitude of S_2 ranges from 10 cm to 20 cm in the east area of the Taiwan Island. There is a small amplitude area near the north cape of the Taiwan Island, for the amplitude there is smaller than 10 cm. The amplitude is higher than 30cm in the Taiwan Strait, and the maximum amplitude (80 cm) appears around the Xinghua Bay, almost the same as that of M_2 tidal constituent.

The co-range lines rotate anticlockwise around the north cape of the Taiwan Island, with the phase increasing from 210° to 360°, and become a degenerative rotary tidal system there (Shen, 1980), which is more obvious than that in M_2 tidal constituent. There exists an amphidromic point in the southwest of Taiwan Island, but such an amphidromic point was not mentioned by Ye et al. (1985), Wu et al.(2004) and Sha et al. (2001) (see Fig. 4a) . However, the present model result is similar with that of Hu et al. (2001), which inferred from the T/P altimeter data that there are two obvious amphidromic points near the Taiwan Bank (Fig. 4b).

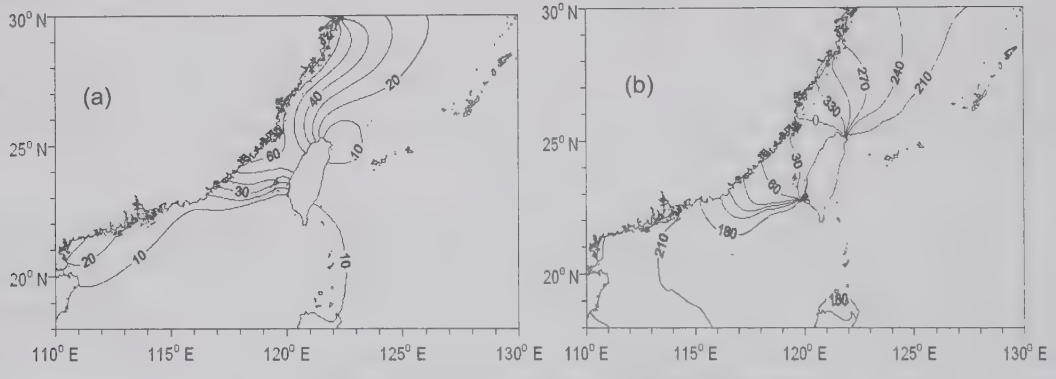

Fig. 3 Co-tidal and co-range charts of S_2 tidal constituent

(a) amplitude (cm); (b) phase (°) referred to 120°E

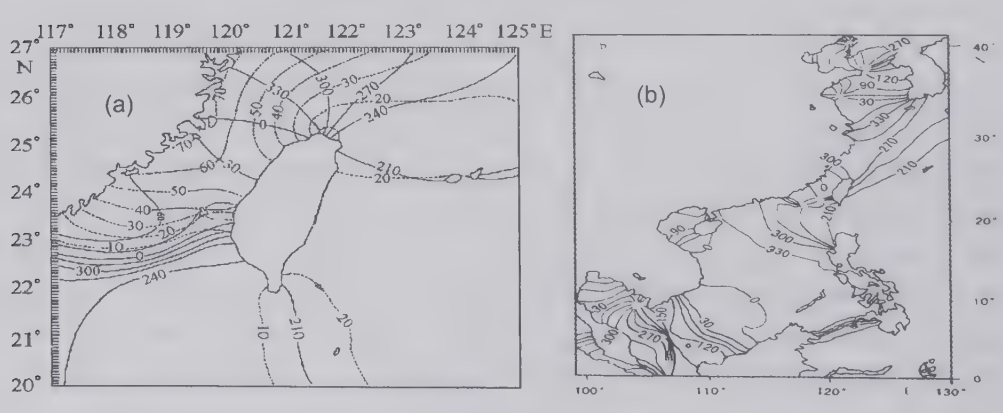

Fig. 4 Co-tidal and co-range charts of S_2 tidal constituent in the Taiwan Strait.

(a) cited from Sha et al. (2001); (b) cited from Hu et al. (2001)

3.3 K_1 and O_1 tidal constituents

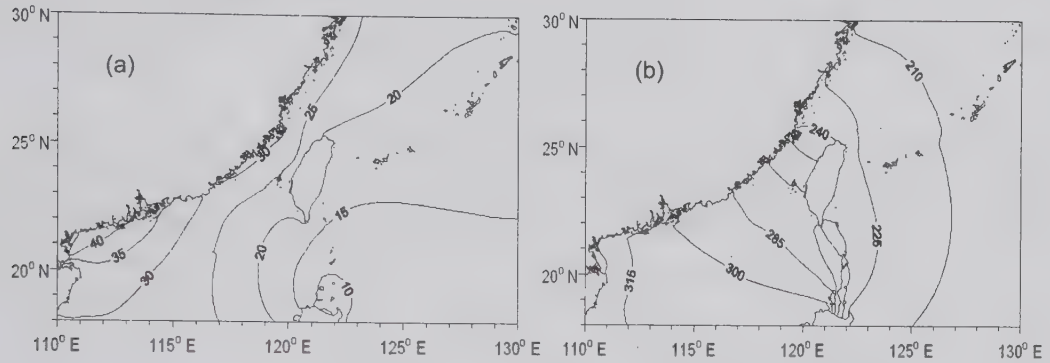

Fig. 5 Co-tidal and co-range charts of K_1 tidal constituent

(a) amplitude (cm); (b) phase (°) referred to 120°E

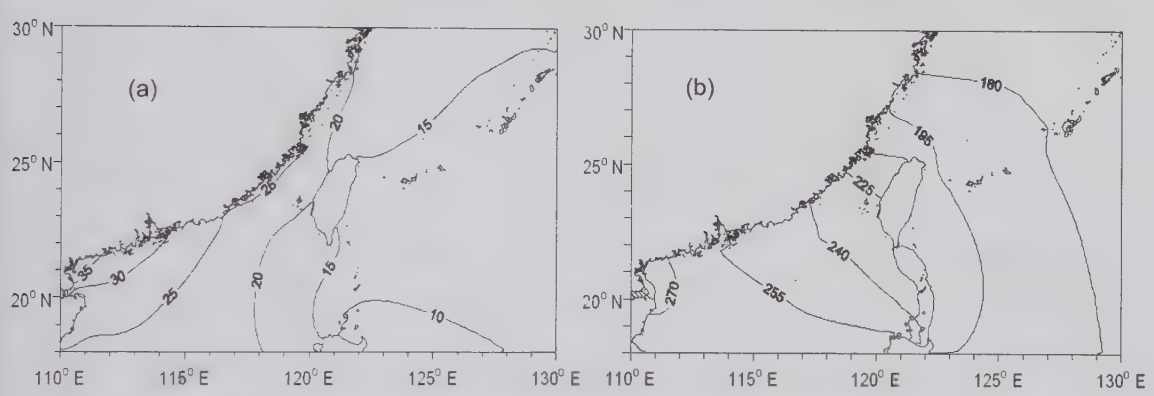

Fig. 6 Co-tidal and co-range charts of O_1 tidal constituent

(a) amplitude (cm); (b) phase (°) referred to 120°E

It can be seen from Fig. 5a that the co-tidal lines of K_1 tidal constituent distribute evenly in the studied area. The amplitude increases gradually from north to south and from east to west. The co-tidal lines are almost parallel to the coastline in the Taiwan Strait, and the amplitude is no less than 30 cm in the western part while it is 20 - 25 cm in the eastern part. The large amplitude area appears between the Qiongzhou Strait and the eastern Leizhou Peninsula, with the maximum amplitude of 45 cm.

The co-range lines of K_1 tidal constituent are about perpendicular to the co-tidal lines in the Taiwan Strait, and distribute densely in the Luzon Strait, with the phase ranging from 225° to 300°. In the Taiwan Strait, the high tide time in the west coast is later than that in the east coast at the same latitude, that is, the high tide time defers slightly from east to west. According to the distribution pattern, the propagating path of K_1 tidal constituent can be deduced: after the tidal wave entering the studied area from the west Pacific, it propagates southwestward through the Taiwan Strait and the Luzon Strait.

As the Fig. 6 shown, the distribution pattern of O_1 tidal constituent is similar to K_1, no matter the

amplitude or the phase. The amplitude of O_1 tidal constituent is 5 cm - 10 cm smaller than that of K_1, and the maximum amplitude (45 cm) appears in the Qiongzhou Strait. The propagating direction is also southwestward, the same as K_1 tidal constituent, so the high tide time defers slightly from east to west too, and the high time appears near the Leizhou Peninsula and the Qiongzhou Strait. But the phase of O_1 tidal constituent is 20° ahead to that of K_1 tidal constituent.

As compared with M_2 and S_2 tidal constituents, the amplitude maximum of K_1 and O_1 tidal constituents appear near the Leizhou Peninsula and the Qiongzhou Strait in stead of the middle Taiwan Strait. Furthermore, the co-tidal and co-range lines of K_1 and O_1 tidal constituents do not distribute densely around the Taiwan Bank, indicating that the diurnal tidal waves directly enter the SCS through the Taiwan Strait and the Luzon Strait. This is due to that the diurnal tidal waves dissipate less energy than the semi-diurnal tidal waves (Ye and Ye, 1986), so it can accumulate enough energy to propagate through the Taiwan Strait from northeast to southwest.

3.4 P_1 and Q_1 tidal constituents

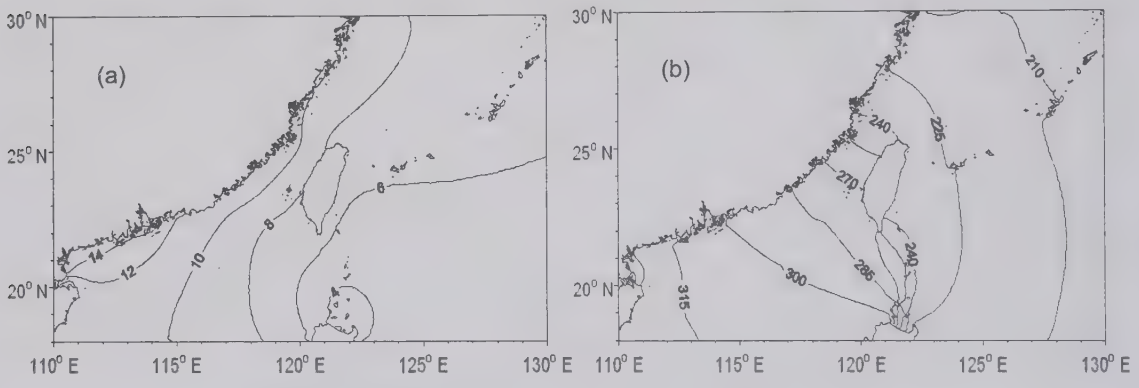

Fig. 7 Co-tidal and co-range charts of P_1 tidal constituent

(a) amplitude (cm); (b) phase (°) referred to 120°E

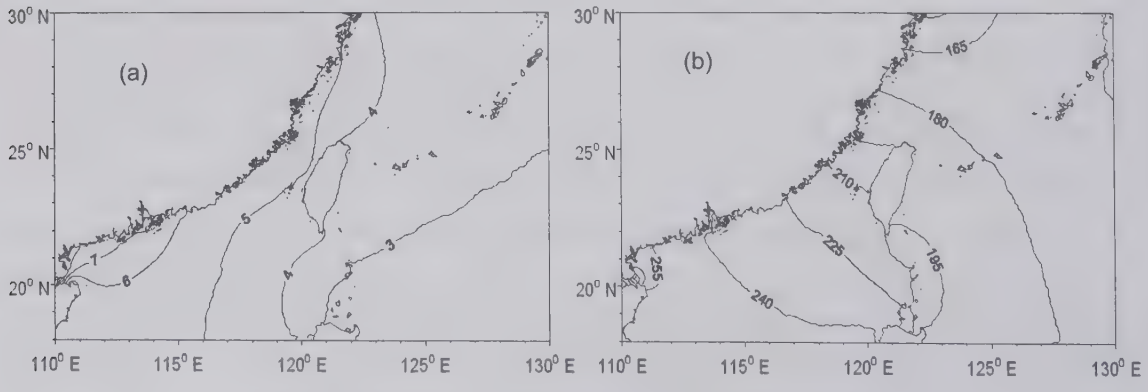

Fig. 8 Co-tidal and co-range charts of Q_1 tidal constituent

(a) amplitude (cm); (b) phase (°) referred to 120°E

As demonstrated in Fig. 7 and Fig. 8, the distribution patterns of co-tidal and co-range of P_1 and Q_1 are quite similar to those of the other major diurnal tidal constituents. The co-tidal lines are perpendicular to the co-range lines, and the phase value increases from northeast to southwest. The maximal amplitudes of P_1 and Q_1 tidal constituents are no more than 15 cm, ranging from 3 cm - 15 cm for P_1 tidal constituent and 3 cm - 8 cm for Q_1 tidal constituent, respectively. The phase of P_1 tidal constituent is close to that of K_1, increasing southwestward from 210° to 330°, while the phase of Q_1 tidal constituent is close to that of O_1, ranging from 170° to 260°. The tidal wave propagates faster in the Luzon Strait, densely in the phase lines there. The maximal amplitude appears almost in the same area, nearshore the eastern Leizhou Peninsula, for both P_1 and Q_1 tidal constituents.

3.5 N_2 and K_2 tidal constituents

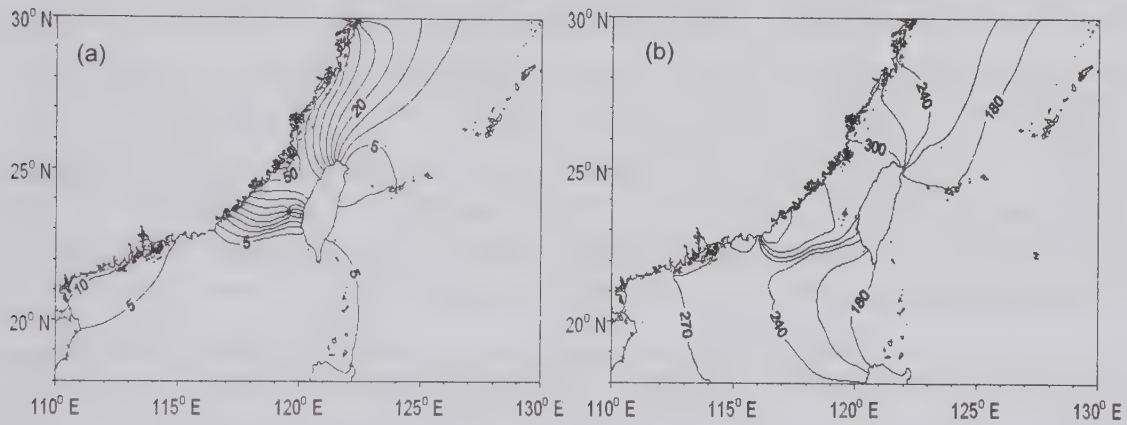

Fig. 9 Co-tidal and co-range charts of N_2 tidal constituent

(a) amplitude (cm); (b) phase (°) referred to 120°E

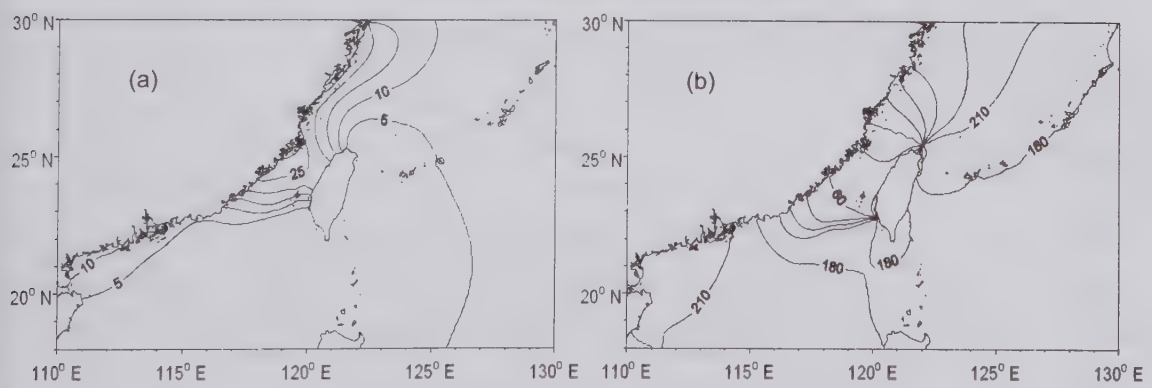

Fig. 10 Co-tidal and co-range charts of K_2 tidal constituent

(a) amplitude (cm); (b) phase (°) referred to 120°E

N_2 and K_2 tidal constituents are similar with M_2 and S_2 tidal constituents, respectively, no matter the amplitude pattern or the phase pattern. The amplitude in the west is larger than that in the east of the strait.

The co-range distribution also shows that a degenerative rotary tidal system exists near the north cape of Taiwan Island. The amplitude increases as the south and north tidal waves converge in the Taiwan Strait. The phase patterns of N_2 and K_2 tidal constituents are almost consistent with those of M_2 and S_2 tidal constituents, respectively.

4 Conclusions

The harmonic constants of 8 principal tidal constituents have been calculated and validated, and the co-tidal features are given in this paper. The main conclusions include:

(a) It is indicated from the comparisons that the model result matches basically with the observation one. The average absolute deviations for amplitude of four tidal constituents, M_2, S_2, K_1 and O_1, are 4.1 cm, 7.4 cm, 2.3 cm and 3.2 cm respectively; and the average absolute deviations for the phase of these tidal constituents are 5.6°, 10.5°, 6.3°and 7.5°, respectively. The average absolute deviations of amplitude for P_1, Q_1, N_2 and K_2 tidal constituents are 1.2 cm, 1.0 cm, 4.5 cm and 5.3 cm, respectively.

(b) In the model domain, the tide propagates from the western Pacific. The semi-diurnal tide consists of two branches, which enter the Taiwan Strait from south and north respectively. The north branch is a degenerative rotary tidal system, and converges with the south branch in the middle of Taiwan Strait. The diurnal tide obviously takes the Kelvin wave form when it propagates through the Taiwan Strait.

(c) The maximal amplitude of the semi-diurnal tides appears around the Meizhou Bay and Xinghua Bay, Fujian Province. The maximum values of M_2 and S_2 are 223 cm and 80cm respectively. The maximal amplitude of the diurnal tides appears near the Qiongzhou Strait and the Leizhou Peninsula, with the maximum amplitude of about 40 cm.

(d) For S_2 tidal constituent, there is an obvious amphidromic point near the Taiwan Bank.

(e) The patterns of co-tidal and co-range charts of N_2, K_2 and P_1, Q_1 are similar to those of M_2, S_2 and K_1, O_1, respectively.

Acknowledgements

This research is jointly supported by the National Natural Science Foundation of China under contract Nos. 40576015, 40810069004 and 40821063, by the key research project of Fujian Province under contract No. 2004N203, and by the Fujian demonstrating region of the “863” Project of the Ministry of Science and Technology of China.

Reference

[1] Cao M D, Fang G H. A numerical model for tides and tidal currents in northern South China Sea [J]. Tropic

Oceanology, 1990, 9(2): 63-70.

[2] Ding W L. The characteristics of the tides and tidal currents in the Taiwan Strait [J]. Journal of Oceanography in Taiwan Strait, 1983, 2(1): 1-8.

[3] Fang G H, Yang J F, Zhao X C. A numerical model for tides and tidal currents in Taiwan Strait [J]. Acta Oceanologica Sinica, 1985, 7(1): 12-21.

[4] Fang G H. Tide and tidal current charts for the marginal seas adjacent to China [J]. C. J. of Oceanology and Limnology, 1986, 4(1): 1-16.

[5] Fang G H, Cao M D, Huang Q Z. A numerical model of tides and tidal currents in South China Sea [J]. Acta Oceanologica Sinica, 1994, 16(4): 1-12.

[6] Fang G H, Wang Y G, Wei Z X, et al. Empirical cotidal charts of the Bohai, Yellow and East China Seas from 10 years of TOPEX/Poseidon altimetry [J]. Journal of Geophysical Research, 2004, 109: 1-13.

[7] Fang G H, Zheng W Z, Chen Z Y, et al. Analysis and forecast of tides and tidal currents. Beijing: Beijing Press, 1986.

[8] Hu J Y, Kawamura H, Hong H S, et al. Tidal features in the china seas and their adjacent sea areas as derived from TOPEX/POSEIDON altimeter data [J]. Chinese Journal of Oceanology and Limnology, 2001, 19(4): 293-305.

[9] Jan S, Wang Y H, Wang D P, et al. Incremental inference of boundary forcing for a three-dimensional tidal model: tides in the Taiwan Strait [J]. Continental Shelf Research, 2004, 24: 337-351.

[10] Jan S, Chen C S, Wang J, et al. The anomalous amplification of M_2 tide in the Taiwan Strait [J]. Geophysical Research Letters, 2004, 31: 1-4.

[11] Lin M C, Juang W J, Tsay T K. Anomalous amplifications of semidiurnal tides along the western coast of Taiwan [J]. Ocean Engineering, 2001, 28: 1 171-1 189.

[12] Liu J F, Liu Z, Gu Y Y, et al. Analysis of the hydrographic elements features in Taiwan Strait [J]. Marine Forecasts, 2002, 19(3): 22-32.

[13] Li Y C, Cai W L, Li L, et al. The tide characteristics of the seas adjacent to Fujian and Taiwan derived from TOPEX/POSEIDON altimeter data [J]. Acta Oceanologica Sinica, 2002, 24(supplement 1): 154-162.

[14] Qian C C, Shen Y.J. Distribution of 9 principal tidal constituents and tide prediction for the East China Sea [J]. China Ocean Engineering, 2000, 14(4): 541-548.

[15] Sha W Y, Lu X G, Jiang G R. Numerical simulation of M_2 tide characteristics in the sea area around Taiwan Strait Island [J]. Journal of PLA University of Science and Technology. 2000, 1(1): 80-87.

[16] Sha W Y, Lu X G, Chen X, et al. Numerical simulation of characteristics of semidiurnal tidal waves in sea region around Taiwan [J]. Acta Oceanologica Sinica, 2001, 23(4): 31-40.

[17] Sha W Y, Lu X G, Zhang W J, et al. Synthetic property of diurnal constituent, tide and tidal current of the sea regions around Taiwan Island [J]. Marine Science, 2002, 26(10): 62-69.

[18] Shen Y J. Numerical computation of tides in the East China Sea [J]. Journal of Shangdong College of Oceanology, 980, 10(3): 26-35.

[19] Wu Z K, Tian J W, Lu X Q, et al. A numerical model of tides in the South China Sea by adjoint method [J]. Oceanologia et limnologia sinica, 2003, 34(1): 101-108.

[20] Wu Z K, Tian J W, Zhao Q. 3-D numerical simulation of the South China Sea tidal waves with assimilation

method [J]. Journal of Hydrodynamics, 2004, 19(4): 501-506.

[21] Wang Z H. Tide application along China coast. 1986.

[22] Yan T Z, Wu Y C. Numerical study on upwelling along Fujian coast I. numerical modeling on tide and tidal current in the Taiwan Strait [J]. Studia Masina Sinica, 1995, 36: 47-53.

[23] Ye A L, Chen Z Y, Yu Y F. Numerical investigation of three-dimensional semi-diurnal tidal waves in Taiwan Strait and its adjacent areas [J]. Oceanologia et Limnologia Sinica, 1985, 16(6): 439-450.

[24] Ye A L, Ye J H. Numerical investigation of three-dimensional diurnal tidal waves in Taiwan Strait and its adjacent areas [J]. Oceanologia et limnologia Sinica, 1986, 17(3): 260-265.

[25] Ye A L. Kelvin wave in Taiwan Strait [J]. Marine Science Bulletin, 1990, 9(5): 1-5.

[26] Yu G M. The basic analysis of the tidal characteristics in the South China Sea [J]. Acta Oceanologica Sinica, 1984, 6(3): 293-300.

[27] Yu Y F, Yu Y X, Zuo J C, et al. Effectof sea level variation on tidal characteristic value for the East China Sea [J]. China Ocean Engineering, 2003, 17(3): 369-382.

[28] Zeng G N, Qi Y Q, Hu J Y, et al. Advances in the M_2 tide wave research in the Taiwan Strait [J]. Advances in Marine Science, 2004, 22(4): 508-518.

[29] Zhao M C, Han X H. The calculation and research for the tidal charts in the China seas [J]. Advances in Water Science, 1995, 1: 23-30.

[30] Zhen W Z, Chen F N, Chen X Z. The tides and tidal currents in the Taiwan Strait [J]. Journal of Oceanography in Taiwan Strait, 1982, 1(2): 1-4.

台湾海峡及其邻近海域潮汐数值计算

朱 佳[1,2]，胡建宇[1,2]，张文舟[2]，曾淦宁[2,3]，陈德文[1]，陈金泉[1]，商少平[1]

（1. 厦门大学海洋学系 亚热带海洋研究所，福建 厦门 361005；2. 厦门大学 近海海洋环境科学国家重点实验室，福建 厦门 361005；3. 浙江工业大学海洋技术专业，杭州 浙江 310014）

摘 要：建立三维潮波模式，模拟了台湾海峡及其邻近海域(18 ～ 30°N，110 ～ 130°E)八个主要分潮(M_2、S_2、K_1、O_1、P_1、Q_1、K_2、N_2)，并利用中国大陆及环台湾岛20多个潮位站的实测资料进行验证，计算结果与实测值吻合良好。此外，给出了八个主要分潮的同潮图，并逐个讨论了潮汐特征。结果显示：(1) 台湾海峡中的潮波运动是北部蜕化了的旋转潮波系统和南部的前进潮波系统共同作用的结果。(2) 半日分潮南、北两支潮波在台湾海峡中部汇合，而全日分潮则在台湾海峡南部海域汇合后继续朝西南方向传播。(3) 半日分潮振幅最高值发生在福建省湄洲湾—兴化湾一带，全日分潮最高值则出现在雷州半岛以东一带近岸海域。(4) N_2、K_2 和 O_1、P_1、Q_1 分潮的振幅、迟角分布分别同 M_2 与 K_1分潮的整体分布趋势相似。

关键词：物理海洋学；台湾海峡及其邻近海域；潮汐特征；数值计算

Effect of Fouling in Daya Bay Scallop *chlamys nobilis* (reeve) Cultivation: Food Competition and Nutrient Release

SU Zhen-xia[1], XIAO Hui[1], HUANG Liang-min, YAN Yan[2]

1. *Huaihai Institute of Technology, Lianyungang* 222005, *Jiangsu Province, China;*

2. *LED, South China Sea Institute of Oceanology, Chinese Academy of Sciences, Guangzhou* 510301, *Guangdong Province, China*

Abstract: Biofouling is an important factor that affects bivalve farming industry. Fouling organisms may reduce growth and survival rate of the cultured species. Fouler are often filter feeders, so they are potential competitors for food resource with the cultured species. The present study was conducted to measure the impact of fouling on food uptake and nutrient release in April, 2006 in Daya Bay near Guangzhou, China. Results showed that fouling organisms had significant effect on food uptake and nutrient release. The chlorophyll a uptake rate of fouled scallops was 7.53 / Lh ± 1.416 / Lh in April, significantly higher than those of cleaned scallops, *i.e.*, 4.23 / Lh ± 2.744 / Lh. The consumption of total particulate matter by fouled scallops in April was 5.52 / Lh ± 0.818 / Lh; the corresponding results for cleaned scallops are 2.49 / Lh ± 0.614 / Lh Fouling increased ammonia release significantly. The ammonia release rate of fouled scallops was 33.81/ Lh ± 7.699 / Lh in April, while cleaned scallops released 2.46 / Lh ± 0.511 / Lh ammonia. Phosphate uptake of fouled scallops was 2.01± 0.699 / Lh and cleaned scallops released phosphate 6.01 / Lh ± 0.876 / Lh in April. There was not significant difference in nitrate consumption between fouled and cleaned scallops. According to the phytoplankton classification of input and output water samples, fouled scallops filtered more phytoplankton species than cleaned scallops. Therefore, this study showed that fouling contributed much to phytoplankton depletion and concentration increase of ammonia in water.

Keywords: scallop; *Chlamys nobilis*; fouling; food uptake; nutrient release

1 Introduction

Most fouling organisms are sedentary filter feeders [1-5] settling on culture -equipment or directly on bivalve shells. For fouling organisms that settle on shells, they not only compete for food but also increase the weight of shells substantially, which may restrict the opening of the valves and affect feeding [6]. Some fouling organisms such as sponges and burrowing worms can even bore through the shell, damaging and weakening the shell, or grow between the shells and prevent the cultured species from closing completely [7-13]. For fouling species growing in nets or cages, the fouling organisms not only compete for food but also greatly reduce or restrict water flow. Consequently, less food is available for individuals and growth is decreased [3, 6,14]. Labor and maintenance costs will thus increase greatly.

Received on June 5, 2008

There were already many reports about the effect of fouling on the cultured bivalves. Mohammad (1976) showed that fouling negatively affected the growth and survival of the related pearl oysters (*Pinctuda ficatu*) [15]. Arakawa (1990) showed the effect of fouling on Pacific oyster (*Crassostrea gigas*) [1]. Claereboudt (1994) reported that regularly changing the pearl nets could increase muscle and soft tissue growth of giant scallops (*Placopecten magellanicus*) [14]. Taylor (1997) reported that fouling affected the growth of pearl oyster, and some fouling even invaded the shell margin, causing shell deformity [3]. Additionally, fouling set more additional weight and dragging on culture equipment and increased the need of buoying and anchoring systems [14]. However, some reports showed that fouler were not important competitors to cultured species and had only a small effect on nutrient use and release. The increase of certain nutrients caused by fouling may stimulate phytoplankton production, thereby increasing the food supply to aquaculture organisms. Thus, fouler may have a positive influence [4] on bivalve farming.

In Daya Bay, scallop culture is constantly submerged and become fouled by ascidians, barnacles, bryozoans, filter-feeding gastropods and bivalves. Lin and Hu (1991) described various fouling species that attached to adult *Chlamys nobilis* [4]. However, the study was concerned with the identification of fouling species rather than determining in detail any effects they might have on *Chlamys nobilis.* The aim of this study was to study the uptake of food and the release of nutrients by scallops and the associated fouler. The experiment was conducted on measuring food uptake and nutrient release in two different study groups (fouled scallop and cleaned scallop) in April 2006

2 Material and methods

2.1 Sample collection and acclimation

In April 2006, scallop cages were collected from Daya Bay culture farm and then transported to the laboratory. Fouled scallops were carefully removed by hand from cages and placed in glass tanks with running water from Daya Bay. Water temperature in tank was 18 °C in April.

All samples were maintained in glass tanks for acclimation (48 h). After acclimation, fouled scallops were transferred to 3-L flow-through containers. Eight containers were used and every container had one-two scallops. Water flow was maintained at about 250 - 300 mL / min. 1 L water samples were taken from the input and output of the containers every hour during a 3-h period. Another 100 mL water samples were taken for phytoplankton species classification in the first sample-taken time. At the end of the experiment, fouler were cleaned from scallop shells and measured dry weight. The cleaned scallops were reacclimated for a short period and then the same experiment as with the fouled scallops was conducted.

2.2 Food uptake and nutrient release rates

Subsamples of 500 mL were taken from each 1-L sample and filtered onto Whatman GF/F 60-mm filters. The filter was put in 90% acetone and frozen for later chlorophyll a analysis. Chlorophyll a was measured using a spectrophotometer (GB 12763.6-1991) [17]. Another 500-mL subsamples were filtered

with pre-dried and pre-weighed Whatman GF/F 60-mm filters for total particulate matter analysis. Filters were later dried at 60 °C for 6 hours and weighed. The filtered water of 500 mL was frozen and ammonia, nitrite, nitrate and phosphate concentrations were later determined using the method described in GB 12 763.4 - 1991 [18].

Food uptake rate and nutrient release rate were calculated by subtracting the output concentration from the input concentration, dividing by the input concentration, and then multiplying by the water flow as was described by Leblanc [4].

Thus the food uptake rate was calculated according to the formula

$$C = V(C_1-C_2) / C_1$$

where C=food uptake rate / Lh; V = water flow rate / Lh; C_1 = inflow concentration of chlorophyll a or TPM; C_2 = outflow concentration of chlorophyll a or TPM. Nutrient release rate was calculated according to the formula

$$R = V(C_1-C_2) / C_1$$

where R=nutrient release rate / Lh, V = water flow rate / Lh; C_1 = inflow concentration of NH_4-N, NO_3-N, NO_2-N and PO_4-P; C_2 = outflow concentration of NH_4-N, NO_3-N, NO_2-N and PO_4-P.

Phytoplankton feeding percentage was calculated by subtracting the output phytoplankton density from the input phytoplankton density then dividing by the input phytoplankton density.

2.3 Statistical Analysis

One factor ANOVA was used to compare the differences by fouled and cleaned scallop treatments in food uptake and nutrient release rate. Significance of all tests was accepted at $P < 0.05$.

3 Results

The shell length, shell height, shell width, total dry weight of scallop and total dry weight of fouling, percentage of fouling are shown in Tab. 1. Fouling community weight was high compared to scallop weight as indicated by the percentages 42.65% ± 31.06% for April. The fouling community was mainly constituted of ascidians, barnacles, oysters and other minor fouling species.

Tab. 1 Biological data of experimental organisms

Shell length / cm	Shell height / cm	Shell width / cm	dry weight of scallop / g	dry weight of fouling / g	percentage of fouling/scallop / %
7 08 ± 0 21	7.22 ± 0 21	2 48 ± 0 20	28.24 ± 2 34	12 06 ± 9 03	42.65 ± 31.06

In April, the fouled and cleaned scallops had significant differences in chlorophyll a and total particulate matter uptake ($P < 0.001$) (Tab. 2), and in ammonia ($P < 0.001$) and nitrite release ($P < 0.001$) (Tab. 3). The presence of fouling significantly increased food uptake and ammonia and nitrite releases.

There was no significant difference in nitrate uptake ($P > 0.05$) (Tab. 4). The fouled scallops uptook phosphate, while cleaned scallops released phosphate (Tab. 4).

Tab. 2 Total particulate matter and chlorophyll a uptake rates by fouled and cleaned scallops in April 2006

	April 2006	
	TPM / Lh	Chl. α / Lh
Fouled scallop	5.52 ± 0.818	7.53 ± 1.416
Cleaned scallop	2.49 ± 0.614	4.23 ± 2.744

Tab. 3 Ammonia and Nitrite release rates by fouled and cleaned scallops in April 2006

	April 2006	
	NH_4-N / Lh	NO_2-N / Lh
Fouled scallop	33.81 ± 7.699	3.33 ± 0.538
Cleaned scallop	2.46 ± 0.511	0.19 ± 0.061

Tab. 4 Phosphate and Nitrate uptake rates by fouled and cleaned scallops in April 2006

	April 2006	
	PO_4-P / Lh	NO_3-N / Lh
Fouled scallop	2.01 ± 0.699	2.99 ± 1.337
Cleaned scallop	-6.01 ± 0.876	2.71 ± 1.235

Tab. 5 Classification of phytoplankton from input water in April 2006

Bacillariophyta	*Pleurosigma falx*
Amphora arenaria	*Pleurosigma* sp.
Amphora sp.	*Pseudonitzschia delicatissima*
Actinoptychus undulatus	*Pseudonitzschia pungens*
Asteromphalus cleveanus	*Rhizosolenia alato f. genuina*
Biddulphia ahombus	*Rhizosolenia alato f. gracillima*
Cerataulina daemon	*Rhizosolenia alato f. indica*
Cerataulina pelagica	*Rhizosolenia cochlea*
Chaetoceros affinis v.affinis	*Rhizosolenia imbricata f. imbricata*
Chaetoceros cinctus	*Rhizosolenia imbricata v.schrabsolei*
Chaetoceros compressus	*Rhizosolenia sinensis*
Chaetoceros debilis	*Rhizosolenia styliformis v.styliformis*
Chaetoceros denticulatus f. denticulatus	*Skeletonema costatum*
Chaetoceros lorenzianus	*Thalassionema nitzschoides*
Cocconeis scutellum v .parva	*Thalassiothrix lorgissima*
Coscinodiscus sp.	*Thalassiosira subtilis*
Cyclotells striata v. striata	**Pyrrophyta**
Cyclotells stylbrum	*Ceratium furca*
Cylindrotheca closterium	*Gonyaulax* sp.
Diploneis sp.	*Gonyaulax verior*
Gomphonema kasnakowi	*Gymnodinium sanguineum*
Guinardia flaccida	*Gyrodinium instriatum*
Gyrosigma balticum	*Noctiluca scintillans*
Gyrosigma wormleyi	*Prorocentrum lima*
Leptocylindrus danicus	*Prorocentrum Micans*
Licmophora ehrenbergii	*Prorocentrum Mexicanum*
Melosira juergensi	*Prorocentrum* sp.
Navicula directa	*Scrippsiella trochoidea*
Navicula sp.	**Chrysophyta**
Nitzschia frustulum	*Distephanus speculum*
Nitzschia longissima	**Cyanophyta**
Nitzschia sp.	*Trichodesmium erythraeum*

Tab. 6 Feeding percentage of fouled scallops to the following genus of bacillariophyta

Genus	Feeding percentage / %
Cerataulina	100 ± 0
Chaetoceros	22.67 ± 10.67
Cyclotella	22.22 ± 19.25
Guinardia	100.00 ± 0.00
Leptocylindrus	100 ± 0
Melosira	83.33 ± 8.33
Navicula	36.67 ± 20.82
Nitzschia	15.69 ± 5.88
Pleurosigma	61.90 ± 8.25
Pseudonitzschia	34.98 ± 6.66
Rhizosolenia	62.09 ± 2.48
Skeletonema	91.67 ± 3.61
Thalassionema	33.33 ± 8.25
Thalassiosira	80.56 ± 12.93
Thalassiothrix	71.43 ± 14.29

The phytoplankton species in water were shown in Tab. 5. The phytoplankton feeding percentage of fouled and cleaned scallops were shown in Tab. 6, Tab. 7, and Tab. 8. Fouled scallops filtered more phytoplankton species than cleaned scallops. The common phytoplankton that fouled and cleaned scallops filtered had eight genus, which were *chaetoceros*, *navicula, cyclotella*, *nitzschia*, *thalassiosira*, *pseudonitzschia*, *thalassionema*, *rhizosolenia*. The presence of fouling increased phytoplankton consumption and the phytoplankton in water was fully filtered by the fouled scallops than the cleaned scallops.

Tab. 7 The Feeding percentage of cleaned scallops to the following genus of bacillariophyta

Genus	Feeding percentage / %
Chaetoceros	16.67 ± 7.64
Cyclotella	66.67 ± 4.12
Diploneis	66.67±28.86
Gyrosigma	50.00 ± 10.00
Navicula	37.5±12.5
Nitzschia	50.41 ± 18.27
Pseudonitzschia	48.16 ± 5.09
Rhizosolenia	15.04 ± 6.72
Thalassionema	26.39 ± 12.73
Thalassiosira	72.22 ± 9.62

Tab. 8 Feeding percentage of fouled and cleaned scallops to other phylum phytoplankton

	Feeding percentage / %	
Phylum	Fouled scallop	Cleared scallop
Pyrrophyta	48.15 ± 6.42	20.11 ± 3.59
Chrysophyta	60.42 ± 3.61	56.67 ± 5.77
Cyanophyta	100.00 ± 0.00	66.67 ± 28.87

4 Discussion

Daya Bay belongs to subtropical sea area. Fouling organisms settle all year around and the first

peak fouling period is from May to August, and the second from October to November. Fouler closely-related to scallop growth mainly include oyster, ascidian, barnacle, et al. Oyster and ascidian have long growth period and the period from April to June is the prosperous fouling period. In November, they are also found settled on cages firmly and are difficult to remove. Barnacle has smaller body size and settles in the whole year. Its peak fouling period is from May to August [19, 20].

In our study, fouling community weight was 42.65% ± 31.06% of the dry weight of the scallop in April. Ascidians, barnacles and oysters were the main fouling species. There were also other species, such as polychaetes and bryozoans, but their biomass was minor compared to the main fouling species. The ascidians, barnacles and oysters are filter-feeding animals, so the uptake of food of fouled scallops was greater than that of cleaned scallops. When many filter-feeding animals gathered on the scallop shells, the weight of shells was increased and the opening of the valves was restricted. These fouler not only influenced the feeding of shellfish but competed for food, especially when food was not abundant. The ammonia release of fouled scallops was also increased, which was 13 times more than that of cleaned scallops.

Lesser (1992) in his experiment reported that on mussel rope culture, blue mussels selected small phytoplankton, whereas the ascidians and the suspension-feeding gastropods preferred large phytoplankton. When food is not limited, interspecific competition for food do not significantly limit mussels yield [2]. In the study, the present of foulings fully utilized the phytoplankton in water. The feeding species of fouled scallops was obviously more than cleared scallops. At the same time, the feeding percentage of fouled scallops to several species was greater than that of cleaned scallops. That is, the interspecific competition for food existed. If the suspension-feeding fouling on scallop shells was more, the food competition certainly affected scallop growth.

The quantity and biomass of fouler that settled on culture cages were very large. Ascidians and barnacles, as the main fouling species, settled intensively on farming cages. The barnacles, settled on not only the scallops shell but the shell of other fouling animals. Their presence may have impact on the whole farming area. When the culture density is high and oxygen supply is scarce, the fouler setting on scallop shells or on cages may compete for food and oxygen with the cultured organisms. As a result, the growth and survival rates of cultured animals will be reduced, which may affect the aquaculture industry.

Results of this study showed that the fouler settling on scallop shells is one of the important affecting factors. Their presence increased food uptake, ammonia, nitrite release. The cages and scallop shells should be cleaned at certain time intervals. The type and abundance of fouling organisms on scallop shells and cages vary temporally. In different months, when the fouling community is different, the impact of fouling organisms on scallops may be different. In the Daya Bay, a subtropical farming area, filter-feeding fouler are dominant, so the impact of fouling organisms should be taken into account when considering the carrying capacity of scallop culture system.

Acknowledgements

This work was supported by National Science Foundation of Huaihai Institute of Technology (No. KQ07102) and Open Project Program of the Key Laboratory of Marine Bio-resources Sustainable Utilization, SCSIO, CAS (No. KK09001). The authors thank the staff of MBRS of the Chinese Academy of Sciences for their technical support. Special thanks to anonymous referees for their constructive comments on this manuscript.

References

[1] Arawaka K Y. Competitors and fouling organisms in the hanging culture of the pacific oyster, Crassostrea gigas (Thunberg) [J]. Mar. Behav. Physiol, 1990, 17 (2): 67-94.

[2] Lesser M P, Shumway S E, Cucci T, et al. Impact of fouling organisms on mussel rope culture: interspecific competition for food among suspension feeding invertebrates [J]. J. Exp. Mar. Biol. Ecol., 1992, 165 (1): 91-102.

[3] Taylor J J, Southgate P C, Rose R A. Fouling animals and their effect on the growth of silver-lip pearl oysters, *Pinctada maxima* (Jameson) in suspended culture [J]. Aquaculture, 1997, 153: 3l-40.

[4] LeBlanc A R, Landry T, Miron G. Fouling organisms of the blue mussel *Mytilus edulis*: their effect on nutrient uptake and release [J]. J. Shellfish Res., 2003, 22(3): 633 - 638.

[5] Ross K A, Thorpe J P, Brand A R. Biological control of fouling in suspended scallop cultivation [J]. Aquaculture, 2004, 229: 99 - 116.

[6] Lodeiros C J M, Himmelman J H. Influence of fouling on the growth and survival of the tropical scallop, *Euvola* (Pencten) *ziczac* (L. 1758) in suspended culture [J]. Aquacult. Res., 1996, 27 (10): 749-756.

[7]Blake J M, Evans J W. Polydora and other related genera as borers in mollusc shells and other calcerous substrates [J]. Veliger, 1972, 15: 235-249.

[8] Bergman K M, Elner R W, Risk M J. The influence of *Polydora websteri* borings on the strength of the shell of the sea scallop *Placopecten magelllanicus* [J]. Can. J. Zool, 1982, 60: 2 551 - 2 556.

[9] Baxter J M. The incidence of *Polydora ciliata* and *Cliona celata* boring the shell of *Patella vulgata* in Orknay [J]. J. Mar. Biol. Assoc. UK, 1984, 64: 728 - 729.

[10] Beristain M A, Malouf R E. The effect of epibionts on the growth of *Mytilus edulis* cultured in Long Island Sound [J]. J. Shellfish Res., 1988, 7: 149.

[11] Schleyer M H. Shell-borers in the oyster, *Striostrea magaritacea*: pest or symbionts [J]? Symbiosis, 1991, 10: 135-144.

[12] Wargo R N, Ford S E. The effect of shell infestation by *Polydora* sp. and infection by *Haplosporidium nelsoni* (MSX) on the tissue condition oysters *Crassostrea gigas* [J]. Estuaries, 1993, 16: 229-234.

[13] Caceres-Martinez J, De Oca P M M, Vasquez-Yeomans R. *Polydora* sp. infestation and health of the Pacific Oyster *Crassostrea gigas* cultured in Baja California, NW Mexico [J]. J. Shellfish Res. 1998, 17 (1): 259-264.

[14] Claereboudt M R, Bureau D, Cŏté J, et al. Fouling development and its effect on the growth of juvenile giant scallops (*Placopecten magellanicus*) in suspended culture [J]. Aquaculture, 1994, 121: 327-342.

[15] Mohammad M B M. Relationship between biofouling and growth of the pearl oyster, *Pinctada fucafu* (Gould) in Kuwait, Arabian Gulf [J]. Hydrobiologica, 1976, 51: 129-138.

[16] Lin Y G, Hu J X. The effect of fouling on growth and survival of scallop *chlamys nobilis* (reeve) [M]. Res. Expl. Nanhai, 1991, 3: 6-12.

[17] GB 12763.6-1991. The Specification for Oceanographic Survey Observations of Marine Biological Survey [M]. Beijing: Chinese Standard Publications, 1991, 5-6.

[18] GB 12763.4-1991. The Specification for Oceanographic Survey Observations of Chemical Parameters in Sea Water [M]. Beijing: Chinese Standard Publications, 1991, 13-20.

[19] Zheng D Q, Huang Z G. Fouling organisms on mariculture cages in Daya Bay, China [J]. J. Fish. Chin., 1990, 14(1): 15-24

[20] Zheng C X, Huang Z G, li C Y, et al. Fouling organisms on mariculture farming in DAYA Bay, China [J]. Chin. J. Appl. Ecol., 1991, 2(2): 146-152.

污损生物对大亚湾养殖扇贝的食物吸收及营养盐排泄的影响

苏振霞[1]，肖 辉[1]，黄良民[2]，严 岩[2]

（1. 淮海工学院，江苏 连云港 222005；2. 中国科学院南海海洋研究所 热带海洋环境动力学重点实验室，广东 广州 510301）

摘 要：污损生物是影响贝类养殖业生产效率的重要因素。附着在养殖生物贝壳上的污损生物影响养殖生物的生长和存活。大部分污损生物是滤食性捕食者，这些污损生物附着在养殖生物贝壳上竞争食物与空间导致贝类生长速度减慢。本实验主要研究有污损生物附着的扇贝及没有污损附着的扇贝在摄食及排泄上的差异，用以说明污损生物对养殖生物摄食及排泄的影响。本研究对 chlorophyll a 和 TPM 的吸收速率进行了测定，对 NH_4-N，NO_2-N，NO_3-N，PO_4-P 的排泄速率进行了测定，对摄食的浮游植物进行了种类鉴定。研究结果表明，有污损生物附着的扇贝及没有污损附着的扇贝在对浮游植物及颗粒物的吸收速率上存在明显差异($P < 0.001$)。在氨及亚硝态氮排泄速率上也存在明显差异($P < 0.001$)。两者吸收 NO_3-N，且吸收速率无差异。通过对摄食的浮游植物种类的鉴定表明，有污损生物附着的扇贝摄食的浮游植物种类要高于没有污损附着的扇贝，且摄食种类有重叠。对同一类的某些浮游植物，有污损生物附着的扇贝的摄食要高于干净扇贝。本研究结果表明，污损生物对浮游植物的摄食及水中氨氮浓度的提高贡献很大，与养殖生物之间存在食物竞争。

关键词：扇贝；华贵栉孔扇贝；污损生物；食物吸收；营养盐释放

Distribution of Turbidity and Fluorescence of SPM in Adjacent Waters of Taiwan Bank in Summer

HU Yi [1, 2], CHEN Jian [2], HE Zhuan[2]

1.*College of Geosciences, Ocean University of China, Qingdao* 266100, *Shandong Province, China;*

2.*Third Institute of 0ceanography, SOA, Xiamen* 361005,*Fujian Province, China*

Abstract: The turbidity and fluorescence of suspended particulate matter (SPM) in the Taiwan Bank and adjacent waters were investigated during July-August, 2004, to examine the effects of the marine sediments re-suspension and sedimentary processes on the turbidity and fluorescence distribution of SPM. The results show that the turbidity of SPM is affected by the re-suspension of marine sediment in the near shore and continental shelf outer fringe, but not obvious in the shoal. The enrichment of phytoplankton has some effects on the turbidity in the continental shelf outer fringe, but not evident in the near shore. This is helpful for better understanding the distribution of turbidity and fluorescence in the adjacent waters of Taiwan Bank.

Keywords: Taiwan Bank; suspended Matter; turbidity; fluorescence

Marine suspended particulate matter (SPM) has important effects on matter transportation and cycling, and therefore, it belongs to hot research within land-ocean interactions. The studies related to SPM in china focus on the distribution, composition, origin and transport [1-9] and the study areas include the East China Sea, Yellow Sea and Bohai Sea, together with the Changjiang and Pearl River Estuaries[10-13]. Based on multi-disciplined observations in the adjacent waters of Taiwan Bank, Hong (1991) found that there was a special ecosystem structure and distribution in the area [14], which is a famous upwelling area in China, Zhang (2000, 2001) reported the vertical distribution of fluorescence chlorophyll a (chl-a) in the Taiwan Strait, and the temporal variations of fluorescence chl-a over days in the southern of Taiwan Strait [15, 16]. The turbidity and fluorescence is one of the important characteristics of SPM, and is helpful for studying the marine sediment and re-suspension processes and related ecosystem in the adjacent waters of Taiwan Bank. The main objective of this paper is to examine the effects of the marine sediments re-suspension and sedimentary processes on the turbidity and fluorescence distribution of SPM through analyzing the in situ turbidity and fluorescence data of SPM investigated in summer, 2004.

1 Study area and method

Water temperature, salinity, and depth, together with the turbidity and fluorescence of SPM, had been obtained during 25 July to 10 August in 2004 by the SD204, which is a small

Received on March 25, 2008

depth-temperature-salinity exploring instrument, carrying the turbidity and fluorescence sensors, made by Seapoint Company. The range of turbidity and fluorescence was set 0 - 12.5 FTU and 0 - 7.5 μg/dm^3 respectively, sampling frequency 1 time/s, descending speed less than 1 m/s. When water depth is over 200 m, the instruments were only lowered to 200 m. The original data were transformed into ASCII data through the software provided by the instrument, and the spike points had been manually smoothed. The vessel, used in this investigation, is "YanPing Ⅱ", which is owned by Fujian Institute of Oceanography.

Nine stations within two sections were selected to investigate about the turbidity and fluorescence of suspended particulate matter in the Taiwan Bank adjacent waters (Fig. 1). The directions of the two sections are vertical to the coast. Section A generally gets across the Taiwan Bank, and Section B is located at the southwest of Taiwan Bank. It is known to all that the Taiwan Bank is a piece of underwater dune, within 20 m - 30 m water depth, overlying southern part of Taiwan Strait. The depth is generally 40 m on both the northern and western parts of the Taiwan Bank. The southern and east southern parts are the steep continent slope, and the eastern part is Penghu Channel with a water depth over 100 m. The water masses affecting the study area, include the along shore current from China mainland, the water from South China Sea, and the Kuroshio part to the South China Sea through Bashi Channel, and the upwelling water [17].

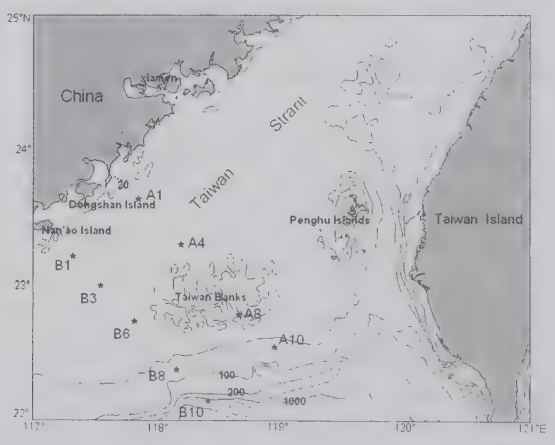

Fig. 1 Location of the survey stations

2 Vertical distributions of turbidity and fluorescence

The vertical distribution of turbidity is shown in Fig. 2 and Fig. 3, and the fluorescence in Fig. 4 and Fig. 5. In order to compare with section A, the data at station B10 was only used shallower than 80 m. According to spatial variations of the topography, the study area is divided into three areas, near shore area, bank area and shelf edge area, respectively. The turbidity and fluorescence show an obvious difference in different areas. Their vertical distributions were classified into four types, strong spring layer, homogeneous, increasing and single peak. The vertical distributions of turbidity and fluorescence in different areas are summarized as the following.

2.1 Near shore area

This area, less than 50 m, is located in the west of the Taiwan Bank, and its SPM is significantly influenced by terrestrial matter. The stations of A1 and B1 are located in this area. Turbidity data become increasing with the depth, and have a spring layer at 10 m. The turbidity data varies from 0.3 FTU to 0.6 FTU at A1 station, and 0.1 FTU to 0.7 FTU at B1 station. Besides, an increasing tendency of turbidity appears toward the seabed, especially at B1 station.

The fluorescence data varies from 0.2 μg/dm^3 at surface to 1.0 μg/dm^3 at subsurface at B1 station, and its spring level reaches 0.1μg/m.dm^3, but the vertical fluorescence at A1 station shows a relatively smooth trend.

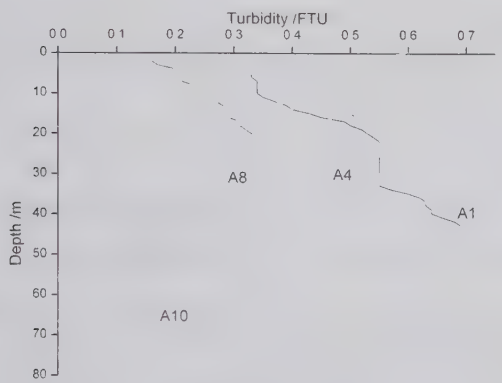

Fig. 2 Vertical distribution of turbidity along section A

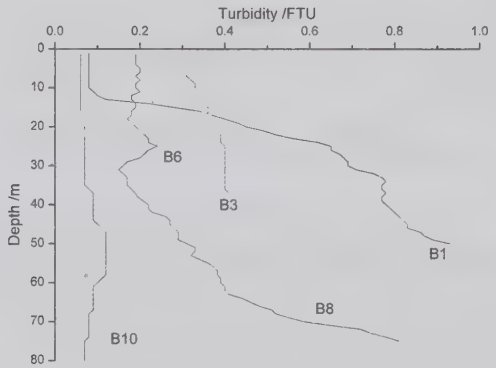

Fig. 3 Vertical distribution of turbidity along section B

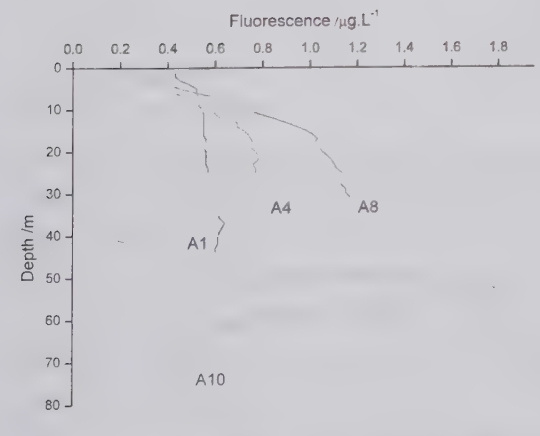

Fig. 4 Vertical distribution of fluorescence along section A

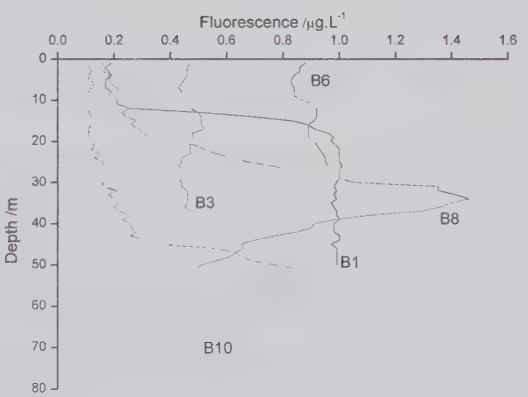

Fig. 5 Vertical distribution of fluorescence along section B

2.2 Bank area

The stations within this area include A4, A8, B3 and B6.The turbidity and fluorescence at A4 station have a strong spring at the depth of 3 - 10 m, and the fluorescence at the subsurface does reach 0.8 μg/dm^3, much higher than 0.3 μg/dm^3 at the surface; under the spring layer, it becomes smooth.

A8 Station is located in the eastern part of Taiwan Bank. The turbidity and fluorescence is relatively stable above 3 m at the surface layer, and then fluorescence varies from 0.3 μg/dm^3 at surface to 1.2 μg/dm^3 near the seabed. The large value of fluorescence shows phytoplankton's flourishing. The turbidity has the same tendency as the fluorescence, but its value is not very high, generally about 0.1 - 0.4 FTU in the whole water column.

The vertical distributions of turbidity and fluorescence at B6 station located in the Taiwan Bank are very smooth due to fully mixed processes by strong hydrodynamics; this trend is similar to that of the B3 station.

2.3 Shelf edge area

The eastern part of Taiwan Bank is the joint area of shelf and slope, with a large gradient of water depth. The stations within this area include B8, A10 and B10. The vertical distribution of fluorescence and turbidity in this area is quite different compared to those in the western part of Taiwan Bank. The turbidity value becomes smaller compared to those in the western part, and the trend of vertical distribution of fluorescence belongs to single peak type. The peak value at B8 station appears at 20 m - 50m, and its maximum value can reach 1.5 μg/dm^3. This suggests that the phytoplankton are enriched in this layer. The trend of vertical distribution of fluorescence at A10 station is generally the same as that at B8 station, except for its peak value at 40 m - 70 m, and so is B10 station, whose peak value is at 45 m - 75 m with a maximum value of 0.9 μg/dm^3. The turbidities at stations of B8 and A10 show a weak peak in accordance with the fluorescence peak, increasing toward the seabed, while relatively stable at station B10.

3 Profiles of turbidity and fluorescence

Profile A is not provided here, considering the stations of A4 and A8 are far away and there are no data on the bank. Fig. 6 and Fig. 7 are turbidity and fluorescence of profile B respectively. The profile B only shows the above 80 m. Turbidity becomes decreasing in the direction from west to east, and the value at bottom is higher than that at upper layer. Turbidity has a great spring layer near the western part of the profile, and the isolines are dense near 10 m waters at B1 station. The vertical mixing was enhanced near B6 station (Taiwan Bank), and therefore, the turbidity tended to be uniform vertically. Moving east along the profile, turbidity value at bottom is higher than those at upper layer in shelf edge. Fluorescence has the same feature as turbidity at western part of Taiwan Bank, but it is different in the eastern part of Taiwan Bank, with a peak value shaped as "bubble" appearing in the middle water.

4 Discussion

SPM has different features in different areas due to many different factors, such as hydrodynamic, submarine geomorphology, material source and the physics and chemistry properties of sediment. The SPM is discussed in the following parts with data of temperature and salinity collected at the same time.

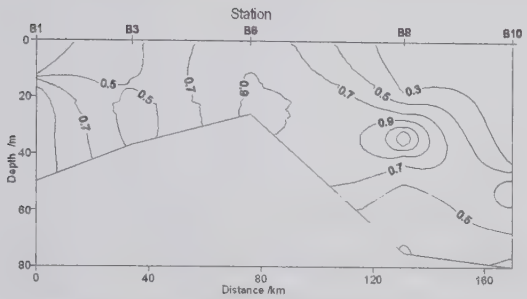

Fig. 6 Fluorescence distribution of profile B

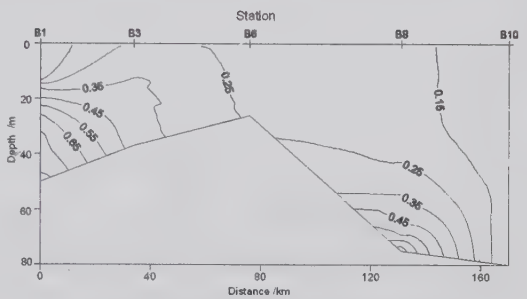

Fig. 7 Turbidity distribution of profile B

4.1 Near shore area

The SPM at B1 station is influenced by the diluted alongshore water in summer. When the diluted water encounters with the seawater, it will overlap on the sea water due to the relatively smaller density, resulting in the halocline and thermocline. Near the border of diluted water and seawater, there exists density stratification, great SPM gradient, and this steady structure limits the exchange of suspended matter. The turbidity value changes from 0.1 FTU at surface layer to 0.6 FTU at subsurface layer, and similarly, the fluorescence value changes from 0.2 μg/ dm^3 to 1.0 μg/dm^3, with changes of temperature and salinity.

According to the study by Zheng (1990) on Yellow Sea [18], the existing turbulent boundary layer near thermocline and halocline causes the water steady and conservative, restricting the advection of ocean current and tidal current. This suggests that the SPM dispersal is also restricted in this area, because the current is the primary carrier and dynamic source of SPM, especially upward movement. The dissolved matter has the potential chances of moving upward due to the hydrodynamics before it deposits on the seabed. When the moving SPM can't break the restriction of spring layer, the SPM will be limited to the waters under the spring layer. In this context, this spring layer likes a "valve", only allowing the suspended matter in, and not out. The SPM enriches near the seabed and forms the "suspended matter spring layer". And this spring layer will change with thermocline and halocline. The phenomena of upwelling is often seen in this area in summer according to previous literatures [19-22]. With a favorable condition of full light and abundant nutrients, phytoplankton can grow rapidly, resulting in suddenly increasing of the fluorescence. The resuspended matter near bottom and lowering settling velocity may be the main factors affecting the phytoplankton assembling, which cause turbidity value becoming large. And the increasing turbidity near the bottom may be the result of resuspended matter near seabed by the strong

hydrodynamics.

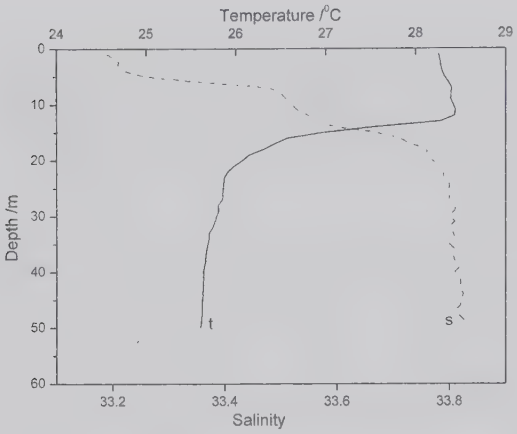

Fig. 8 Temperature and salinity vertical distribution of station B1

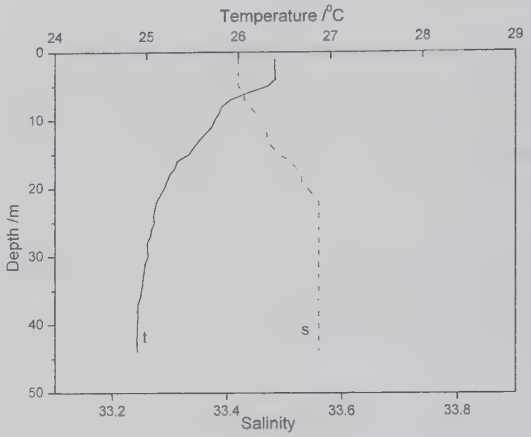

Fig. 9 Temperature and salinity vertical distribution of station A1

Vertical distribution of fluorescence at station A1 does not vary significantly, which may suggest that the resuspension on the seabed is caused by upwelling. The exchange and transport of suspended particulate matter by means of suspension, deposition, resuspension and redeposition near bottom, and therefore, the turbidity often shows a high value correspondingly during the processes. It is expected that the inorganic particulate matter has an important contribution to the high turbidity rather than phytoplankton.

From above analysis, it can be determined that the high turbidity near bottom is mainly due to the resuspension from the seabed rather than the phytoplankton enrichment.

4.2 Bank area

A thin "suspended matter spring layer" is found at the subsurface layer of A4 station in summer (Fig. 10). The surface water is irradiated by sunshine in summer, which causes the surface water temperature higher than that of subsurface, and at the same time, the water below the subsurface layer is mixed to be almost homogeneous by upwelling. Under this condition, a thin thermocline at subsurface is easy to be formed (Fig.10). The phytoplankton would enrich under favorable conditions of temperature and nutrition at subsurface, while this would not easily happen under high temperature at surface. Obviously, the vertical distribution of turbidity and fluorescence at station A4 are influenced by high radiation of sunshine, which are different from those at stations of A1 and B1 near shore area due to interactions between various water masses.

The vertical distributions of turbidity and fluorescence are almost homogeneous at stations of B3 and B6, which is probably due to the full mixing by strong hydrodynamics, and furthermore the coarse sediment is uneasily to resuspend from the bottom.

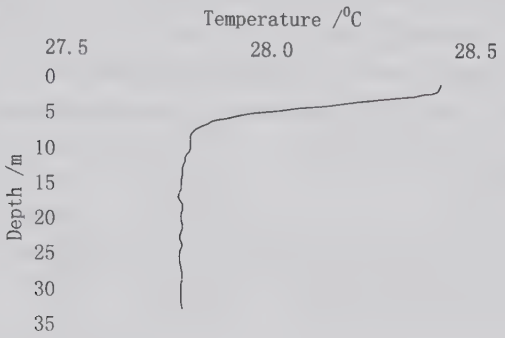

Fig. 10 Temperature vertical distribution of station A4

The fluorescence at Station A8, located at the edge of Taiwan Bank, increases with the depth. This may be due to the joint interactions between upwelling and strong hydrodynamics in the Taiwan Bank. The turbidity has the same tendency as the fluorescence, although not evident as the latter. The increasing turbidity near the seabed may be partly correlated with the enriched phytoplankton.

The vertical trends of turbidity and fluorescence have various features due to the complex hydrodynamics in Taiwan Bank area. The fluorescence increases with the increasing depth at stations of A4 and A8 unlike those at stations of B3 and B6. The vertical turbidity does not vary significantly in this area except for that at station A8, which has an increasing tendency with depth increasing.

4.3 Shelf edge area

A weak peak of the turbidity exists along a peak of the fluorescence at stations of B8 and A10, and it may suggest that the phytoplankton has some influences on the distribution of turbidity. The turbidity below the spring layer increases with the depth, and it is high compared to those above the spring layer. It may be the result of particulate resuspension from the seafloor. This area is far away from mainland, and is little affected by the terrigenous river. The high transparence of sea water in this area is beneficial for phytoplankton growing. Under favorable conditions of temperature, salinity and pressure, fluorescence reaches the peak in the middle of water body.But the assembling is restricted by sunlight and nutrient, and phytoplankton only enriches at certain water layer, where always show the thermocline and halocline. The turbidity is lower in shelf edge area than those near shore area.

5 Conclusion

(1) The survey area is divided into three parts based on Taiwan Bank, near shore area, bank area and shelf edge area respectively. The turbidity is higher at surface than those at bottom in near shore area, with a clear stratification. And the vertical turbidity is mixed to be homogeneous due to the strong hydrodynamics near Taiwan Bank. From eastern direction to the shelf edge area, the turbidity value is lowest, indicating the high transparent.

(2) Fluorescence has the same tendency as the turbidity. Fluorescence shows an obvious stratification in near shore area, higher value near bottom and lower value at surface, which are related to the upwelling in summer near shore. Fluorescence appears homogeneous due to full mixing by strong hydrodynamics in the Taiwan Bank area, and it exists a single peak in shelf edge area.

(3) The distribution of turbidity in near shore area is controlled by the particulate resuspension from bottom, however, it is not obvious in the Taiwan Bank which shows coarse sediment on the seabed. The resuspension effect can cause high turbidity near bottom in the shelf edge, and the weak peak of turbidity at middle layer may be caused by the phytoplankton enrichment.

Acknowledgements

Xiamen University offers the surveying chance, with the finance of Chinese National Natural Science Important Foundation-"Evidence of phytoplankton response to the inter-annual environmental variability in southern Taiwan Strait upwelling"; senior engineer Huang Cai-bin and the sailor on the "Yanping II" provide great help on the survey, and the editor and reviewer give a proper advice to this paper; I am grateful for all suggestions and advice. This research was supported by the SOA Science Fund for Youths of China (2008316) and Fujian Provincial Natural Science Foundation of China (2006J0288).

References

[1] Huan F, Cochranb J K, Hirschberg D J. Transport and sources of metal contaminants over the course of tidal cycle in the turbidity maximum zone of the Hudson River estuary [J]. Water Research, 2002, 36: 733 - 743

[2] Wynn R B, Masson D G, Stow DAV, et al. Turbidity current sediment waves on the submarine slopes of the western Canary Islands [J]. Marine Geology, 2000, 163(1): 185 - 198

[3] Odate T, Hirawake T, Kudoh S, et al. Temporal and spatial patterns in the surface-water biomass of phytoplankton in the North Water [J]. Deep-Sea Research Part II, 2002, 49(22): 4 947 - 4 958

[4] Uncles R J, Bloomer N J, Frickers P E, et al. Seasonal variability of salinity, temperature, turbidity and suspended chlorophyll in the Tweed Estuary [J].The Science of the Total Environment, 2000, 251: 115 - 124

[5] Yang Z S, Guo Z G, Wang Z X, et al. Suspended matter in the Huanghai Sea and East China Sea: its contents, distribution, relation to the water masses and factors of influence [J]. Journal of Ocean University of Qingdao, 1991, 21(3):55 - 69.

[6] Qin Y S, Zheng T M. Preliminary study on sediment distribution in the Inner Shelf of the East China Sea. Geology of the Yellow Sea and the East China Sea [M]. Beijing: Science Press, 1982. 39 - 51.

[7] Lei K, Yang Z S, Guo Z G, et al. Suspended sediment flux in spring on the East China Sea shelf with different surface sediment types [J]. Oceanologia et Limologia Sinica , 2001, 32(1):50 - 57.

[8] Su J, Jiang W S, Sun W X. Analysis of SPM data obtained in ocean investigation in the Bohai Sea [J]. Oceanologia et Limologia Sinica , 2001, 31(5): 647 - 652.

[9] Sun X G, Fang M, Huang W. Spatial and temporal variations in suspended particulate matter transport on the

Yellow and East China Sea shelf [J]. Oceanologia et Limologia Sinica, 2000, 31(6):581 - 587.

[10] Shang S L, ZHANG C Y, ZENG Y G. Field calibration of Chlorophyll fluorometer for Zhujiang River estuary and its adjacent sea areas of South China Sea [J]. Journal of Tropical Oceanography ,2004，23(5): 63 - 71.

[11] Xu X Q, Cao W X, Yang Y Z. Relationships between spectral absorption coefficient of particulates and salinity and chlorophyll a concentration in Zhujiang River mouth [J]. Journal of Tropical Oceanography, 2004，23(5):63 - 71.

[12] Shi X Y, Wang X L, Han X R, et al. Nutrient distribution and its controlling mechanism in the adjacent area of Changjiang River estuary [J]. Chinese Journal of Applied Ecology, 2003,14(7):1 086 - 1 092.

[13] Li D J, Li J, Chen J Y, et al. A study on suspended matter in the Changjiang River estuary [J]. Oceanologia et Limologia Sinica ,2000, 31(3):295 - 301.

[14] Hong huasheng,Qiu shunyuan,Ruan wuqi .et al.Minnan-Taiwan Bank Fishing Ground Upwelling Ecosystem Study [C]. Beijing: Science Press, 1991. 341 - 346.

[15] Zhang F, Huang B Q, Chen Z Z, et al. Vertical distribution features of temperature and chlorophyll a in Taiwan Strait in august, 1998 [J]. Marine Sciences, 2000, 25(9):1 - 5.

[16] Zhang F, Ruan W Q, Huang B Q. A study of multi-diel variation of chlorophyll a in southern part of Taiwan shoal [J]. Journal of Oceangraphy in Taiwan Strait, 2000, 19(3):322 - 328.

[17] Li L, Guo X G, Wu R S. Oceanic fronts in southern Taiwan Strait [J]. Journal of Oceangraphy in Taiwan Strait, 2000, 19(2):147 - 156.

[18] Zhen T M, Zhao Y Y, Li F, et al. The study of Suspended matter in the south Yellow Sea in summer [J]. Acta Oceanologica Sinica, 1990. 12(6):749 - 757.

[19] Zhuan W, Hu J Y, He Z G, et al. An analysis on surface temperature and salinity from southern Taiwan Strait to Zhujiang River estuary during july-august, 2000 [J]. Journal of tropical Oceanography, 2003. 22(4):68 - 76

[20] Xu J D, Guo X G, Li L, et al. Hydrology features in outer sea of eastern Guangdong in summer 2002 [J]. Journal of Oceangraphy in Taiwan Strait. 2003. 22(2):218 - 228.

[21] Wu R S, Li L. Summarization of study on upwelling system in the South China Sea [J]. Journal of Oceangraphy in Taiwan Strait. 2003, 22(2):269 - 277.

[22] Wang X L, Wen Q. Study on the carbon assimilation rate of phyto-plankton in the upwelling region in Minnan-Taiwan Bank fishing groud [J]. Acta Ecologica Sinica,1992，12(3):219 - 224.

夏季台湾浅滩周边水域悬浮物质浊度和叶绿素 a 荧光分布特征

胡 毅[1,2]，陈 坚[2]，和 转[2]

（1. 中国海洋大学地球科学学院，山东 青岛 266100；2. 国家海洋局第二海洋研究所，福建 厦门 361005）

摘 要：2004 年 7 ～ 8 月在台湾浅滩周边水域进行了两个断面的水体悬浮物浊度、叶绿素 a 荧光调查，通过对该区域悬浮物质浊度、叶绿素 a 荧光的夏季分布变化特征研究，结合水文相关要素分析，初步揭示了区域海洋沉积和再悬浮过程对悬浮体浊度、叶绿素 a 荧光分布的影响。指出悬浮物质浊度在近岸与陆架外缘主要受再悬浮作用影响，而浅滩区再悬浮作用不明显；在陆架外缘区浮游植物的聚集作用对浊度有一定的贡献作用，而近岸区则不明显。

关键词：台湾浅滩；悬浮物质；浊度；荧光

Relationship between Phytoplankton Distribution and Environmental Factors in the Chukchi Sea

LIN Geng-ming, YANG Qing-liang, TANG Sen-ming

Third Institute of Oceanography, State Oceanic Administration, Xiamen 361005, *Fujian Province, China*

Abstract: Based on the samples collected from the Chukchi Sea during the FCNARE cruise from July to August in 1999 with the "Xuelong", the research vessel of SOA, China, the relationship between the distribution characterization of phytoplankton and environmental factors was analyzed with Primer 5.2 software. The result showed that the assemblages of phytoplankton in Chukchi Sea can be divided into three ecological groups: Arctic-boreal group, distributed mostly in northeastern ice-edge where the depth is more than 2 000 m and affected directly by Arctic Ocean; Boreal group, distributed in shelf-break ice in the center water where the depth is less 100 m; Eurythermal group, mainly distributed in the south which exchanged with North Pacific water through Bering Strait. The species diversity, cell density and distribution variability of phytoplankton among stations were great different. The range of phytoplankton density among stations was 1.6×10^3 - $90\ 680.2 \times 10^4$ cells/m^3, and the ranges of diversity index and evenness index among stations were 0.07 - 0.87 and 0.33 - 3.82, respectively. Principal components analysis (PCA) showed that temperature and salinity had made important roles in the distribution of phytoplankton in the Chukchi Sea. Furthermore, the different influences of the variant water regimes, and the extremely dynamic physical nature of the drifting pack ice (e.g. packing, breaking up and melting) introduce short-term variability into the water conditions that no doubt affect the phytoplankton distrubition.

Keywords: Chukchi Sea; Phytoplankton, Distribution; Environmental factors; Multivariate analysis

1 Introduction

Global changes cause the fast changes of ocean and sea ice in arctic. As primary producer of arctic ocean ecosystem, phytoplankton is irreplaceable and important research object among the investigation of key scientific problems of Arctic changes(Chen et al.,2003; Wang ,1997). Although considerable data have been accumulated on the phytoplankton in Arctic Sea, little data is available on the phytoplankton distribution from East Siberian Sea to Chukqi Sea where the harsh Arctic climate like ice conditions is very obviously (Cecilie, 2003; Heimdal, 1989; Werner,1977; Yang et al., 2002, 2006). Furthermore, the comparability is low because the environmental conditions of Chukqi Sea is totally different from Bering sea and other ocean areas; there are different views about the potentially limiting role of nutriments as essential for phytoplankton growth in drifting ice (Gradinger,1995; Alexander, et al., 1996; Harri ,2006). This paper applies the Primer 5.2 software to analyze the relationship between phytoplankton distribution

Received on April 17, 2008

and the environmental factors under the conditions of the harsh Arctic climate like ice conditions etc.

2 Materials and methods

2.1 Sample collection

The samples were collected from 26 stations (Fig.1) in Chukchi sea （66°N - 74°N, 184°W - 204°W）during the FCNARE cruise from July to August in 1999 on the Xuelong Research Vessel of SOA, China. The phytoplankton samples were obtained by vertical plankton hauling (37 cm diameter opening and 280 cm long, with 0.077 mm mesh size) at the speed of 0.5 m/s from the bottom(from 200 m when the depth is greater than 200 m) to the surface .

2.2 Statistic analysis of data: By Primer 5.2 software

(1) The species diversity index (H') and evenness index (J) follow the formulae as below:

$$H' = -\sum_{i=1}^{s} p_i \log_2 p_i \quad \text{（Shannon-Wiever, 1963）}$$

$$J = H'/\log_2 S \quad \text{(Pielous, 1969)}$$

(2) Cluster analysis and multidimensional scaling (MDS) of community adopted Bray-Curtis comparability distance:

$$\text{B（j,k）} = \frac{\sum_{i=1}^{s} \left| X_{ij} - X_{ik} \right|}{\sum_{i=1}^{s} \left| X_{ij} + X_{ik} \right|} \quad \text{(Bray-Curtis,1957)}$$

where, *S* is the species quantity of sample, Pi is the ratio between the cells quantity of the species I and the quantity of total cells of sample; B (*i,k*) is the modulus of distance between sample i and sample k , *Xij* and *Xik* is separately the data of the species *i* in sample *j* and sample *k*.

(3) Filtration of species and datum handling

Because a large number of species occurred only occasionally and did not offer much useful ecological information, a criterion of selection of species was established before computation. The occurrence rate of the species was more than 10%, which were selected for cluster analysis and multidimensional scaling; In addition, the number of a species was transformed to square root and standardized by Primer software, thereafter, calculated Bray-Curtis comparability distance among samples and build comparability matrix.

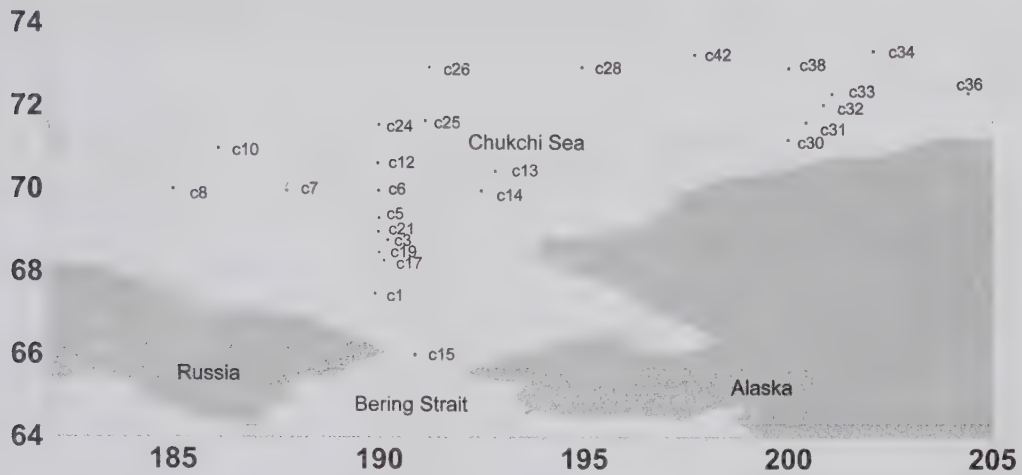

Fig. 1 Sampling stations in Chukchi Sea

3 Results and discussion

3.1 The species composition

A total of 103 taxa of phytoplankton were identified, consisting of 33 genera in 3 phylum (Tab. 1), and diatoms was the main component of phytoplankton in survey area, which was not only rich in species but also high in abundance and accounted for 99.96% of the total phytoplankton density. The dominant species are *Chaetoceros socialis, C. subsecundus, C. compressus, C. furcellatus, Nitzschia grunowii and Thalassiosira nordenskioldi* et al. of which *Chaetoceros* spp *and Nitzschia* spp accounted for 67.5% and 23.2%, respectively.

3.2 Ecological group and community structure

The cluster analysis showed that phytoplankton in Chukchi Sea can be divided into three ecological groups (seen in Fig. 2): (a) Arctic-boreal group, the representative species were *Bacteriosira fragolis* of typical Arctic species which was widely distributed in the Arctic seas. The species such as *Lauderia glacialis, Chaetoceros furcellatus, C. socialis, Nitzschia grunnowii, Thalassiosira nordenskioldi* et al. were the common species found in this survey. They were mainly distributed in the northeastern ice-edge (StasC42, C38, C36, C34 and C30 - C33) with depth more than 2 000 m and affected directly by Arctic Ocean of low temperature. (b) Boreal group, mainly distributed in shelf-break ice in the center water where the depth is less than 100 m. The dominant species were *Chaetoceros teres, C. debilis, C. curvisetus, Nitzschia longissima, Cylindrotheca closterium, Thalassionema nitzschia and Leptocylindrus danicus.* (c) Eurythermal group, including boreal oceanic group. The representative species were *Chaetoceros atlanticus, Corethron criophilum, Proboscia truncata, Proboscia imermis, Denticula seminae, Rhizosolenia setigera, Rhizosolenia styliformis, Asterolampra heptactis, Chaetoceros convoltus, C. borealis, Ceralitum*

longipes, Dinophysis acuminatad etc. They were mostly distributed from the south of Chukqi Sea (Stas C21,C17 and C19 et al.) to the vicinity of Bering Strait (Sta C15) where the exchange of North Pacific water of high temperature and salinity occurred.

Tab. 1 A list of phytoplankton species

species	species
Bacillariophyta	*C. subsecundus*
Achnanthes longipes	*C. pelagicus*
Amphiprora alata	*C. convoltus*
A. hyperborea	*C. laciniosus*
Asteromphalus hyalinus	*C. teres*
Asterolampra heptactis	*C. wighami*
Bacteriosira fragilis	*Cocconeis fasciolata*
Caloneis brevis	*Corethron criphilum*
Chaetoceros affinis	*Coscinodiscus asteromphalus*
C. atlanticus	*C. debilis*
C. borealis	*C. excentricus*
C. concavicornis	*C. curvatulus*
C. constrictus	*C. lineatus*
C. convoltus	*C. marginatus*
C. curvisetus	*C. oculatus*
C. compressus	*C. oculus-iridis*
C. decipiens	*C. radiatus*
C. debilis	*C. subtilis*
C. distans	*C. wailesii*
C. furcellatus	*Coscinodiscus* sp
C. gracile	*Cyclotella striata*
C. nipponica	*Cylindrotheca closterium*
C. socialis	*Dentecula seminae*
Diploneis splendida	*R. styliformis*
Eucampia balaustium	*R. setigera*
Fragilaria sp.	*R. stolterfothii*
Fragilariopsis kerguelensis	*R. hebetata* f. *hiemalis*
Fragilariopsis sp.	*Skeletonema costatum*
Lauderia borealis	*Stephanopyxis nipponica*
L. glacialis	*Synedra henndeiana*
Leptocylindrus danicus	*Synedra* sp.
L. minimus	*Thalassiosira baltica*
Melosira sulcata	*T. decipiens*
M. hyperborea	*T. gravida*
Navicula digitoradiata	*T. nordenskioldi*
N. granii	*T. subtilis*
N. septentrionalis	*T. rotula*
Navicula sp.	*Talassiosira* sp.
Pseudo-nitzschia pungens	*Thalassiothrix frauenfeldii*
P. delicatissima	*Thalassionema nitzschioides*
Nitzschia longissima	*Triceratium* sp.
N. grunowii	**Pyrrhophyta**
N. seriata	*Ceratium arcticum*
N. frigida	*C. fusus*
Nitzschia sp.	*C. tripos var subsalsum*
Pleurosigma sp.	*C. lineatus*
Proboscia truncata	*C. longipes*
P. imermis	*Ceratium* sp.
Rhizosolenia alata	*Dinophysis acuminata*
Protoperidinium catenatum	*P. pallidum*
P. conicoides	**Chrysophyta**
P. depressus	*Phaeocystis pouchetii*
P. pellucidum	*Dictyocha fibula*

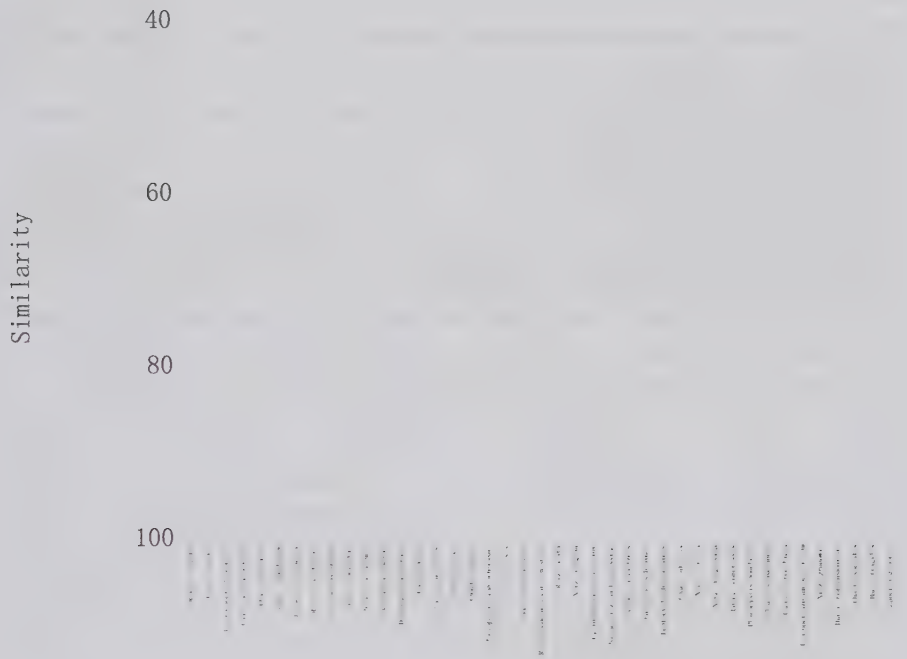

Fig. 2 Dendrogram of cluster analysis for phytoplankton groups from Chukchi Sea

Further analysis with multidimensional scaling (MDS) showed that the flora in Chukchi sea could be divided into 3 distinct communities (Fig. 3). It embodies the unification between ecological characterization of phytoplankton and its inhabit environment. Chukchi Sea connects with Bering Sea by Bering Strait, respectively influenced by the Arctic Ocean and the North Pacific at different degree, and phytoplankton in different water mass displayed different community characterization. Moreover, there were great difference of temperature and salinity existing between two adjacent stations because of uncertainty of arctic ices. Taking Stas C5 and C6 as example, the surface temperature and salinity of Sta C6 were 0.58 °C and 27.14, but the corresponding value of Sta C5 were 3.05 °C and 31.3. It is reflected that there were distinct physical environment variations during the melting time. It is showed in Fig. 3 that Sta C5 and Sta C6 fell into different communities. Obviously, there is close relationship between the phytoplankton distribution in Arctic sea and ice conditions, except the position of dynamic drifting ice, its physical conditions (e.g. packing, breaking up and melting) also introduce the distribution variability of phytoplankton in survey areas.

3.3 Horizontal distribution of phytoplankton cell density

The result showed that distribution of phytoplankton cell density among stations varied greatly. The variation of cell density was as high as 568 750 times, ranging from 1.6×10^3 cells/m^3 to 9.10×10^8 cells/m^3;

there was also great variation for the diversity index (H')and evenness index (J') among stations, where it differed in about 12 times. The average density of phytoplankton in Chukchi Sea was 8.32×10^7 cells/m^3, and higher density was located at Stas C21 and C17 in the south, where the density came to 9.0×10^8 cells/m^3. Secondly, it was more than 8.0×10^8 cells/m^3 in pack ice around the middle area (Stas C24 - C27) and StaC15, but lower densities (see Fig. 4) were located in deep water in the north (Stas C34, C36, C38 and C42) and the marginal drifting ice (Stas C30 - C33). Phytoplankton distribution in Chukchi Sea showed a trend of cell density decreased from the south to the north and the west was slightly higher than the east. By comparing the horizontal distribution of phytoplankton density, temperature and salinity (see Fig. 4 - 6), it could be seen that the spatial relationship between the phytoplankton density and temperature and salinity was generally consistent. Regression analysis showed that there was positive correlativity between the phytoplankton density and temperature and salinity in the survey area, and the coefficients of correlation were 0.908 and 0.812($a < 0.01 - 0.05$), respectively.

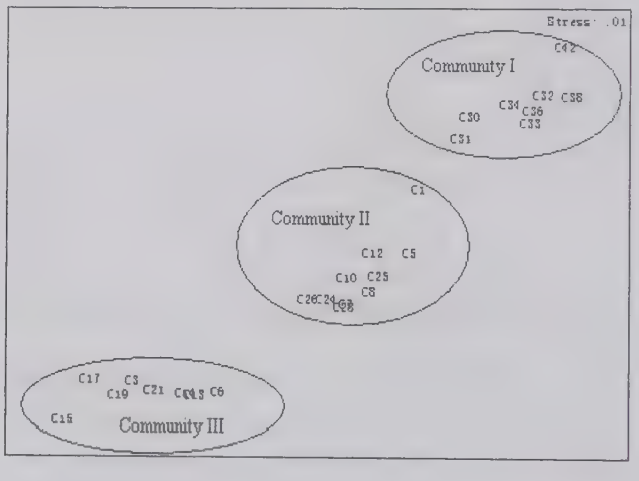

Fig. 3 The analysis of MDS in phytoplankton from Chukchi Sea

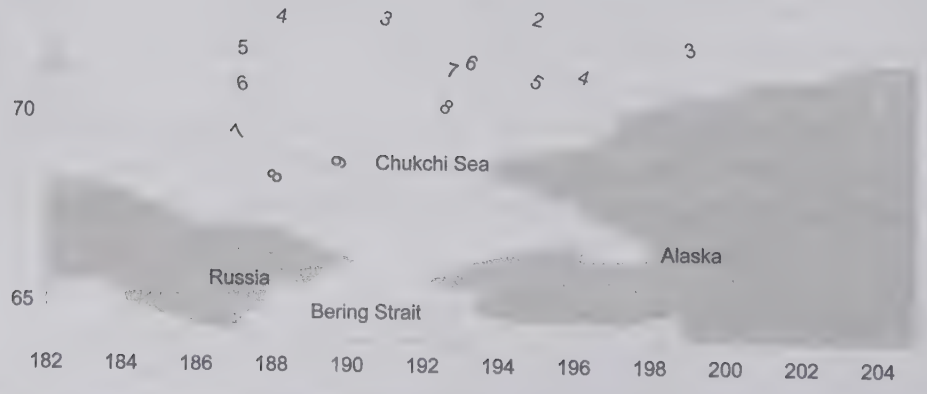

Fig. 4 Horizontal distribution of total phytoplankton cell density in Chukchi Sea (10^8cells/m^3)

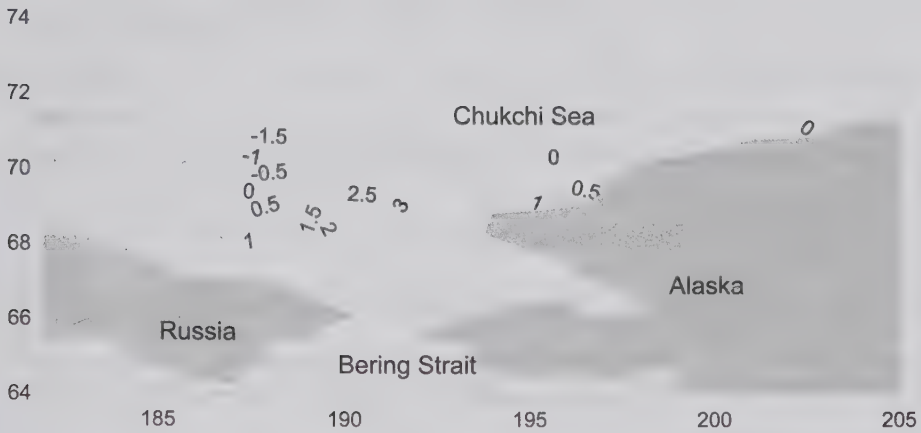

Fig. 5 Horizontal distribution of temperature in Chukchi Sea (Jul - Aug.1999)

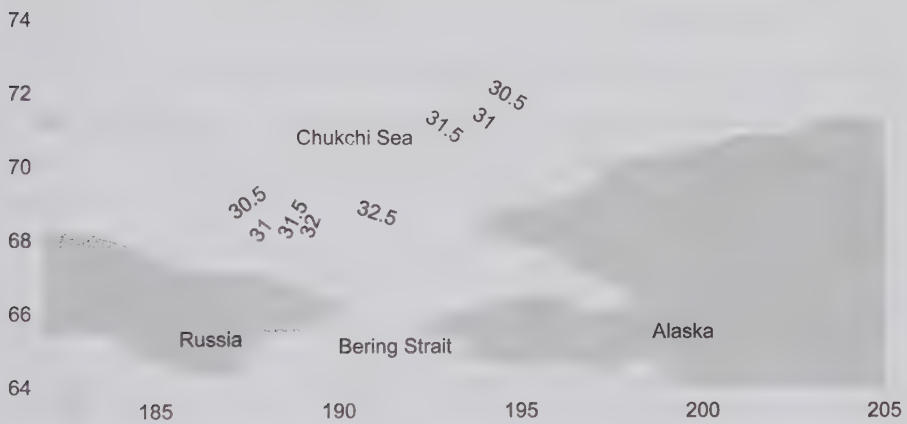

Fig. 6 Horizontal distribution of salinity in Chukchi Sea (Jul - Aug. 1999)

For the further analysis of environmental factors which determined the distribution of phytoplankton, the principal component analysis (PCA) was adopted according to physical-chemical parameters of each station. Five important factors were obtained, which explained 87.5% of total variability. As known from Tab. 2 and Tab. 3, the first principal component (PC1) explained 50.9% of the total variances, and correlated positively with phytoplankton, zooplankton, temperature and salinity. It is reflected that spatial distribution of phytoplankton in Chukchi Sea was mainly affected by water current and abundant phytoplankton hence the denseness of zooplankton. The second principal component (PC2) explained 21.3% of the total variances, and correlated negative with phytoplankton and nutriment. It is reflected that high nutriment concentration triggered the growth of phytoplankton. Moreover, PCA analysis provided further conclusion that the dominant factors which influence phytoplankton of Chukchi Sea were temperature and salinity, secondly nutriment. The above conclusions supported the conclusion that light and temperature are more important than nutriment for arctic phytoplanktons(Heimdal,1989), and also matched the geographical location of Chukchi Sea. Chukchi Sea is an approximately close bay,

surrounded by land and icecap, only exchanging with Bering Sea by Bering Strait of 55 km width in the south. Thus the distribution of phytoplankton in Chukchi Sea is mainly influenced by North Pacific waters with relatively higher temperature and salinity through the Bering straits, at the same time, influenced by terrigenous input and ice melting (Coachman et al.,1975;Sambrotto *et* al.,1984). Moreover, the Arctic bloom which in principle followed the retreating ice edge as it moves northward in summer. The high productivity of Chukchi Sea in summer assimilated nutriment which was an important supply of high nutrients transported by the Northern Pacific water to the Arctic ocean.

Tab. 2 Eigenvalues and percent of variation explained for the first 5 components of the PCA

Principal component	Eigenvalues	Percent of variation / %	Cumulative variation / %
1	3.70	50.9	50.9
2	1.84	21.3	72.2
3	0.70	8.0	80.2
4	0.65	6.3	86.5
5	0.07	1.0	87.5

Tab. 3 Factor Loadings of phytoplankton and environmental factors in PCA

Variable	PC1	PC2	PC3	PC4	PC5
phytoplankton	0.265	-0.586	0.129	-0.340	0.343
zooplankton	0.447	-0.148	-0.454	0.313	-0.381
temperature	0.482	-0.076	-0.418	-0.089	-0.114
salinity	0.382	-0.297	0.426	0.484	0.335
total nitrogen	-0.369	-0.343	-0.607	-0.085	0.457
phosphate	-0.253	-0.605	0.211	-0.202	-0.634
silicate	-0.389	-0.237	-0.095	0.705	-0.036

The extent of Arctic Sea ice during summer has declined to record minima during the past decade. These changes have a profound impact on many other aspects of Arctic and global climate, ecology and society. For example, many plankton and animal species have been migrating further north. According to the historical datum,the mixed water of Bering sea with North Pacific has direct influence on the waters to the north of 68°N，in this survey，it was in the south of 70°N. At the same time, the northwestern pacific indicator species like *Denticula seminae* was only limited in southern stations (Tang et al., 2001;Yang et al.,2002), while it extended to eastern of Alaska as well as a few stations of marginal drifting ice (Stas C30 - C33) in this survey, which showed the invasion of North Pacific waters.

Acknowledgements

This study was supported by the Ministy of Science and Technology survey project under contract

No.2006FY220700.

Reference

[1] Chen L Q, Zhao J P, Bian L G, et al. Marine Environment and Air-Sea Interaction in the Arctic Region [M]. Beijing: China Ocean Press, 2003, 339pp.

[2] Wang Z P. Marine biology process and global climatic changes in Polar Regions [J]. Donghai Marine Science, 1997, 15(3):29-35.

[3] Cecilie H, von Quillfeldt CH. Microalgae and Biodiversity in Polar Regions [P]. In: Iken K, Konar B eds. Proceedings of the Arctic Biodiversity Workshop: New Census of Marine Life Inititative. Alaska Sea Grant College Program, Fairbanks, Alaska, 2003, M-26, 131-149.

[4] Heimdal B R. Arctic Ocean Phytoplankton [J]. in:The Arctic Seas-Climatology,Oceanography,Geology,and Biology. (ed.Y. Herman),Van Nostrand Reinnold Company, New York, 1989, 193-222.

[5] Werner D. The biology of diatoms [M]. Botanical Monographs, Vol. 13. University of California Press, Berkeley, Califonia, 1977, 1-498.

[6] Yang Q L, Lin G M, Lin J H, et al. Species composition and distribution of phytoplankton in the Chukchi Sea and the Bering Sea [J]. Journal of Polar Research, 2002, 4(2): 113-125.

[7] Yang Q L, Lin G M. A multivariate analysis of netphytoplankton assemblages in the Chukchi Sea [J]. Journal of Plant Ecology, 2006, 30(5):763-770.

[8] R. Gradinger. Climate Change and Biological Oceanography of the Arctic Ocean [J]. Mathematical, Physical & Engineering Sciences. 1995, 352, 277 - 286.

[9] Alexander V, S Henrichs, H J Niebauer, et al. Bering Sea ice dynamics and primary production [R]. NIPR Symposium on Polar Biology. 1996, 9:13-25.

[10] Harri Kuosa. Changes in Phytoplankton Biomass and Nutrient Quantities in Sea Ice as Responses to Light/Dark Manipulations during different Phases of the Baltic Winter 2003 [J]. Hydrobiologia. 2006, 1:11-24.

[11] Coachman L K, K Aagaara, R B Tripp, et al. Bering strait: the regional physical Oceanography [M]. Seattle: University of Washington Press, 1975.

[12] Sambrotto R N, Goering J J, Mcroy C P, et al. Large yearly production of phytoplankton in Bering Strait [J]. Science, 1984, 225:1 147-1 150.

[13] Tang Y X, Jiao Y T, Zou E M, et al. Preliminary analysis of the hydrographic features and water masses in the Bering Sea and the Chukchi Sea [J]. Chinese Journal of Polar Research, 2001, 13, 57-68.

楚科奇海浮游植物的分布与环境因子的关系

林更铭，杨清良，唐森铭

(国家海洋局 第三海洋研究所，福建 厦门 361005)

摘 要：根据 1999 年 7 — 8 月“雪龙”号考察船在楚科奇海采集的样品，运用 PRIMER 软件分析该区网采浮游植物的分布特征及其与环境因子的关系。结果表明：楚科奇海浮游植物群聚可分为三个生态类群：北极—亚北极类群，主要分布于水深大于 2000 米且受北冰洋影响较直接的东北部浅水浮冰外缘；北方温带类群，主要分布于水深小于 100 米的中部浅水浮冰区；广温性类群，主要分布于通过白令海峡与北太平洋进行水交换的南部水域。该区浮游植物平面分布差异大，细胞密度站间变化范围为 1.6×10^3 ～ 90680.2×10^4，物种多样性指数和均匀度站间变化范围分别为 0.07 ～ 0.87 和 0.33 ～ 3.82。主成分（PCA）分析表明，对楚科奇海浮游植物分布起支配作用为水温和盐度。此外，由于该海区所处的特殊地理环境，浮冰的位置及其物理状态（聚集、开裂和消融等）均会增加浮游植物分布的变异。

关键词：楚科奇海；浮游植物；分布；环境因子；多元分析

《海洋通报》（英文版）加入《中国学术期刊（光盘版）》和《中国期刊网》全文数据库，入网“万方数据——数字化期刊群”以及加入《中文科技期刊数据库》的声明

为适应我国信息化建设的需要，扩大作者学术交流渠道，本刊已于 2001 年加入《中国学术期刊（光盘版）》和《中国期刊网》全文数据库，2004 年入网“万方数据——数字化期刊群”，2006 年加入《中文科技期刊数据库》，2007 年 6 月加入【中文电子期刊服务】（CEPS），其作者著作权使用费与本刊稿酬一次性给付。如作者不同意在本刊发表的文章入编上述数据库和网络，请在来稿时申明，本刊将做适当处理。

特此声明！

《海洋通报》（英文版）编辑部

Sequence Comparison of Mitochondrial 16S rRNA Gene between Two *Sesarma* Species

XU Jing-ming

College of Life Science and Technology, Chongqing University of Arts and Sciences, Chongqing 402168, *China*

Abstract: Partial sequences of the mitochondrial 16S rRNA gene were determined for two *Sesarma* species (*S. haematocheir* and *S. plicata*), and the length of sequence of *S. haematocheir* and *S. plicata* was the same. Of the 533 nucleotides obtained, the A, T, G and C contents were similar, which were 198 bp (37.1%), 206 bp (38.6%), 84 bp (15.8%), 45 bp (8.4%) and 200 bp (37.5%) , 205 bp (38.5%) , 81 bp (15.2%), 47 bp (8.8%) respectively. There were 49 different sites between the two species, including 21 transition sites, 22 transversion sites and 6 deletion/insertion sites. Furthermore, 361 bp homologous fragment was analyzed to discuss the phylogenetic relationship of 20 *Sesarma* species. The results showed that AT content (78.6% - 82.9%) was higher than GC content and there were 91 variable positions of 16S rRNA sequences among the 20 species. Among 3 *Sesarma* species in China, *S. dehaani* and *S. haematocheir* were closely related (*d*=0.0151); and there were greater genetic distances between *S. plicata* and *S. dehaani* / *S. haematocheir* (*d*=0.0924/0.0923). The average genetic distances of *S. plicata* , *S. dehaani* and *S. haematocheir* with the North American crabs of genus *Sesarma* were respectively 0.103 2 ± 0.008 9, 0.0783±0.0105 and 0.072 0 ± 0.011, which indicated that there were greater genetic differences between China and North American *Sesarma* crabs and they were monophyletic each other.

Keywords: *sesarma haematocheir*; *s. plicata*; 16S rRNA; phylogeny

The crab of genus *Sesarma*, which belongs to the Grapsidae, is mainly distributed in the marine intertidal and supratidal [1]. There have been some studies on molecular phylogeny and taxonomy in the *Sesarma* crab species [2-5]. Mitochondrial DNA has been extensively used in fishery study with features such as its compactness, maternal inheritance and a faster evolutionary rate compared to nuclear DNA [6-8]. Previous studies suggested that 16S rRNA was applied to study the phylogeny of crabs [9-14]. In this study, partial sequences of the mitochondrial 16S rRNA gene were determined for two species of *Sesarma*, which are *S. haematocheir* and *S. plicata*, and the fragments sequenced were used for the analysis of the genetic variations between them. Furthermore, phylogenetic relationships of 20 *Sesarma* crab species were discussed using the related gene sequences downloaded from the GenBank (Tab. 1).

1 Materials and Methods

1.1 Samples

The samples of *S. haematocheir* and *S. plicata* were collected from the coast of Rizhao,

Received on January 1, 2008

Shandong Province, and preserved in 95% ethanol. Three individuals of each species were used for sequence analysis.

Tab. 1 Base composition of 16S rRNA gene segment of 20 *Sesarma* species

Species	Abbreviation	Content / %					Total length / bp	Accession number
		A	T	G	C	A+T		
Sesarma haematocheir	*S. h*	39.6	41.2	13.6	5.6	80.8	359	DQ131499
S. plicata	*S. p*	40.2	40.4	13.3	6.1	80.6	361	DQ131500
S. dehaani	*S. de*	39.0	40.9	14.5	5.6	79.9	359	AY151822
S. verleyi	*S. v*	39.4	39.2	14.9	6.5	78.6	355	AJ225850
S. dolphinum	*S. do*	40.1	39.0	14.1	6.8	79.1	354	AJ225872
S. cookei	*S. co*	40.3	39.5	13.9	6.3	79.8	352	AJ225854
S. jarvisi	*S. j*	39.5	39.5	14.7	6.2	79.0	354	AJ225868
S. bidentatum	*S. b*	40.2	38.8	14.7	6.2	79.0	353	AJ005954
S. ayatum	*S. ay*	41.1	39.4	13.1	6.4	80.5	358	AJ005957
S. sp.	*S. sp*	41.2	39.2	13.2	6.4	80.4	357	AJ225891
S. windsor	*S. w*	41.9	38.8	12.7	6.5	80.7	353	AJ225849
S. rhizophorae	*S. rh*	40.6	40.1	12.9	6.4	80.7	357	AJ225851
S. curacaoense	*S. cu*	41.3	39.0	12.9	6.7	80.3	356	AJ225870
S. reticulatum	*S. ret*	40.8	39.2	13.2	6.8	80.0	355	AJ225867
S. fossarum	*S. f*	41.5	39.8	12.6	6.2	81.3	357	AJ225873
S. crassipes	*S. cr*	39.7	40.8	13.6	5.8	80.7	360	AJ225869
S. rubinofforum	*S. ru*	43.3	39.6	11.2	5.9	82.9	356	AJ225852
S. aequatoriale	*S. ae*	42.1	40.4	11.7	5.8	82.5	359	AJ225874
S. sulcatum	*S. su*	41.3	40.4	12.5	5.8	81.7	361	AJ225853
S. rectum	*S. rec*	40.3	41.1	12.5	6.1	81.4	360	AJ225866
Average of *Sesarma*		40.7	39.8	13.3	6.2	80.5		
Hemigrapsus sanguineus	*H. s*	36.9	39.1	16.3	7.7	76.0	350	AJ493054

1.2 DNA extraction

DNA was isolated from muscle tissue (about 60mg) of walking legs or claws using Classic Genomic DNA Isolation Kit (Bio Basic Inc of Canada).

1.3 PCR amplification

Selective amplification of a fragment of the 16S rRNA gene was carried out by polymerase chain reaction (PCR) with the primers L2510 5'-CGCCTGTTTAACAAAAACAT-3' and H3059 5'-CCGGTCTGAACTCAGATCATGT-3'. PCR amplification was performed in 25 μl reaction volumes

containing 2.5 μl 10×PCR buffer, 2.0 μl dNTPs (2.5 μM), 1 μl template DNA, .5μl of each primer (10 μM), 18.25 μl sterile deionized H_2O, and 1.25 units of *Taq* polymerase. Reactions were performed with an initial denaturation step at 94 °C for 90s, then 39 cycles of 94 °C, 30s / 49 °C, 45s / 72 °C, 60 s, and a final extension step at 72 °C for 5 mins.

1.4 Sequencing

The amplified products were electrophoresed on a 1.2% agarose gel and purified with Gel Extraction Kit (Watson Biotechnologies, Inc). Double-stranded PCR products were sequenced in both directions, using an ABI 377 automated sequencer (Perkin-Elmer Corp). The primers used for sequencing were the same as those for PCR amplification.

1.5 Data analysis

The sequences were edited and aligned by the DNASTAR software (DNASTAR, Inc). Phylogenetic and molecular evolutionary analyses were conducted using MEGA version 2.1(Arizona State University, Tempe, Arizona, USA). A 361 bp homologous fragment of 20 *Sesarma* crab species was adopted for phylogenetic analysis, using *Hemigrapsus sanguineus* as the outgroup.

2 Results and discussion

The complete alignment of the sequenced 16S rRNA gene region consisted of 533 positions, not including the primers (Fig.1). There was no sequence variation among three individuals of each kind of species. The lengths of sequences of *S. haematocheir* and *S. plicata* were the same, and the A, T, G and C contents were similar, which were 198 bp (37.1%), 206 bp (38.6%), 84 bp (15.8%), 45 bp (8.4%) and 200 bp (37.5%) , 205 bp (38.5%) , 81 bp (15.2%), 47 bp (8.8%) respectively. Aligned the sequences of the two species, there were 49 different sites, including 21 transition sites, 22 transversion sites and 6 deletion/insertion sites. The two sequences have been deposited in GenBank (Tab. 1).

After deletion of variable positions and compensatory mutations, 361 homologous bp was analyzed to discuss the phylogenetic relationship of 20 *Sesarma* species. It was clear that AT content (78.6% - 82.9%) was higher than GC content, and there was a little difference of A, T, G and C among 20 *Sesarma* species in contents (Tab. 1). The rarest base is C (average 6.2%). This pattern of base composition was consistent with the descriptions of other marine crustacean mtDNA sequences [15-18]. Fig. 2 shows the variation sites of 16S rRNA sequences among the 20 species above. They included 91 variable positions (Fig. 2).

```
S.h GTCTGTTTGA AGGTATAAAA AGTTTAACCT GCCCACTGAT AAAATTTTAA AGGGCCGCGG  [ 60]
S.p ....A....G ..A.....  ...C.....  ..T.....  .TT.....T.  ..A.....  [ 60]

S.h TATTCTGACT GTGCAAAGGT AGCATAATCG TTAGTTTTTT AATTGGAATC TTGTATGAAT  [120]
S.p ..........  ..........  ..........  ..........  .....A....  .....  [120]

S.h GGTTTGACAA AAAAAAATCT GTCTTTATAA TTATTTATTG AATTTAACTT TTAAGTGAAA  [180]
S.p ........G.  ......GA..  ..........  .....A....  .......T..  .....  [180]

S.h AGGCTTAAAT AAATTAAAAA GACGATAAGA CCCTATAAAG CTTAATATTA TATTTTTATT  [240]
S.p ..........  ..G.......  ..........  ..........  ..........  AT..C.....  [240]

S.h TAATTAAATT TTAAATTTTA TATAAAAATT TGGTAAATAA ATTTTATTTT ATTGGGGTGA  [300]
S.p ....A.....  ...--...A.  ......TG..  ......-...  T.........  .....  [300]

S.h TAATGGTAAA ATGATTATTA ACTGTTAAAT TT-TTTAGAC AAAAATAAAT GAATAGTAAT  [360]
S.p ..........  .....C.A..  ........T.  ..A....A..  ...G......  ..T..AA..C  [360]

S.h TGTTA-----  TAAAGGATCC TGTATTAAAG ATTAAAAGTT TAAGTTACTT TAGGGATAAC  [420]
S.p .TA..ATTAA  ....T.....  .A.-......  ...T......  .....  .....  [420]

S.h AGCGTTATTT TTTTTGAGAG TTCTTATCGA GAAAAAAGTT TGCGACCTCG ATGTTGAATT  [480]
S.p .....A....  ..........  ...A......  ..........  ..........  .....  [480]

S.h AAAATATCTA TATAATTGCA GTAGTTATAT AAGAAGGTCT GTTCGACCTT TAAAATTTT [539]
S.p ..........  ........T.  .C........  ..........  ..........  ....--..A [539]
```

Fig. 1 Sequences alignment of the 16S rRNA segments of *S. haematocheir* and *S. plicata*

Genetic distance among 20 *Sesarma* crab species was calculated based on Kimura 2- parameter method. The molecular phylogenetic tree was constructed by the neighbor-joining method. Statistical significance of groups within inferred trees was evaluated by bootstrapping with 1 000 replications (Fig. 3).

In this study, 17 of 20 species of the crab genus *Sesarma* are distributed in North America, the others, *S. haematocheir*, *S. dehaani* and *S. plicata*, in China. Among them, *S. dehaani* and *S. haematocheir* have the closest relation that the genetic distance between them was only 0.015 1, but the distances of *S. plicata* with *S. dehaani* and *S. haematocheir* were 0.0924 and 0.092 3, respectively. The average genetic distances of *S. plicata* , *S. dehaani* and *S. haematocheir* with the North American crabs of genus *Sesarma* were respectively 0.103 2 ± 0.008 9, 0.078 3 ± 0.0105 and 0.072 0 ± 0.011, but the average genetic distance among the North American crabs of genus *Sesarma* was only 0.040 7 ± 0.015 1, which indicated that there were greater genetic differences between the crabs in China and North America and they were monophyletic each other.

All data were in agreement that *S. dehaani* and *S. haematocheir* were the most basal species, and the molecular data strongly supported the close phylogenetic relationship between them. The result corresponded with that *S. dehaani* and *S. haematocheir* shared close geographic and morphological proximity. They were both supratidal species and occupied the similar habitats. The next species to branch off was the intertidal species, *S. plicata* (Fig. 3), and were not same in habitat and had bigger morphological differences with the former [1]. These results are inclined to support the view that *S. plicata* belongs to the genus *Parasesarma* [19].

```
[                                1111111 1111111111 1111111111 1111122222 ]
[      11344444 5555666666 6780011244 4444555566 7777888889 9999901111 ]
[     1967602489 6789123568 9503512123 4568268969 1239012580 2456741678 ]
S.ae  -CAGTAAAAT T-ATAT-ATT ATCAAAAGAT TT-ATAAATT --AATATGAT ATTTAATATA
S.ay  -.G...G..A CACA..-.A. .......... ..T....... AA.....A.. .........G
S.b   -.G...G..G CA-GG.-.A. .......... ..T.....-- AA.....A.. ....G....G
S.co  -.....G.G. .A.G..A.A. ...GG..T.. ..T...G..- GA-....A.. .........G
S.cr  -.....G... .T....-... .......... ..G....... AT...G.... G.........
S.cu  -.G...G... CA-C.C-... .......... ..T....G.- AA.G...... ..........
S.do  -.....G... CA-C..-.G. G...G..... ..T..G.... AA...G.... .....G....
S.f   -......... CA-...-.G. .......... ..T....... AA........ ..........
S.h   -TG....... .T....-... .......... A.TT..T.A. TT..A....A .A..T....G
S.j   -.....G... CAT...-.G. ....G..... ..T.......- GAG....A.. ....G..G..
S.p   -TGA.G..GA .T....-..A ..T.G....A ..TC....A. TA...G.... ....T....G
S.rec -.G....... .T....-.C. .......... ..TT...GA. AT.....A.. ..........
S.ret -.G...G... CA-C..-... .......... ..T....G-- AA.G...... ..........
S.rh  -.G...G... CA-C..-... ...G...... ..T....G.. AA...G.... ..........
S.ru  -......... .T....-... ........G. ..A......A TA........ ...A......
S.sp  -.G...G..A CACA..-.A. .......... ..T....... AA.....A.. .........G
S.su  -......... .-..G.-... .......... ..G....... --........ .........G
S.v   -.....G... CA-C..-.A. ....G..... A.T....... AA.G.G.... .........G
S.w   -.....G... CA-C..-.A. .......... ..T....... AA........ ..A.......
S.de  -TG....G.. .T....-... .........A A.TT..T.A. AT..G....A .A..TG...G
H.s   GTG.G..G.. .-..GGTG.. CA...GG..G AATCCGT..- TAT.A.CAG. .G..-.C.G.

[      2222222222 2222222222 2222222222 2222223333 333333333]
[      1223334444 4555556777 7777777888 8888990000 114556667]
[      9791782356 7026788012 3456789012 3567290256 234140291]
S.ae   AATTG-ATGA -AAAAAAAT- AA-AATTTAA AATGTA-AAA AATTGTTAA
S.ay   .....-...- -.........A ..-G....TG ..--.G-..G .........
S.b    .....-...- -.........A ..-GT...TG ..--GG-..G .........
S.co   ....A-..A- -......T.-- G.-.G...-. ..--.G-..G ......C..
S.cr   .....-...G -.........A .GTTTA..GT ..--.G-.... .........
S.cu   .....-.... -.........A ..ATGA..T. G.--..-.... ....A....
S.do   .....-..A- -.......CAA ..-.G..--. ..--.G-..G .........
S.f    .....-..A- -.........T ..-.GA..T. G.--.GA..G .........
S.h    G....-.ATT -TG.....GT ..--T.-GTT ..--GG-.... .......G.
S.j    .....-...- -..G.....A ..-.G...-. ..--.G-..G .G.......
S.p    G.CA.-..TT AT...GT.-- ..A.C..AT. .TAA..-T.. T.A...AG.
S.rec  .....-...T -T...T..AT ..A.T..... ...-.G-..G .......G.
S.ret  .....-..A. -.T......A ..ATGAC.T. G.--..-..G .........
S.rh   .....-..AT -.........A ..-T.A..T. G.--..-.... .........
S.ru   .....-..A. -.......-- -.-..A..... ..--..-.... ....A....
S.sp   .....-...- -.........A ..-G....TG ..--.G-..G .........
S.su   .....-.... -.........T ..-....... ......-.... .........
S.v    .G...-G.A- -.....G..A .G-GT..GT. ..--.G-..G .........
S.w    .....-...- -......G.- -.-..A..T. ..--.G-..G ......A..
S.de   G....-..TT -TG.....AT ..--T..GTT G.--GG-.... .......G.
H.s    G....C..T- -.TTTTTG-- ..--T...-- -.--..G.G. ...CAAA.G
```

Fig. 2 Variation sites in 361 bp segment of 16S rRNA gene among 20 *Sesarma* species

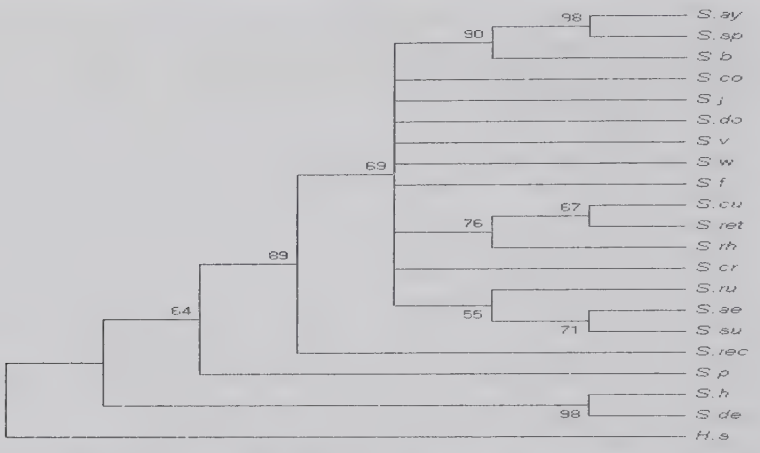

Fig. 3 Neighbor-joining molecular phylogenetic tree of 20 *Sesarma* species using *Hemigrapsus sanguineus* as the outgroup

Acknowledgements

This work was supported by the special grant of Chongqing University of Arts and Sciences for the person with ability. We are grateful to Researcher Wang Yongliang in the Institute of Oceanology, Academia Sinica for his help of identifying the samples.

References

[1] Dai A Y, Yang S L, Song Y Z, et al. Crabs of the China Seas [M]. Beijing: China Ocean Press, 1986, 456-517.

[2] Schubart C D, Diesel R, Hedges S B. Rapid evolution to terrestrial life in Jamaican crabs [J]. Nature, 1998, 393: 363-365.

[3] Schubart C D, Cuesta J A, Diesel R, et al. Molecular phylogeny, taxonomy, and evolution of nonmarine lineages within the American Grapsoid crabs (Crustacea:Brachyura) [J]. *Molecular Phylogenetics and Evolution*, 2000a,15(2): 179-190.

[4] Schubart C D, Neigel J E, Felder D L. The use of the mitochondrial 16S rRNA gene for phylogenetic and biogeographic studies of Crustacea [J]. Crustacean Issues, 2000b, 12: 817-830.

[5] Sun H Y, Zhou K Y, Yang X J. Phylogenetic relationships of the mitten crab as inferred from mitochondrial 16S rDNA prtial sequences (Crustacean, Decapoda) [J]. Acta Zoologica Sinica, 2003, 49 (5): 592 - 599.

[6] Avise J C. Phylogeography [M]. London: Harvard University Press, 2000, 10-12.

[7] Brown W M. Evolution of mitochondrial DNA [A]. In: Nei M , Kochn R. *Evolution of genes and proteins*. [C] Sunderland MA, Sinauer, 1983, 62-88.

[8] Lu G Q, Li S F. Advances in the study and application of fish mitochondrial DNA polymorphism [J]. Journal of Fishery Sciences of China, 1998,5(3): 94-103.

[9] Harrison J S. Evolution, biogeography, and the utility of mitochondrial 16S and COI genes in phylogenetic analysis of the crab genus *Austinixa* (Decapoda:Pinnotheridae) [J]. Molecular Phylogenetics and Evolution, 2004,

30: 743-754.

[10] Qiu G F, Xu Q T, Wang L Q, et al. Molecular taxonomy and phylogeny of four species of *Eriocheir* (Decapoda: Brachyura: Grapsidae) [J]. Acta Zoologica Sinica, 2001, 47(6): 640-647.

[11] Schubart C D, Neigel J E, Felder D L. Molecular phylogeny of mud crabs (Brachyura:Panopeidae) from the northwestern Atlantic and the role of morphological stasis and convergence [J]. Marine Biology, 2000c, 137: 11-18.

[12] Schubart C D, Cuesta J A, Rodríguez A. Molecular phylogeny of the crab genus *Brachynotus* (Brachyura: Varunidae) based on the 16S rRNA gene [J]. Hydrobiologia, 2001, 449: 41-46.

[13] Sun H Y, Zhou K Y, Jing K Y, et al. The systematic positions of genus *Helice* inferred from mitochondrial 16S rDNA partial sequences [J]. Journal of Nanjing Normal University(Natural Science), 2002, 25(1): 15-19.

[14] Weinberg J R, Dahlgren N D, Halanych K M. Genetic differences within and between species of deep-sea crabs (*Chaceon)* from the North Atlantic Ocean [J]. Biological Bulletin, 2003, 204: 318-326.

[15] Gao T X, Li J, Wang Q Y, et al. Sequence analysis on mitochondrial 16S rRNA gene in *Fenneropenaeus chinensis* [J]. Journal of Fishery Sciences of China, 2003, 10(5) :359-364.

[16] Palmero I, Renart J, Sastre L. Isolation of cDNA clones coding for mitochondrial 16S ribosomal RNA from crustacean Artemia [J]. Gene, 1988, 68: 239-248.

[17] Nobumitsu S U, Fumiyo S, Satoshi C, et al. Morphological stasis and phylogenetic relationships in Tadpole shrimps, *Triops*(Crustacea: Notostraca) [J]. Biological Journal of the Linnean Society, 1997, 61: 439-457.

[18] Quan J X, Zhuang Z M, Deng J Y, et al. Phylogenetic relationships of 12 Penaeoidea shrimp species deduced from mitochondrial DNA sequences [J]. Biochemical Genetics, 2004, 42(9/10): 331-345.

[19] Serene R, Soh C L. New Indo-Pacific genera allied to *Sesarma* Say 1817 (Brachyura, Decapoda, Crustacea) [J]. Treubia, 1970, 27: 387-416.

相手蟹属两种蟹类线粒体 16S rRNA 基因序列的比较

徐敬明

（重庆文理学院 生命科学与技术学院，重庆 402168）

摘 要：测定了相手蟹属（*Sesarma*）红螯相手蟹（*S. haematocheir*）和褶痕相手蟹（*S. plicata*）线粒体 16S rRNA 基因部分片段的序列，二者的序列长度相同，均为 533 bp，且 A、T、G、C 的含量相似，分别为 198 bp (37.1%), 206 bp (38.6%), 84 bp (15.8%), 45 bp (8.4%) 和 200 bp(37.5%) , 205 bp (38.5%) , 81 bp (15.2%), 47 bp (8.8%)；二者的序列有 49 处差异，其中 21 个位点为转换、22 个位点为颠换和 6 个缺失/插入位点。进一步对 20 种相手蟹属蟹类的长度为 361 bp 的 16S rRNA 基因同源序列进行分析，发现 AT 的含量为 78.6% ～ 82.9%，明显高于 GC 的含量，且存有 91 个变异位点。从 NJ 树和遗传距离来看，在分布于中国的 3 种相手蟹中，无齿相手蟹（*S. dehaani*）和红螯相手蟹的亲缘关系最近(*d*=0.015 1)，而它们与褶痕相手蟹的亲缘关系则较远(*d*=0.092 4/0.092 3)。分布于中国的相手蟹和分布于北美的相手蟹之间存在着较大的遗传距离（差异），表明它们之间有着较远的亲缘关系，互为单系起源。

关键词：红螯相手蟹；褶痕相手蟹；16S rRNA；系统发生

Sedimentary Environment Analysis of Ancient Sand Ridges from Zk23 Hole in the East China Sea

DU Wen-bo[1], YE Yin-can[2], ZHUANG Zhen-ye[3]

1. *East China Investigation and Design Institute under CHECC, Hangzhou* 310014, *Zhejiang Province, China;*
2. *Second Institute of Oceanography, SOA, Hangzhou* 310012, *Zhejiang Province, China;*
3. *College of Marine Geosciences, Ocean University of China, Qingdao* 266100, *Shandong Province, China*

Abstract: Based on the analysis of core samples from the hole of Zk23 in the East China Sea Continental Shelf and by means of sedimentary stratigraphy, biostratigraphy and chronostratigraphy, the authors consider that the fine-sand deposition in borehole was part of buried ancient estuary sand ridges of the Yangtze River. The deposition history of study area around the hole before and after the glacial period as well as postglacial period is made clear after our research: (1) the estuarine sublayer -undersea delta facies strata was deposited under the fast sea level rise about 15 kaB.P; (2) sand ridges mostly consisting of fine-sand, were formed when the sea level was the fluctuant range of 60 - 80 m of isoba[illegible] during the deglacial period around 15 - 12 kaB.P; (3) first silty clay and clay silt strata above the sand ridges were deposited during the period when the sea level rose fast from 12 to 7 kaB.P. and then it keeps stable to the present.

Keywords: ancient sand ridges; sedimentary environment; East China Sea Continental Shelf

Sand ridges on the continental shelf are common features in the modern seabed, so it has important significance to study and recognize them, which can not only heighten the theory of shallow sea sediment dynamics, but also improve the study of marine engineering and military affairs oceanography. This paper analyzed formation environment of the buried sand ridges outer continental shelf in the East China Sea and supplied new science gist to study sand ridges in the East China Sea Shelf based on data from a bore of engineering geology.

Many ancient sand ridges are distributed at the water depth of 60 m - 120 m on continental shelf in the East China Sea, mainly in the south of 31°N. They stretch in NW-SE directions, ridge alternate with trough and they diverge toward SE orientation [1-4]. The borehole Zk23 locates in side limb of an ancient sand ridge which is in middle-south of the East China Sea Shelf (28°42′N, 123°53′E), and it is the first drill core that directly penetrated sand ridge and was limited by age (Fig. 1). The author analyzed it with Sediments' granularity, micro-paleobiology, and ages determinate by ^{14}C and studied the characteristics of stratum and sedimentary environment.

Received on March 24, 2008

1 Regional setting

Continental shelf basin of the East China Sea is one of many tectonic basins which locate in inner west margin of structures around the Pacific Ocean, the borehole Zk23 locates in settlement regions that belongs to the first level structure units of continental shelf basin in the East China Sea. The East China Sea shelf is gentle topography and from northwest inclined to southeast. Its average gradient is 58″the minimum is 34″and average water depth is 72 m [5]. The boundary line between inner shelf and outer shelf is at 50 m - 60 m depth, the borehole lies to the western side in outer shelf.

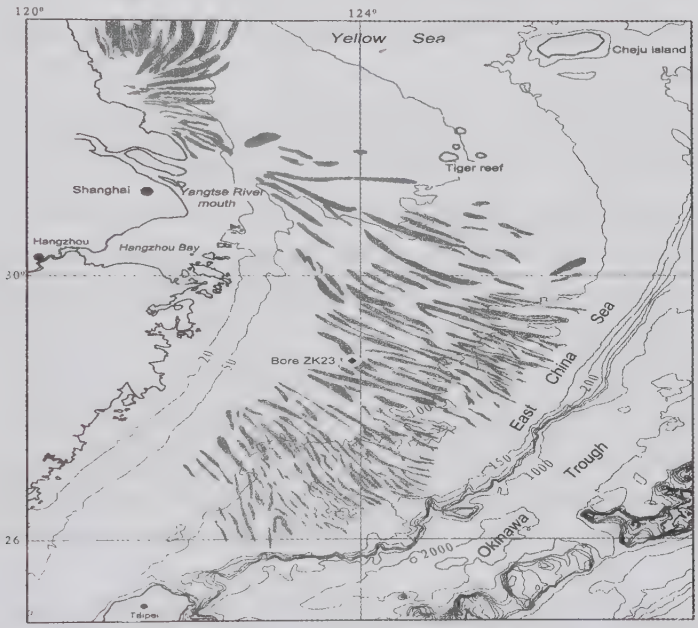

Fig. 1 Distribution of sand ridges in the East China Sea Continent Shelf and Zk23 Position

(By LI Guang-xue et al.[6],modified)

The East China Sea level is about 130 m of isobath at the lowest during the last glaciation maximum, and later the whole trend is rising up, fluctuating up and down during deglaciation period. Abounding sand ridges grew up around the water depth of 60 m - 120 m [2, 3,11], and the sea level rose fast during ten thousand years in the post-glacial period, and then it rise up to the present coast line in 6 - 7 kaB.P [12].

2 Methods

We obtained 15 core units which more typically by the changes of sedimentary components and granularity in different depth during the course of opening this core from top to bottom, each unit is in the length of 20 cm, and then we tested and analyzed them. The granularity analyses of core have been done by sieve analysis, and micro-paleobiology was authenticated by the lab geology minerals of Tianjin; age

^{14}C was tested by the way of dilution in the check and measure center of marine geology in china geological survey, and test sample is gray clay. The author drew a Geological column profile and others maps then analyzed sedimentary environment using these test data of having tested.

3 Stratum of borehole Zk23

The stratum of borehole Zk23 can be divided into three layers from top to bottom: I layer (fine grain), II layer (coarse grain), III layer (granule). Each layer connects with interlayer gradual change, the stratum as follows:

(1) III layer Burying depth is 8.5 - 9.3 m, and thickness is 0.8 m; it mainly consists of grayness clayey silt(silt content reaches 50.43% - 56.90%) , contained lamellas of fine sand and clay, and a few of shell detritus. Sediments average size is more fine (Mz, 5.33 φ), and separation is bad (σ_I,2.27 - 2.56). Skewness is about zero(Sk,－0.10 - 0.12). Kurtosis is even and middling(Kg,0.75 - 0.97).

This layer contains foraminifera and marine ostracodes, such as *Heterolepa subpreecincta*, *Florilus decorus, Pseudorotalia gaimardii*, *Cibicedes pseudoungerianus*. There are little swim species but shallow-water to deep-water species are all present, as fragments of *globigerina.SP. glatinata* etc which presents shallow-water species, *Neogloboquadrina parchyderma*, *Pulleniatina obliquiloculata*, *Globorotalia truncatulinoid*, and so on those that present species lived in deep-water far away ocean. Marine ostracodes shallow-water species appear in onshore and intertidal zone such as *Bicornucythere bisanenis*, *Cushmanidea subjaponica*, *Sinocytheridea impressa*. And there also included inshore species (like oyster) chips of mollusk. This layer gradually changes to II layer by interlayer lamella sand on the top with burying-depth of 8.5 m , and the age is （15 480 ± 650）aB.P. using ^{14}C tested (burying depth 8.5 m. gray clay).

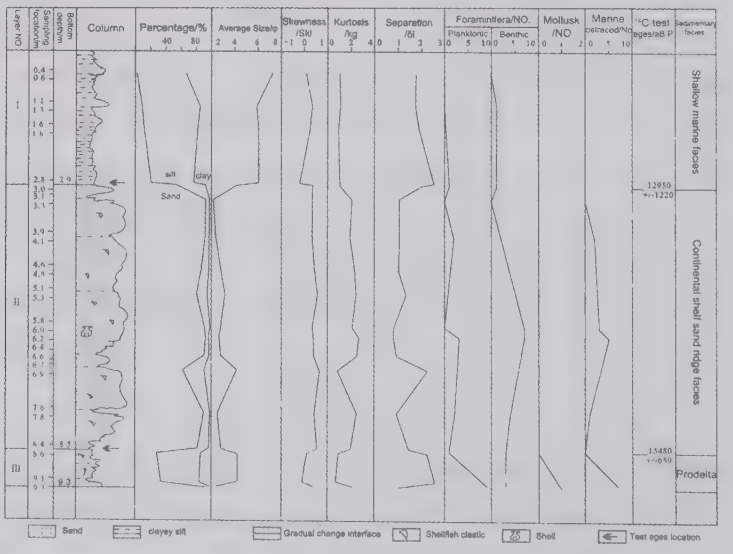

Fig. 2 Geological column profile of core Zk23 in the East China Sea Shelf

(2) II layer Burying depth is 2.9 m - 8.5 m, and thickness is 5.6 m; it consists of gray fine sand and silty fine sand clayey, and occasionally appears interlayer lamella of clay. Sand content reaches 53.86% - 92.54%, biological shell detritus presents in all layer. Sediments average size is more coarse (Mz, 2.21 - 4.21 φ), and separation is middling (σ_I, about 1.0). Skewness mostly is positive (Sk, 0.35 - 0.66). Kurtosis is acuity (Kg, about 2).

This layer contains abundant benthic foraminifera and marine ostracodes, and few planktonic foraminifera, no shell detritus of mollusk. Benthic foraminifer is the species of onshore estuary, mostly is *Ammonia beccarii* vars, and others are *Florilus decorus*, *Pseudorotalia gaimardii*, *Quinqueloculina lamarckiana*, *A. convexedorsa* Zheng, *Cribrononion incertum*, *Heterolepa subpreecincta*, *Paratotalia inermis* and so on. Marine ostracodes mostly are *Bicornucythere bisanenis, Cushmanidea subjaponica* and *Sinocytheridea impressa*.

(3) I layer Burying depth is 0 m - 2.9 m, and it consists of gray silt and clay silt. Silt content reaches more 56.95% - 76.52%, clay is 15.01% - 33.31%. Horizontal bedding can be found, and the depth of lamina is about 1 mm, and there are few fine sand interlayers with the depth of about 1 cm and fragmentary biological detritus. The sediments average size is more fine(Mz, 6.03 - 7.26φ), and separation is bad to worse (σ_I, 1.76 - 2.54), Skewness is more positive (Sk, −0.17 - 0.32), Kurtosis is middling (Kg, 0.96 - 1.12).

Micro-paleobiology is few in this layer, and there are shallow warm water species *Pseudorotalia gaimardii* in the depth of 1.1 - 1.3 m, fragments of *globigerina.sp.* and *Florilus decorus* in the depth of 2.8 - 3.0 m. This layer gradually changes to II layer by interlayer lamella sand on the bottom whose burying-depth is about 2.9 m , the age is (12 950 ± 1 220) aB.P. by using ^{14}C tested (burying depth is 2.9 m, gray clay).

4 Sedimentary environment

The stratum of borehole Zk23 consists of three layers: fine grain clay silt in bottom (III layer) and fine grain silt on the top (I layer) and coarse grain fine sand at middle part (II layer). The middle part fine sand is depth of 5.6 m which almost contains most of the core. We analyzed sedimentary environments of each layer by means of data that we have attained.

4.1 The middle fine sand layer (II layer)

This layer was limited by age of ^{14}C test from boundary top to bottom, the earlier age is (15 480 ± 650) aB.P. later is (12 950 ± 1 220)aB.P., which indicated that the fine sand layer with the depth of 5.6 m deposited during 15 000 - 12 000 aB.P. Accounting to changes of East China Sea [9], the sea level had fluctuant range of 60 m - 80 m of isobath during the deglaciation. The depth of water is 82.3 m in borehole Zk23, which stands in the zone of alongshore shallow-water or onshore. So we can conclude that this layer is alongshore or onshore face according to chronostratigraphy.

This layer contains abundant benthic foraminifera living in alongshore estuary, especially the *Ammonia beccarii* vars., and secondly *Florilus decorus*, *Pseudorotalia gaimardii*, *Quinqueloculina lamarckiana*, *A. convexedorsa* Zheng, *Cribrononion incertum*, *Heterolepa subpreecincta*, *Paratotalia inermis* and so on. Those abundant fit together the species which alongshore estuary biology and others much species of euryhaline ostracodes in inshore estuary, and all these together sufficient indicated that this layer living in alongshore estuarine sedimentary environments by the biostratigraphy.

We have tested three sample teams and have got detailed grain-size analysis to this layer (Tab. 1). Probability curve we have drawn presents four segments, and the middle segment is spring component, which shows two segments and its up and down note are at around 3.2 φ and 1.5 φ (Fig. 3a). It shows the complex cross hydrodynamic environments are two items or much more, such as wave and tidal current or tidal and fluvial actions et al., which are interacted affecting environments of onshore shallow-water dynamic. Frequency curve has obvious characteristics that showed bimodal distribution, positive skewness and slightness tail (Fig. 3b), which indicated much source sediments and the action of fluvial (later). Sediments grain size less than 2 φ- 3 φ usual are not transferred, and those fine grain exceeding 4 φ are gradually fallen deposited during the course of suspending(Fig. 3b). In the C-M drawing, those test points in this layer are all fallen in the Ⅴ zones of QR segment, which are belongs to the zone of gradual changes suspend deposit (Fig. 4), and illuminates that the stream begins to show characteristics of stretched currents and water becoming widen takes on deposition of estuary and delta in this zone.

We summarized those evidences of sedimentary stratigraphy, biostratigraphy and chronostratigraphy et al., considering that this layer deposit belongs to alongshore estuary sedimentary environments. Consulting the theory of ancient estuary sand ridges of Yangtze River by Yangwenda[13] and Lishaoquan[14] and the watercourse deposit of underwater delta rebuilt with tidal currents by Liuzhenxia[15, 16], all those can sufficiently shows that the fine-sand deposition depth of 5.6 m was underwater ancient estuary sand ridges of the Yangtze River.

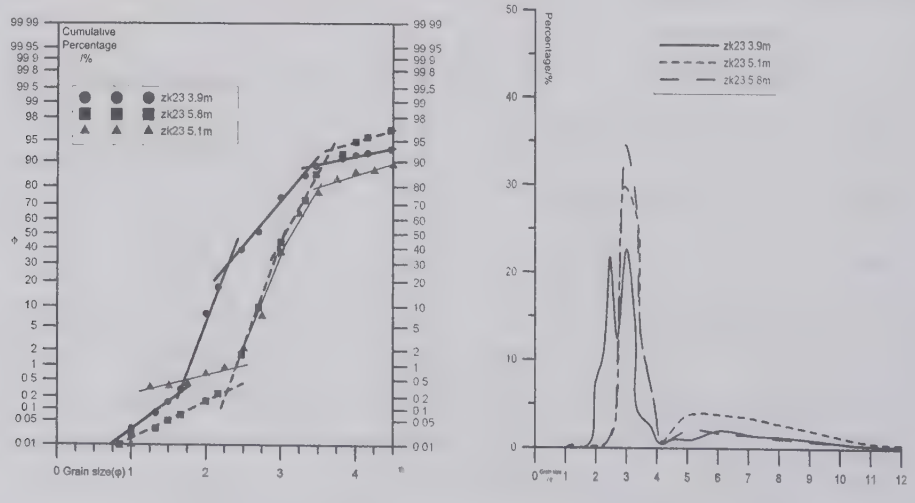

(a) Probability curve of grain size (b) Frequency curve of grain size

Fig. 3 Probability curve (a) and frequency curve (b) of grain size of layer Ⅱ in Zk23 in the East China Sea Shelf

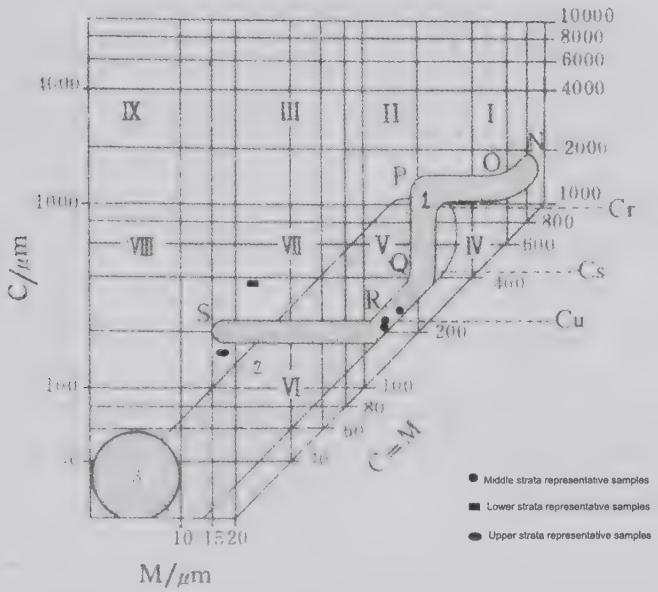

Fig. 4 Distributions of samples of Zk23 in the C—M drawing

4.2 The bottom silt layer(Ⅲ layer)

This layer with burying depth of 8.5 m - 9.3 m are interlayer of silt and clay (Tab. 2) and horizontal bedding each lamina depth is 0.5 mm - 1 mm. We can conclude that this layer still stands in subtidal zone and prodelta sedimentary environments, by the combinations analysis of micro-paleobiology which included species of shallow-warm water and benthic alongshore and shallow-water onshore marine ostracodes, and abundant shell crumbs and little shell fragments of mollusk.

Tab. 1 Data of grain size by sieve analysis

Grain size		Depth / m					
		3.9 - 4.1		5.1 - 5.3		5.8 - 6.0	
D / mm	φ	Percentage / %	Cumulative Percentage/ %	Percentage / %	Cumulative Percentage/ %	Percentage / %	Cumulative Percentage/ %
<0.045	<4.47	6.63	93.37	11.05	88.95	3.31	96.69
0.045 - 0.056	4.16	0.96	92.4	1.93	87.01	1.06	95.64
0.056 - 0.063	4	0.51	91.89	0.76	86.25	0.75	94.88
0.063 - 0.071	3.82	0.93	90.96	3.02	83.23	2.80	92.09
0.071 - 0.090	3.47	2.36	88.64	6.60	76.62	6.62	85.47
0.090 - 0.100	3.32	3.63	84.97	12.82	63.81	13.06	72.4
0.100 - 0.125	3	10.79	74.18	26.76	37.05	28.10	44.3
0.125 - 0.154	2.7	22.64	51.53	29.70	7.35	34.50	9.8
0.154 - 0.180	2.47	12.46	39.08	5.23	2.13	8.16	1.65
0.180 - 0.224	2.16	21.73	17.35	1.22	0.91	1.41	0.24
0.224 - 0.250	2	9.41	7.94	0.24	0.67	0.08	0.16
0.250 - 0.315	1.66	7.62	0.31	0.25	0.41	0.09	0.07
0.315 - 0.355	1.49	0.17	0.15	0.05	0.36	0.02	0.05
0.355 - 0.400	1.32	0.07	0.08	0.03	0.33	0.02	0.03
0.400 - 0.500	1	0.05	0.03	0.32	0.01	0.01	0.02
0.500 - 0.560	0.84	0	0	0	0	0.01	0.01

Tab.2 Test data of grain size of Zk23 samples

Grain size		Depth / m			
		1.6 - 1.8		8.4 - 8.6	
D / mm	φ	Percentage / %	Cumulative Percentage/ %	Percentage / %	Cumulative Percentage/%
< 0.000 5	>11	1.76	100	0.54	100
0.000 5 - 0.001	11	2.57	98.24	2.93	99.36
0.001 - 0.002	10	5.3	95.67	4.13	96.43
0.002 - 0.004	9	8.17	90.37	6.26	92.4
0.004 - 0.008	8	11.42	82.2	9.15	86.14
0.008 - 0.016	7	15.83	70.78	13.91	76.99
0.016 - 0.063	6	21.54	54.95	17.92	63.08
0.032 - 0.063	5	21.8	33.41	15.92	45.16
0.063 - 0.125	4	9.86	11.61	14.31	29.24
0.125 - 0.25	3	1.66	1.75	11.63	14.93
0.25 - 0.50	2	0.09	0.09	3.3	3.3
0.50 - 1.00	1	0	0	0	0
>1	0	0	0	0	0

Note：1.6 m - 1.8 m means of Ⅰ layer；8.4 m - 8.6 m means of Ⅲ layer。

4.3 The top fine grain layer(Ⅰ layer)

The silty clay and clay silt strata with the burying depth of 0 - 2.9 m have deposited until present-day after the Ⅱ layer (Tab. 2). Silty clay stratum with the burying depth of 1.1 m - 1.3 m contains much Pseudorotalia gaimardii, which are ones of dominant species in the East China Sea present-days, belong to the warm species of shallow-water that shows more high temperature and deep water environments. The presence of fragments of globigerina.sp. also illuminates more warm water in that days which lives in the bottom of this layer depth of 2.8 m - 3.0 m. All those combine with age of ^{14}C about 12 kaB.P. in the bottom of this layer, which we can learn that the fine grain layer deposited after deglaciation in Holocene and gradually has been submerged in the water depth of 82 m during the rise of sea level. And waves were not usually affecting the seabed except the weathers of storm wind, so we can find the fine sand lamella deposit in silt clay.

5 Conclusions

(a) The authors confirmed that the middle fine-sand deposition in borehole Zk23 was buried ancient estuary sand ridges of the Yangtze River, based on the analysis of grain size, micro-paleobiology and test age of ^{14}C from core samples in each layer and by means of sedimentary stratigraphy, biostratigraphy and chronostratigraphy.

(b) The sedimentary environments of study area around the hole before and after the glacial period as well as postglacial period is made clear, and the estuarine sublayer -undersea delta facies strata(Ⅲlayer) was deposited under the fast sea level rise in this area about 15kaB.P; buried ancient estuary sand ridges of the Yangtze River(Ⅱ layer) were formed when the sea level was the fluctuant range of 60 m - 80 m of isobath during the deglacial period around 15 - 12 kaB.P.; the silty clay and clay silt strata (Ⅰ layer) above the sand ridges were deposited, which are the depositions of shallow water faces during the sea level rose fast again around 12 kaB.P., and till to 7kaB.P. , then it keeps stable to the present.

References

[1] ZHU Yong-qi, ZENG Cheng-kai, FENG Yun. Geomorphology characteristics on the East China Sea shelf [J]. Donghai Marine Science, 1984, 2(2):1-13.

[2] YANG Chang-shu, SUN Jia-song. Tidal sand ridges on the East China Sea shelf [A]. De Boer P L, Van Gelder A and Nio S D. Tide-Influenced Sedimentary Environments and facies, Sedimentology and Petroleum Geology [C]. Netherland: D. Reidel, 1988, 23-38.

[3] YANG Chang-shu. Active, moribund and buried tidal sand ridges in the East China Sea and the southern Yellow Sea [J]. Marine Geology, 1989, 88:97-116.

[4] LIU Zhong-chen, CHEN Yi-lan, DING Ji-sheng, et al. Study on zoned characteristics and formation cause of the East China Sea submarine Topography [J]. Advances In Marine Science, 2003, 21(2):160-173.

[5] The editorial committee of the Chinese Academy of Sciences, "China Geographical", China Geographical. Marine Geographic [Z]. Beijing: Science Press, 1979.

[6] LI Guang-xue, YANG Zi-geng, LIU Yong. Study on formation cause of the submarine sedimentary in the East China Sea [Z]. Beijing: Science Press, 2005.

[7] LIU Zhen-xia, YU Hua, XIONG Yin-qian, et al. A Comparative Study on Tidal Sand Ridges in the East China Sea and Celtic Sea [J]. Advances In Marine Science, 2005, (23)1:35-41.

[8] Uehara K, Saito Y and Hori K, Paleotidal regime in the Changjiang(Yangtze) Estuary, the East China Sea, and the Yellow Sea at 6 ka and 10 ka estimated from a numerical model[J]. Marine Geology, 2002,183:179-192.

[9] ZHU Yong-qi, LI Cheng-yi, ZENG Cheng-kai, et al. On the late Pleistocene lowest sea level in the East China Sea shelf[J]. Chinese Science Bulletin, 1979, 24(7):317-20.

[10] YANG Zi-geng. High resolution strata division of Marine sedimentary in the Quaternary [J]. Marine Geology Letters, 2000, 16(2):1-4.

[11] Berné S, Vagnen P, LIU Zhenxia, et al. Pleistocene forced regressions and tidal sand ridges in the East China Sea[J]. Marine Geology, 2002, 188:293-315.

[12] ZHU Yong-qi, ZENG Cheng-kai, JIN Chang-mao. Sea level changes on the shelf of the East China Sea since the Late Pleistocene [J]. Chinese Science Bulletin, 1981,19:1 195-1 198.

[13] YANG Wen-da. Structure and sedimentary environment for submarine dune ridges in the East China Sea [J]. Marine Geology and Quaternary Geology, 2002, 22(1):9-16.

[14] LI Shao-quan, LI Shuang-lin, CHEN Zheng-xin, et al. Deltaic sedimentary sequences developed during last glacial maximum in the EA01 core on the outer shelf of the East China Sea [J]. Marine Geology and Quaternary Geology, 2002, 22(3):19-26.

[15] LIU Zhen-xia, Berné S, the L'ATALANTE Scientific Party. Paleo-environment in the continental shelf of the East China Sea since the mid-Pleistocene [J]. Marine Geology and Quaternary Geology, 1999, 19(2):1-10.

[16] LIU Zhen-Xia, Serge Berné, Yoshiki Saito, et al. Quaternary seismic stratigraphy and paleoenvironments on the continental shelf of the East China Sea [J]. Journal of Asian Earth Sciences, 2000, 18:441-452.

[17] QIN Yun-shan. Geology of the Bohai Sea [M]. Beijing: Science Press, 1985.

东海 Zk23 孔的古沙脊沉积环境

杜文博[1]，叶银灿[2]，庄振业[3]

(1. 中国水电顾问集团华东勘测设计研究院，浙江 杭州 310014；2. 国家海洋局第二海洋研究所，浙江 杭州 310012；
3. 中国海洋大学 海洋地球科学学院，山东 青岛 266003)

摘 要：根据东海陆架 Zk23 孔岩心分析资料，进行了沉积地层学、生物地层学和年代地层学分析，确定了该钻孔中段细砂层为埋藏古长江河口沙脊沉积，阐明了该孔附近海区冰消期前后和冰后期的沉积历史。约在 15 kaB.P.以前，海平面上升较快，沉积了下层的河口－水下三角洲相地层；约在 15 ～ 12 kaB.P. 的冰消期期间，海平面波动并稳定于 60 ～ 80 m 等深线附近，发育了沙脊地貌；约在 12 kaB.P. 以来海平面再度快速上升，至 7 kaB.P. 水位稳定，直至今日，沉积了沙脊上覆的浅海相粉砂质黏土和黏土质粉砂地层。

关键词：古沙脊；沉积环境；东海陆架

Eco-Environment Status of the Bohai Bay and the Impact of Coastal Exploitation

NIE Hong-tao, TAO Jian-hua

Department of Mechanics, Tianjin University, Tianjin 300072, *China*

Abstract: With the rapid economic development in the surrounding coastal zone, more and more wastewater has been discharged into the Bohai Bay. And with the scale of coastal exploitation being expanded year by year, the eco-environment of the Bohai Bay has been confronted with great pressure. In this paper, the main problems in the eco-environment of the Bohai Bay were summarized firstly. Red tides occurred more frequently and more seriously; salinity rose in inshore area, the fishery resources degenerated; all the above indicate that the eco-environment of the Bohai Bay is under a severe situation. Next, to make a concrete study of the existing status of the Bohai Bay, the eco-environment index system was set up. Then the principal components analytic method and grey relation method were adopted to carry on a comprehensive analysis on the status. The results show that serious pollution of inorganic nitrogen and active phosphate, and poor species diversity are the main presentations of the bad quality of the inshore aquatic eco-environment of the Bohai Bay, which is mainly induced by the massive discharge of pollutant from land and the overexploitation in the surrounding coastal zone. At last, the variations of hydrodynamic characteristics and the pollutant transport caused by coastal exploitations such as reclamation and seawater desalination are analyzed. The results show that reclamation in coastal water not only decreases the tidal prism and weakens the tidal current action, but also influences the pollution distribution in the coastal water. The seawater desalination project would cause tremendous influence to the aquatic eco-environment of the Bohai Bay as the pollutant's pulse impact. Much more attention would be paid to the reasonable use of the coastal zone resources and the control of pollution from land-based sources.

Keywords: Bohai Bay; aquatic Eco-environment; indicator system; reclamation; seawater desalination

Bohai Bay locates in the west of the Bohai Sea, which is a semi-enclosed interior sea in the north-eastern China. Bohai Bay is a shallow sea bay with wide mild slope beach, and covers an area of 14 700 km^2 with an average water depth of 10 m. There are a number of estuaries and wastewater outfalls along the west coastline of the Bohai Bay, from which a large amount of pollutants are discharged into the sea. Unfortunately, most of such sewage is discharged into the Bohai Bay directly without any ocean treatment engineering. Nowadays the region around the Bohai Sea has became the third pole of economic development of China, therefore many exploitation projects have been carried out or will be carried out along the coastline, such as marine chemical industry, port building, oil and gas exploitation, tourism and so on, especially the large-scale reclamation and the seawater desalination in recent years.

Received on May 23, 2008

As a result, more and more wastewater has been poured into the Bohai Bay. It is difficult for pollutants discharged from land-based resources to reach the central part of the Bohai Sea or the outer sea due to the extremely weak water exchange of the Bohai Bay. The eco-environment of the Bohai Bay will face great pressure.

Many studies have been tried to reveal the eco-environmental problem existing in the Bohai Bay [1-7], but these research works usually explain a certain aspect of the phenomenon in it. So in this article, the overall eco-environment situation of the Bohai Bay is attempted to be focused on. First the main problems which the Bohai Bay eco-environment faced are analyzed by unifying the related literature. Then the eco-environment integrated index system is set up based on the actual situation. And the principal components analytic method and grey relation method are applied to carry on the concrete analysis. At last, aimed at the coastal zone development operation, the influence, which is impacted by the human activity, on the eco-environment of the Bohai Bay is simulated.

1 Pressure on the eco-environment of the Bohai Bay

The main problems in the eco-environment of the Bohai Bay can be summarized as follows:

(a) Red tides occur more frequently and more seriously. The red tide, which happened in 1998, is considered to be the most serious disaster in the Bohai Sea. It lasted for 40 days and covered an area more than 5 000 km^2 including part area of the Bohai Bay [8]. In 2003, 2004, and 2005 red tides took place in large area in the Bohai Bay frequently [6, 8]. Moreover, red tides appear not only in summer, but also in spring and autumn. All the catastrophic events indicate that the Bohai Bay eco-environment is in serious eutrophication, and which is mainly caused by increasing pollutant flux from land into the sea. Bohai Bay receives a mass of industrial and domestic wastewater from Haihe river basin including Tianjin, Beijing and most regions of Hebei province annually. Among them, only from Tianjin the drainage amount of COD was 130 400 t and the drainage amount of inorganic nitrogen was 15 700 t in 2003, while in 2005 the COD drainage amount rose to 146 000 t and the drainage amount of inorganic nitrogen was 19 400 t [9]. In recent years, along with the rapid development of the industry, the urban construction, the aquaculture and the increase in population, the industrial and domestic waste water and the relevant pollutants increase dramatically, especially the massive discharging of nitrogen and phosphoric into the sea, which aggravates the pollution and eutrophication in the coastal water unceasingly.

(b) Salinity rises in inshore area. Investigations show that the salinity and its distribution in Bohai Sea have experienced a noticeable change, and the average salinity of Bohai Sea has been increasing dramatically. Lin et al. [10]analyzed the long-term variations of the sea surface salinity (SSS) of the Bohai Sea during 1960-1997, and the trend analysis showed that the annual growth rate of SSS was 0.074/a during that period. The region of the highest salinity is changed from the center of Bohai sea to the coastal water [11]. These variations are caused by the rapid reduction of the runoff to sea, as well as the increased evaporation from the sea surface due to the temperature rise. For example, in Haihe River Basin, the

amount of runoff to sea is only 5.4 billion m^3 in 1998 with abundant rainfall, and the average value only 0.28 billion m^3 from 1999 to 2002 with a small quantity of precipitation. The runoff to sea has been decreasing sharply since 1960s' which mainly caused by natural and human factors in the Bohai Bay coastal zone. In the natural aspect, the precipitation presents descending tendency, but the land surface evaporation increases in recent years under the background of a worldwide warming [10]. In the aspect of human activity, many river sluices have been constructed in order to satisfy the increasing water demand because of the increasing population and the accelerated economic development of Haihe river basin. These activities cut off the surface runoff and decrease the water flux entering into the sea year by year.

(c) The fishery resources degenerate. The fishing ground around the Haihe Estuary has disappeared because of the serious pollution. Jin et al. [4, 5] pointed out that the number of some high-valued species sharply decreased with their life-span and individual sizes becoming smaller. The dominant species had largely changed, while low-valued species which adapting well to the new and harsher environment had predominated in number. The overfishing and the worsening environment have broken down the Bohai Bay ecosystem, which caused a drop in the biota productivity and spoiled the stability of the ecosystem[5,7]. And with the development of coastal exploitations such as the reclamation projects and seawater desalination, large-area wetland would be occupied or damaged. Reclamation from sea not only destroys the original flow field, changes the original landform shape and the survival environment of marine life, but also influences the transportation of pollutants in the inshore water. Seawater desalination projects would worsen the local aquatic eco-environment by the discharging of concentrated seawater with the high salinity and high concentration pollutants. All these would do more harm to the eco-environment and the fishery resources would be damaged.

2 Existing aquatic eco-environment status of the Bohai Bay

2.1 Evaluation indicator system

At present, there is no recognized standard to estimate the eco-environment to be healthy or not, but two methods, including the bio-indicator law and the indicator system law, are widely used. Considering the Bohai Bay inshore water characteristics, it is very difficult to confirm which kind of species is the bio-indicator, so the indicator system law is used to analyze the Bohai Bay water eco-environment condition. Based on the analysis of the Bohai Bay eco-environment, the structure of the evaluation indicator system is developed which is divided into three levels: the target level (T), the category level (S) and the indicator level (I). The target level (T) is the evaluation level of Bohai Bay eco-environment. The category level (S) includes nutritional index (S1), environmental index (S2) and biological index about phytoplankton (S3) [12]. Under each index there are four main indicators, so the indicator level (I) is composed of 12 indicators totally. Fig. 1 illustrates the evaluation indicator structure of the Bohai Bay.

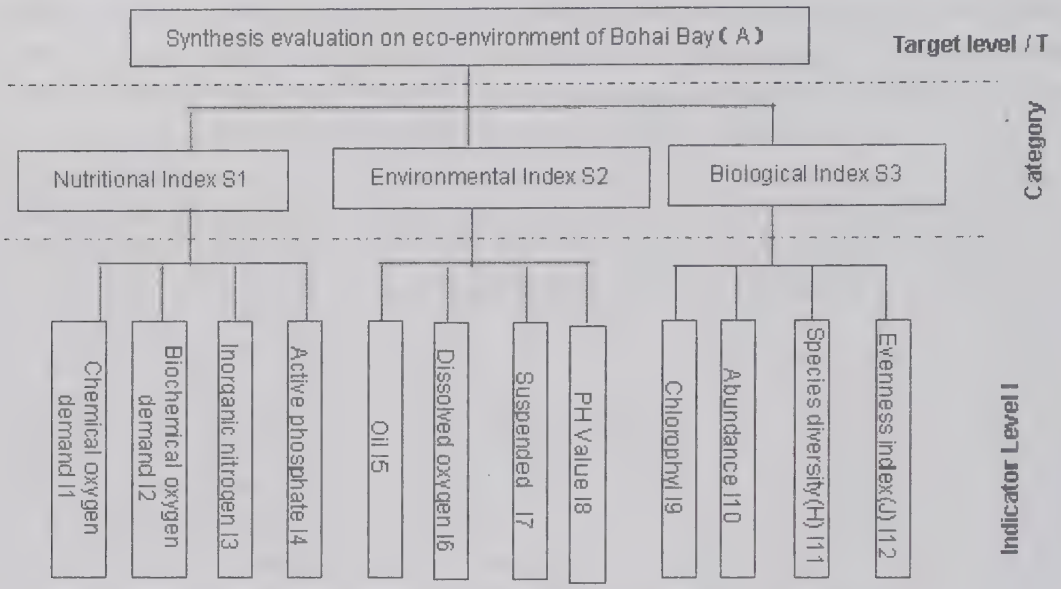

Fig. 1 Hierarchy chart to the evaluation of the Bohai Bay eco-environment

2.2 Evaluation standard

The Sea Water Quality Standard (GB 3097-1997) is used as the evaluation standard, and as there is no criterion for the biological indicators in the sea water quality standard, other water trophic level judged by biological index about phytoplankton [13] is adopted.

Fig. 2 Regular monitoring stations

2.3 Data collection

A series of field surveys and laboratory tests were undertaken. Fig. 2 shows the locations of the 16 regular monitoring stations in the Bohai Bay. The field data were collected from these stations three times a year, in May, August and October (corresponding to spring, summer and autumn) in the Bohai Bay from 2003 to 2005, respectively.

In Fig. 2, points D1, D2 and D3 indicate the locations of Yongdingxin River Estuary (or Beitang Outfall), Haihe Estuary (or Dagu Outfall) and Duliujian River Estuary, respectively.

2.4 Analysis of the variations of indicator value

The annual average value of several kinds of indicators in the last three years are showed in Fig. 3. From the figure, we can see that the inorganic nitrogen pollution was quite serious as its annual mean values for these years all exceeded the *Sea Water Quality Standard for Class 2*. The exceed value of inorganic nitrogen each year appeared in the stations 4′, 6′ and 8′nearby Beitang outlet and Dagu outlet respectively. In 2004 and 2005, inorganic nitrogen concentration in stations 12′and 14′, nearby Duliujian river estuary, also exceeded the acceptable limit severely. For active phosphate, the rate of exceeding the *Sea Water Quality Standard for Class 2* was not high. And all the maximal values for past years appeared nearby Beitang outlet and in the sea area northern to it. For chemistry oxygen demand, it did not exceed the allowed standard. This was different from the river pollution in which chemistry oxygen demand was the main matter exceeding the water quality standard and much work had been done to decrease it. But seen from the above analysis, much attention would be paid to the pollution of inorganic nitrogen. For the species diversity, its value was not bigger for the multi-annual average value in most stations. Furthermore from the figure it can be seen that the pollution of the Bohai Bay presents the characteristic of high concentration in the sea area near coastline, but low concentration in the open sea as concentration values were less in the station 13′and 16′ far away from the land. And the maximal value often emerges in the sea area nearby the pollution outlet. Since many exploitation projects are carried on and a large amount of sewage are discharged from the land, the inshore water condition will be even worse.

2.5 Synthesis evaluation on eco-environment of the Bohai Bay

The information of sea eco-environment system is multidimensional and complicated. In this paper, the Grey Relation Method based on the grey theory [14] is used for the evaluation on the eco-environment of the Bohai Bay. Considering different contributions of various indicators in the evaluation system, the weight of each indicator is determined by the principal component analytic method.

2.5.1 Analysis of the weight of Indicator

According to the indicator system in the above sections, the datum of 12 indicators about 16 stations are used to set up the initial sample matrix. In order to eliminate the difference caused by the dimension of various indicators, the initial sample is normalized and the normalized sample matrix $A_{n\times m} = (a_{ij})_{n\times m}$ is

obtained, where a_{ij} is the normalized value in the i th indicator at the j th station; n is the number of the indicators and n = 12. m is the number of stations and m = 16. Through extracting principal components from the sample correlation information matrix and determining the load of the indicator [15, 16], the weight of various indicators are obtained as following.

Firstly, the relational information matrix is defined as:

$$\Gamma_{m\times m} = \left(G^T\right)_{m\times n} \times G_{n\times m} + I_{m\times m} \tag{1}$$

where

$$G_{n\times m} = \begin{bmatrix} 1-a_{11} & 1-a_{12} & \cdots & 1-a_{1m} \\ 1-a_{21} & 1-a_{22} & \cdots & 1-a_{2m} \\ \cdots & \cdots & \cdots & \cdots \\ 1-a_{n1} & 1-a_{n2} & \cdots & 1-a_{nm} \end{bmatrix}$$

Secondly, calculated the characteristic value λ_i of the relational information matrix $\Gamma_{m\times m}$, and the corresponding characteristic vector $Q = (q_1, q_2, ..., q_m)$ is obtained. The variance contribution $E(\%)$ of characteristic value λ_i can be expressed as:

$$E_i = \lambda_i / \sum_{i=1}^{n} \lambda_i \times 100\% \tag{2}$$

Recorded $D_{m\times m}$ as the main factor load matrix, it shows the relations between the primitive factor and the main factor.

$$D_{m\times m} = Q\Lambda^{\frac{1}{2}} \tag{3}$$

where

$$\Lambda^{\frac{1}{2}} = diag(\sqrt{\lambda_1}, \sqrt{\lambda_2}, \cdots, \sqrt{\lambda_m})$$

Then the regression equation is set up by using the relational information matrix $\Gamma_{m\times m}$ and the main factor loading matrix $D_{m\times m}$, and the coefficient vector $\overline{\alpha_i}$ can be obtained:

$$\overline{\alpha_i} = {\Gamma_{m\times m}}^{-1} d_i \tag{4}$$

At last, carried out the linear combination with the characteristic value and variance contribution, the weight value of the i th indicator can be expressed:

$$\overline{w_i} = \sum_{i=1}^{n} \left|\overline{\alpha_i}\right| E_i \tag{5}$$

After normalized, the weight vector can be obtained:

$$W = (w_1, w_2, ..., w_n) \text{ and } w_i = \overline{w_i} / \sum_{i-1}^{n} \overline{w_i} \tag{6}$$

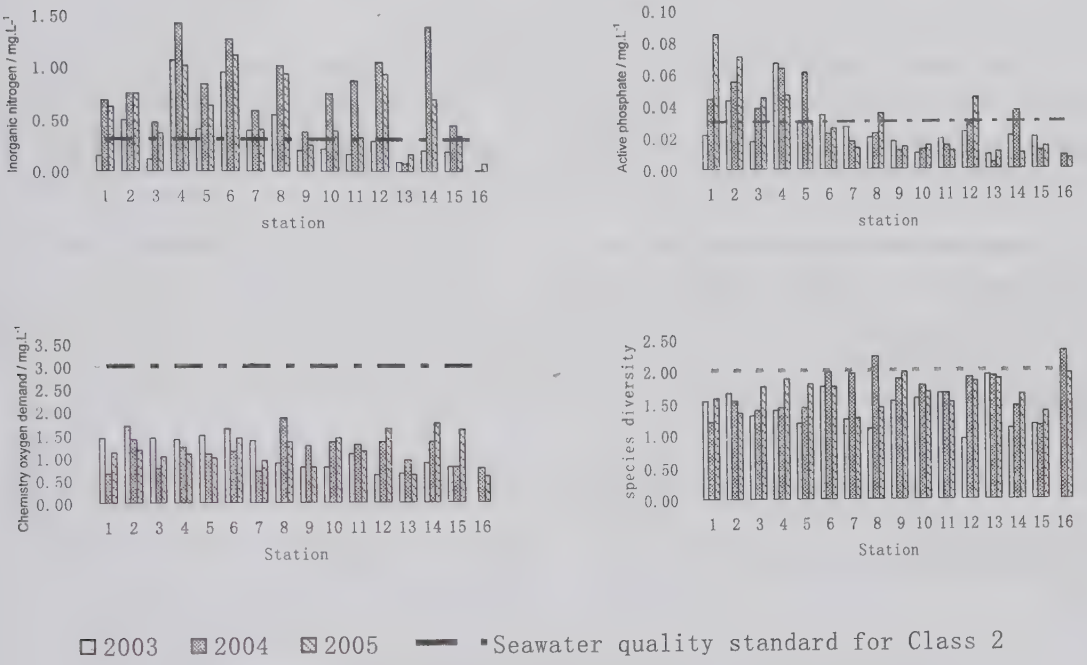

Fig. 3 Annual average value of evaluation indicators for the past three years

Fig. 4 shows the weights of each evaluation indicator of the Bohai Bay eco-environment. It can be seen from the figure that *inorganic nitrogen* (I3), *active phosphate* (I4) and *species diversity* H' (I11) account for greater weight than the others. The weights of these three indicators have exceeded 0.12 in every year, while the weight of *chemical oxygen demand* (I1) is smaller with the value being only 0.03. Thus, the main indicating factors of the Bohai Bay aquatic eco-environment are *inorganic nitrogen* (I3), *active phosphate* (I4) and *species diversity index* (I11). Combined with the variations analysis of indicator value, the serious pollution of *inorganic nitrogen* and *active phosphate*, and the poor *species diversity* are the main presentations of the bad quality of the inshore aquatic eco-environment of the Bohai Bay.

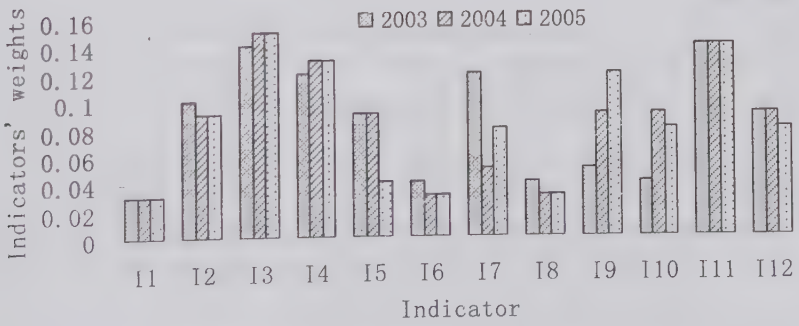

Fig. 4 Weights of evaluation indicators for Bohai Bay eco-environment

2.5.2 Evaluation on aquatic eco-environment of the Bohai Bay

Grey Relation Method is adopted to carry on a comprehensive evaluation on the inshore eco-environment of the Bohai Bay. Via carrying on the comparison between the monitor data at various stations and the corresponding indicator standard, synthesizing and analyzing their similarities or differences, the rank of water quality in each station will be ensured[14,16].

Firstly, the water quality standards of 12 indicators are used to set up the initial standard matrix. After being normalized, the standard matrix is given as $B_{m\times c}=\{b_{ik}\}_{m\times c}$, where b_{ik} is the normalized value of the indicator's standards, c is the class number of water standard and $c=4$ for the sea water quality. Then the absolute difference between the j th station and the k th standard for i th indicator can be defined as:

$$\Delta_{jk}(i)=\left|a_{ij}-b_{ik}\right| \quad (i=1,2\cdots m;\ \ j=1,2,\cdots n;\ \ k=1,2\cdots c) \tag{7}$$

And the grey relational coefficient is:

$$\xi_i(a_j,b_k)=\frac{\min\limits_k\min\limits_i\Delta_{jk}(i)+\rho\max\limits_k\max\limits_i\Delta_{jk}(i)}{\Delta_{jk}(i)+\rho\max\limits_k\max\limits_i\Delta_{jk}(i)} \tag{8}$$

where ρ is the distinguishing coefficient and its value is from 0 to 1, usually $\rho=0.5$.

Secondly, the grey relational grade, between the j th station and the k th standard, can be calculated by combining the indicator weight and the relational coefficient, as follows:

$$\gamma_{jk}(a_j,b_k)=\sum_{i=1}^{n}w_i\xi_i(a_j,b_k) \tag{9}$$

The grey relational grade $\gamma_{jk}(a_j,b_k)$ indicates the similar degree between the sample and the standards in each station. While the value of $\gamma_{jk}(a_j,b_k)$ is bigger, the sample is more close to the corresponding standard.

Taken the grey subordinate degree u_{jk} between the station sample and all levels of standards as the weighting coefficient, the relational difference degree can be written as:

$$d(a_j,b_t)=u_{jk}\overline{\gamma_{jk}(a_j,b_k)}=u_{jk}\cdot(1-\gamma_{jk}(a_j,b_k)) \tag{10}$$

where $\sum_{k=1}^{c}u_{jk}=1$, (j=1,2,...,m), and $\sum_{j=1}^{m}u_{jk}>0$, (k=1,2,...,c)

Constructed the objective function with the rule: the sum of square is smallest of all weighted relational difference $d(a_j,b_t)$ between the sample and the standards, the grey subordinate degree can

be obtained:

$$u_{jk} = 1 / \sum_{l=1}^{c} \left[\frac{\overline{\gamma_{jk}}}{\overline{\gamma_{jl}}} \right]^2 \quad (j = 1,2,\cdots,m) \tag{11}$$

At last, the grey synthesis index $GSI(j)$, for the eco-environment of each station, can be expressed as:

$$GSI(j) = (u_{jk}) S^T = \sum_{k=1}^{c} t u_{jk} \quad , \quad (j = 1,2,\cdots,m) \tag{12}$$

where $S^T = (1,2,\ldots c)$ is the rank vector for the standard. And it can be seen that the value of $GSI(j)$ is between 1 and c. The grey synthesis index $GSI(j)$ indicates the aquatic eco-environment quality (Tab. 1).

Tab. 1 Grey synthesis index GSI and the aquatic eco-environment quality

Grey Sythesis Index (GSI)		$GSI < 1.0$	$1.0 \le GSI < 2.0$	$2.0 \le GSI < 3.0$	$GSI \ge 3.0$
Quality of Aquatic Eco-environment		good	normal	poor	worse
Stations	2003	—	1、3、9、10、11、13、14、15	2、4、5、6、7、8、12	—
	2004	—	9、13、15、16	1、2、3、4、5、6、7、8、10、11、12、14	—
	2005	—	7、9、13、15、16	1、2、3、4、5、6、8、10、11、12、14	—

The evaluation results of the Bohai Bay aquatic eco-environment are given in Tab.1 and Fig.5 by using the indicator system and the evaluation method set up in the above sections. It can be seen from Fig.5 that the eco-environment quality is very poor at station 4′, 8′ and 12′, while it is better at stations of 13′ and 16′ in 2003, 2004 and 2005. As showed in Fig.1, the station 4′, 8′ and 12′are located nearby Beitang outfall, Dagu outfall and Duliujian river estuary respectively. But station 13′ and 16′are far away from the land. Considering the space distribution, the aquatic eco-environment of the Bohai Bay presents the tendency of changing for the better from the inshore water to the distant sea. The inshore water eco-environment, especially near the sewage outfall, is worse, which illuminates that the aquatic eco-environment of the Bohai Bay is mainly influenced by the discharging of land-based wastewater. And investigations show that approximately 87% of pollutants are discharged from land, and 95% of pollutants generated in the land are transported by rivers into the Bohai Sea[17]. Most of the pollutants come from the domestic sewage and industrial wastewater in the Haihe basin. Since many exploitation projects will be set up and a large amount of sewage will be discharged from the land in the future, it will be a very challenging task to manage the inshore water eco-environment of the Bohai Bay.

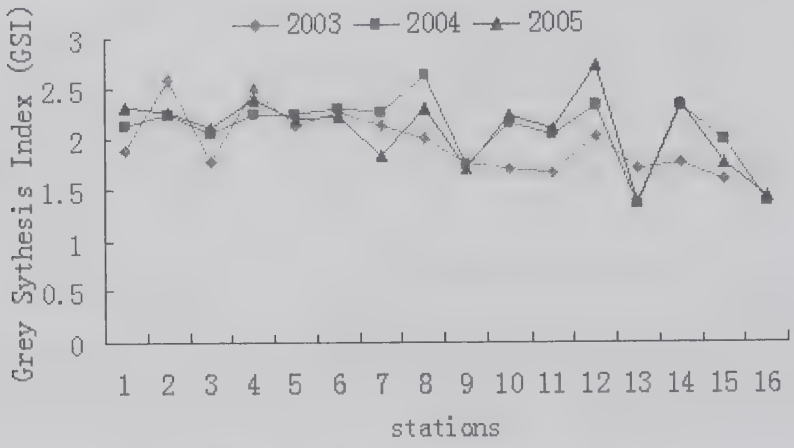

Fig. 5 Results of the aquatic eco-environment assessment

3 Influence on the aquatic eco-environment of the exploitation in Bohai Bay coastal zone

The Bohai Bay coastal zone is a region with high strength of exploitation. More and more space is demanded for the great advance of economy, and thus some exploitations such as the reclamation from sea, come to be necessary. At the same time, however, the sustainable development of economy must be kept on, and the harmoniousness must be achieved between the economic development and the eco-environment. Therefore, it is very important to investigate the influence of the exploitation upon the eco-environment.

In this paper, taking a few coastal exploitation projects along the coastline of Tianjin as examples, their influences on aquatic eco-environment are analyzed. Some of which are already finished and the other will be implemented before long. In Fig. 6, A, B1, B2, B3, C1, C2 are the positions of these reclamation projects, and the region surrounded by B1, B2, B3 is Tianjin port; D1, D2 indicate the two main sewage outfalls in Tianjin coastal zone, the Beitang Outfall and the Dagu outfall respectively. Point E is the discharge outfall for the highly concentrated salt water of a seawater desalination project.

And in this study, a depth-integrated hydrodynamic and solute transport model was adopted to predict the impact of various projects. The model has been well applied to many coastal basins for simulating the hydrodynamic and solute transport processes [18].

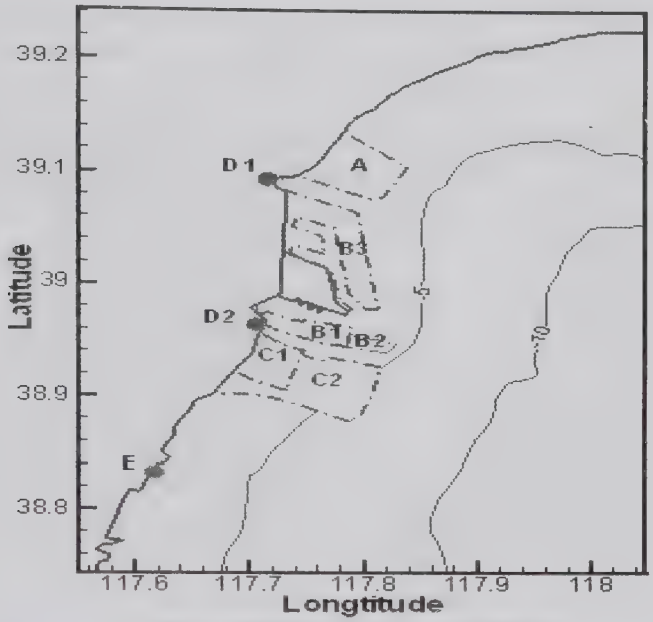

Fig. 6 Sketch map for exploitation

3.1 Influence of reclamation from sea

3.1.1 Variations of hydrodynamic characteristics

The studied area is confined between 117°30' - 118°25'E and 37°54' - 39°15'N in the Bohai Bay, and the tide data of M2 is applied as the hydrodynamic condition on the open boundary. The variations of tidal flow field are studied under the influence of reclamation projects (Fig. 7).

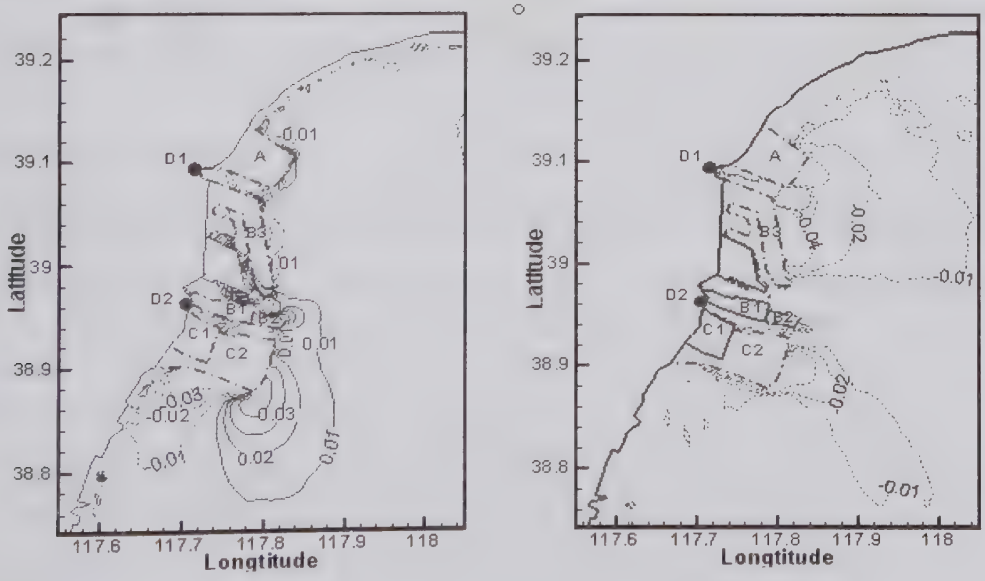

(a) at peak time of flood (b) at peak time of ebb

Fig. 7 The Change of Tidal Current before and after Reclamation

(after project – before project. real line is positive, dashed is negative)

Fig. 7 illustrates the variation of tidal flow field in the coastal water before and after the reclamation. It can be seen that project C1 and project C2 occupy the original stronger flow field nearby the Dagu sewage outfall, and a new Haihe eatusry channel has come into being with the project B1 and B2. In the channel, the flow speed is lower, which is a disadvantage for the transportation and diffusion of the pollutants discharged from Dagu outfall (D2). With projects B3 and A being completed, a narrower channel of Yongdingxin River is also formed and in this channel the same problem appears again. Compared with the situation before the reclamation, at peak time of flood, the current speed reduces obviously in the area south to Project C1 after the reclamation, while in the area southeast to Project C2, the current speed increases. At the peak time of ebb, the current all presents a tendency of reduction in the coastal water. On the whole, the exploitation will have great influence on the inshore field of the Bohai Bay.

Furthermore, statistic analysis of the simulation shows that if all the reclamation projects had been completed, the tidal prism would be reduced by more than 1% in the area (117°35' - 118°E, 38°48' - 39°15'N) closed to the coastline. The variation of tidal prism directly influences the intensity of water exchange between the bay and the open sea, and the distribution of marine life such as phytoplankton. Therefore, it plays a very important role for maintaining the healthy eco-environment. With the tidal prism reduced, the tidal current hydrodynamic action will be weakened. Then it will possibly cause silting up which is a disadvantage for the shipping of the port, and change the sediment which will influence the habitats of the benthos. In additions, decrease of the tidal prism also affects the transport of pollutants, and then causes the deterioration of water quality.

3.1.2 Variations of pollutant transport

The Dagu outfall (D2) is one of the main sewage discharge outlets along the Bohai Bay coastline. Simulations are carried out on the pollutants discharged from Dagu outfall under the influence of the reclamation. COD is selected as the simulation indicator and the discharge flux is 3.6 kg per hour. The maximum values in various regions are computed, and the result is shown in Fig. 8.

Before the construction of project C1 and C2, the pollutants discharged from the Dagu outfall obviously move to the south side of the coastline, as shown in Fig. 8a. After the completion of projects C1 and C2, the wastewater would flow into the Tianjin port. In addition, between project B1, B2 and project C1, C2 the sewage concentration is very high, and the water quality worsens, which will affect the environment quality of Tianjin port and the area nearby, as shown in Fig. 8b. The reason is that reclamation projects change the flow field in the coastal water and influence the transportation of the pollutants. As mentioned in the above section, the flow speed is lower in the narrow channel between projects C1, C2 and projects B1, B2. With the weak transport action, the pollutants discharged from Dagu outfall (D2) would accumulate gradually and cause high concentration in the channel. Besides, the channel outlet is near the Tianjin port, and there is clockwise tide-induced residual current, so the wastewater would influence the water quality near Tianjin port obviously. To deal with this problem, changing the position of sewage outlet such as offshore emission is a good means, and establishing corresponding treatment engineering is a good way too.

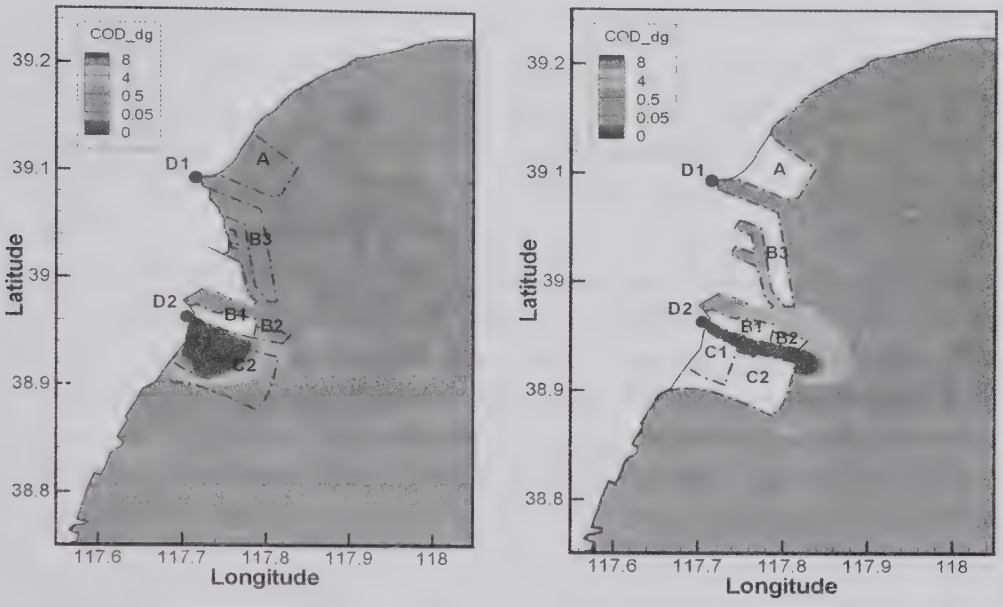

Fig. 8 Contours of COD concentration while wastewater discharges from Dagu outfall(D2)

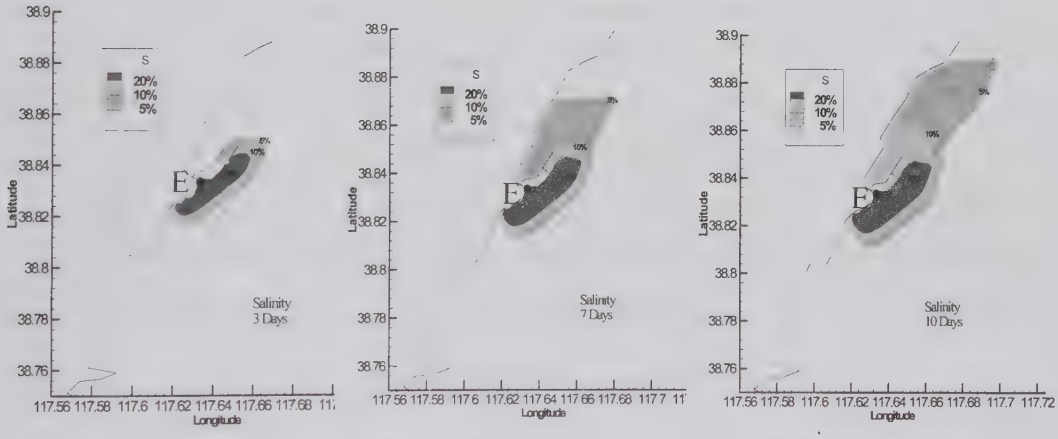

a) Continuous discharging for 3 days b) continuous discharging for 7 days c) continuous discharging for 10 days

Fig. 9 Distribution of sea water salinity rise

3.2 Influence of seawater desalination engineering

Nowadays, many coastal regions in north china face a serious shortage of fresh water resources. Since sea water is unexhausted, seawater desalination project would be a considerable way to solve this problem. But if the scale of seawater desalination is too large, it will also bring many problems to the eco-environment in the coastal area, such as a great lost of the plankton and fish eggs, which is caused by drawing massive sea water, and discharging the concentrated sea water with high salinity, heat and

pollutants.

In this paper, a seawater desalination project, with a production of 100 thousand tons per day, is investigated as an example. The outfall for high concentrated salt water of the project is marked with point E in Fig. 6. The scenes that salt water with high concentration discharges continuously for 3 days, 7 days and 10 days are simulated respectively. Through the simulation, the salinity rising area is analyzed. The results are shown in Tab. 2 and Fig.9. It can be seen from the results that after the continuous discharging of high salinity water lasts for 3 days, the sea area with salinity rising by 5% is 6.34 km^2, and then it extends to 17.3 km^2 after 7 days and to 25.97 km^2 after 10 days. With the discharge of concentrated salt water, the inshore water salinity rises gradually and the affected area extends constantly. Due to the weak action of water exchange in the Bohai Bay, the high-salt water is difficult to be transported into the open sea. As more and more seawater desalination projects are carried out, more concentrated salt water will be discharged, and therefore the protection of the eco-environment of the Bohai Bay will be under greater pressure. Since the high-salt water gathers near the outfall and the transport action is weak in the coastal area, much work has to be done to select the position of outfall. And the position should be far away from the biological living area. Moreover, it is good to make comprehensive utilization of high concentrated salt water such as salt-making etc. and establish treating plant to decrease the duration time and concentration of salt water discharge.

Tab. 2 Variations of the area with salinity rise

	Area / unit: km^2		
	Salinity rise by 5%	Salinity rise by 10%	Salinity rise by 20%
Discharge for 3 days	6.336	4.484	3.022
Discharge for 7 days	17.302	7.213	4.630
Discharge for 10 days	25.977	12.477	5.215

4 Conclusion

Bohai Bay coastal zone is one of the hot regions of economic development in China nowadays. With the fast economic development, Bohai Bay eco-environment has faced many problems. In this paper, integrated analysis is carried on and it can be seen that:

(1) Bohai Bay aquatic eco-environment has suffered from considerable human impacts through an enormous amount of sewage and intensive exploitation. In the Bohai Bay, red tides occur more frequently, and salinity in inshore area rises obviously, and the fishery resources degenerate seriously.

(2) In recent years, *inorganic nitrogen* and *active phosphate* are the two primary pollutants in Bohai Bay, and especially the concentration of *inorganic nitrogen* exceeds the *Sea Water Quality Standard for*

Class 2 severely. And *species diversity* is poor, whereas the pollution of *chemical oxygen demand* is not serious and its annual average value presents the descend tendency. Besides, the worse areas of aquatic eco-environment are mainly concentrated in the sewage outfall and the nearby sea area, and the pollution in sea area presents to be serious in the area near coastline, while be slight in the far shore. These phenomena indicate that Bohai Bay aquatic eco-environment is affected by the discharging of pollutant from land greatly.

(3) The coastal zone exploitation influences the eco-environment of nearshore area obviously. The reclamation from sea not only decreases the tidal prism and weakens the tidal current action, but also influences the pollution distribution in the nearshore area. The project of seawater desalination also has great influence on the aquatic eco-environment of the Bohai Bay as the pollutants pulse impact.

In a word, the aquatic eco-environment of the Bohai Bay is under a severe situation, which is mainly influenced by the pollutants from land and the coastal exploitation by human being. As the water exchange is weak, and the self-cleaning capacity and pollution carrying capacity is poor in the Bohai Bay, the eco-environment becomes worse because a large amount of pollutants from land are discharged into the sea. Coastal exploitations, such as reclamation from sea, building seawater desalination engineering and sluice in the estuary etc., often damage the aquatic eco-environment of the coastal water as well as bring the economic benefits. It's necessary to pay more attention to the reasonable use of the coastal zone resources and the control of pollution from land-based sources.

Acknowledgements

This work is financially supported by the National Natural Science Foundation of China (Grant No: 50479049), the Support Plan of Science and Technology of Tianjin (Grant No.07ZCGYSH01700), the Natural Science Foundation of Tianjin (Grant No.07JCZDJC10700) and Global Environmental Foundation (Grant No.TF053183).

References

[1] Qin Y W, Meng W, Zheng B H, et al. Distribution features of nitrogen and phosphorus in aquatic environments of the Bohai Gulf [J]. Acta Oceanologica Sinica, 2005, 27(2):172-176.

[2] Shen Y L, Zhang H, Ma X, et al. The influence for the ocean primary yield-power (chlorofucinc) with the change of inorganic nitrogen and reactive phosphate in the Bohai Ocean Gulf [J]. Environmental Monitoring in China,2004,20(1):52-54.

[4] Jin X S, Tang Q S. The structure, distribution and variation of fishery resources in the Bohai Sea [J]. Journal of Fishery Sciences of China,1998,5(3): 18-20.

[5] Jin X S. The dynamics of major fishery resources in the Bohai Sea [J]. Journal of Fishery Sciences of China, 2001, 7(4): 22-26.

[6] Fang E J, Li W K , Chen W, et al. A discussion on occurrence of red tide nearshore of Tianjin in the Bohai Bay

and prevention countermeasure [J]. Modern Fisheries Information,2006,21(2): 15-17.

[7] Guo X P, Jin X S, Dai F Q. Growth variations of small yellow croaker (Pseudosciaena polyactis Bleeker) in the Bohai Sea [J]. Journal of Fishery Sciences of China, 2006, 13(2): 243-249.

[8] State Oceanic Administration of China. China Marine Disaster Bulletin, 1995-2005.

[9] Tianjin Environmental Protection Bureau. Tianjin Environment Outlook, 2001-2004.

[10] Lin C L, Su J L, Xu B G, et al. Long-term variation of temperature and Salinity of the Bohai Sea and their influence on its ecosystem [J]. Progress in Oceanography, 2001, 49: 7.

[11] Wu D X, Wan X Q, Bao X W. Comparison of summer thermohaline field and circulation structure of the Bohai Sea between 1958 and 2000 [J]. Chinese Science Bulletin, 2004, 49(4): 363-369.

[12] Karydis M, Tsirtsis G. Ecological indices: a biometric approach for assessing eutrophication levels in the marine environment [J]. The science of the Total Environment, 1986, 186:209-219.

[13] Li Q X, Tao J H. Application of phytoplankton community indexes in coastal eutrophication assessment [J]. China Environmental Science, 1999, 19(6): 548-551.

[14] Deng J. Control problems of grey systems [J]. System Control Letter, 1982, 5: 288-294.

[15] Chen Y C, Li Z P, Cao Q H. Weighting technique in environmental quality assessment [J]. Chongqing Environmental Science, 1997,17(2): 43-47.

[16] Shi X X, Xia J. Grey-mode identification model for water environmental quality assessment and its application [J]. China Environmental Science, 1997, 17(2): 127-130.

[17] Liu C, Wang Z Y, He Y et al. Analysis on water quality of the estuary around Bohai Bay [J]. Environmental Pollution & Control, 2003, 25(4):222-225.

[18] Wang Z L, Tao J H. Numerical study of pollutant transport in the Sea-Bay with mild slope beach [J]. Acta Oceanologica Sinica, 1998, 17 (3): 399-408.

渤海湾水生态环境现状和海岸带开发对其的影响研究

聂红涛，陶建华

（天津大学力学系，天津 300072）

摘 要：由于沿海地区经济迅速发展，越来越多的陆源污水排入渤海湾，渤海湾生态环境系统承受着巨大的压力。本文建立了渤海湾生态环境的多级指标体系，并根据2003年至2005年多次渤海湾监测资料对其现状进行了分析；然后进一步研究了由于围海造地、海水淡化等开发工程引起的近岸海域水动力条件和污染物输移的变化。结果表明，陆源污染物大量排放、沿海开发活动加剧是影响渤海湾水生态环境的主要原因。沿海围垦不仅导致潮通量减少，潮流作用减弱，而且影响近岸海域污染物的输移和分布。海水淡化高浓度盐水的排放也对近岸海域的水生态环境造成很大的影响。

关键词：渤海湾；水生态环境；指标体系；围海造地；海水淡化

海 洋 通 报（英文版）

HAIYANG TONGBAO

2009 年 10 月 第 11 卷 第 2 期

目 次

红外和微波辐射计反演海表面温度的比较 …… 殷晓斌 等 (12)

变分同化方法反演海气耦合模型参数的研究 ……杜华栋 等 (22)

台湾海峡及其邻近海域潮汐数值计算 …… 朱 佳 等 (36)

污损生物对大亚湾养殖扇贝的食物吸收及营养盐排泄的影响 ……苏振霞 等 (44)

夏季台湾浅滩周边水域悬浮物质浊度和叶绿素 a 荧光分布特征…… 胡 毅 等 (54)

楚科奇海浮游植物的分布与环境因子的关系…… 林更铭 等 (64)

相手蟹属两种蟹类线粒体 16S rRNA 基因序列的比较 …… 徐敬明 (69)

东海 Zk23 孔的古沙脊沉积环境 ……杜文博 等 (80)

渤海湾水生态环境现状和海岸带开发对其的影响研究 ……聂红涛 等 (96)

Marine Science Bulletin

Marine Science Bulletin publishes papers on marine science and technology including physical oceanography, chemical oceanography, marine biology, marine geology, environmental oceanography, estuarine & coastal sciences, marine technology, digital ocean, coastal zone management, ocean engineering, marine economics, etc., and aims to promote international academic exchange.

Editor-in-Chief: XU Sheng (徐　胜)
Associate Editor-in-Chief: HE Guang-shun (何广顺)　LU Ming-sheng (卢明生)
Executive Editor: YANG Rui (杨　瑞)　QIU Wen-jing (邱文静)　LI Xue (李　雪)
ZHANG Xiao-xian (张潇娴)　YUAN Ze-yi (袁泽轶)
English proofed by: WANG Qi (王　琦)

Semi-annually (started in 1999, sum 22)
Publication date: May. 15th and Oct. 15th

Marine Science Bulletin **(Vol. 11, No. 2, Oct. 2009)**

Responsible Institution:
State Oceanic Administration of China
Sponsored by:
National Marine Data and Information Service
Edited by:
Office of Marine Science Bulletin (English edition)
Printed by:
Printery of National Marine Date and Information Service

Published by:
Office of Marine Science Bulletin (English edition)
E-mail: msb@mail.nmdis.gov.cn
Tel: (022) 24011287
Address: 93 Liuwei Rd., Hedong District, Tianjin 300171, China

---

ISSN1000-9620
CN12-1271/N

Price: $ 30.00 / ￥18.00 Per year